Numerical simulation and optimization of the magnet system for the Lorentz Force Velocimetry of low-conducting materials

Der Fakultät für Elecktrotechnik und Informationstechnik der
Technischen Universität Ilmenau
zur Erlangung des akademischen Grades eines
Dr. Ing.

eingereichte Dissertation

von
Herr Dipl. Ing. Artem Alferenok
aus
Moskau

Datum der Einreichung: 29. November 2012

Referent: Dr.-Ing. Ulrich Lüdtke

Koreferent: Prof. Dr.-Ing. Bernard Nacke

Koreferent: Prof. Dr.-Ing. habil. Hannes Töpfer

Tag der mündlichen Prüfung: 25. Februar 2013

urn:nbn:de:gbv:ilm1-2013000083

Erklärung der eigenständigen Anfertigung einer Dissertationsschrift

Hiermit versichere ich, dass ich die Dissertationsschrift mit dem Titel: „Numerical simulation and optimization of the magnet system for the Lorentz Force Velocimetry of low-conducting materials“ vollständig eigenständig angefertigt habe. Alle verwendeten Hilfsmittel und Quellen wurden von mir im Schrifttum der Arbeit angegeben.

Artem Alferenok Ilmenau, den 26.11.2012

Zusammenfassung

Die Anwendung von Lorentz-Kraft-Anemometern (LKA) für schwach leitfähige Materialien wurde numerisch untersucht. Das Modell des LKA wurde mit Hilfe des kommerziellen Programms COMSOL Multiphysics entwickelt. Das Ziel der Untersuchungen war die Optimierung der Magnetsysteme für eine konstante Geschwindigkeit (v =5 m/s) und eine vorgegebene elektrische Leitfähigkeit (σ = 4 S/m) des Elektrolyten. Der Querschnitt des Elektrolyten beträgt 0,05 m×0,05 m, der Abstand zwischen dem Elektrolyt und dem Magnetsystem (MS) beträgt 3 mm. Als Material für die MS wurde Nd-Fe-B verwendet. Optimierung bedeutet Maximierung der Lorentzkraft F_L und Minimierung der Masse m des MS. Aus konstruktiven Gründen bezüglich der Kraftmesseinrichtung wurde die Masse des Messsystems auf maximal 1 kg beschränkt und eine Auflösung der Messgrösse F_L von wenigstens 10 μN gefordert. Das Modell wurde, bezüglich des Magnetfeldes mit Hilfe von analytischen Lösungen, verifiziert.

Fast alle Ergebnisse dieser Arbeit wurden unter der Voraussetzung des konstanten Geschwindigkeitsprofils vom Elektrolyten ermittelt (Festkörperapproximation). Diese Annahme reduziert die Rechenzeit wesentlich und wurde mit Hilfe der experimentellen Ergebnisse und auch numerisch mittels k-ϵ Turbulenzmodell validiert. Für ein konstantes und ein turbulentes Geschwindigkeitsprofil betragen die Unterschiede bei den F_L weniger als 5 %. Die optimierten Abmessungen von den Magneten bei der Festkörperbewegung sind deswegen näherungsweise auch für turbulente Strömungen zulässig. Die niedrige magnetische Reynolds Zahl ($Rm \ll 1$) hat uns erlaubt, die Differentialgleichungen im Modell zu entkoppeln.

Das Rechengebiet wurde mit dem Faktor 4 für $N = 1$ und mit Faktor 2 für $N > 1$ reduziert, wobei N die Anzahl der Magnete in einem von beiden Halbach-Arrays im MS ist. Unterschiedliche MS (Halbach-Arrays) wurden mit Hilfe der Optimierungs-Toolbox in MATLAB optimiert, wobei die Funktion *fmincon* verwendet wurde. Um das Polynom für die F_L zu bekommen, wurde die Methode der kleinsten Quadrate verwendet. Die Optimierungen mittels Polynom 2. und 4. Grades wurden für $N = 1$ und $N = 3$ durchgeführt. Da der Unterschied zwischen den Ergebnissen unwesentlich war, wurde das Polynom 2. Grades weiter benutzt, um die Rechenzeit zu reduzieren.

Die Sensibilität der optimierten Ergebnisse wurde bezüglich der Änderung der v, σ, der Magnetisierung M und der Position vom Kanal relativ zum MS entlang der y und z Achse für verschiedene MS analysiert. Die Sensibilität der Lorentzkraft bezüglich v und σ ist etwa 1 und bezüglich der Magnetisierung M etwa 2,05 für alle N. Das MS mit 18 Magneten ($N = 9$) und mit den optimalen Abmessungen der Magnete wurde als das optimalste MS für die angegebenen Ausgangsdaten und Beschränkungen ermittelt.

Abstract

The use of Lorentz Force Velocimetry (LFV) for low conducting material has been investigated numerically. A numerical model of LFV was developed using COMSOL Multiphysics software. The main goal of the investigation was to optimize the magnet system for fixed velocity (v = 5 m/s) and conductivity ($\sigma = 4$ S/m) of an electrolyte, fixed cross-section dimensions of the electrolyte (0.05 m×0.05 m), fixed distance between the electrolyte and magnet system (3 mm), and no change in the material of the magnets (Nd-Fe-B). Optimizing in this instance means maximizing the Lorentz force F_L and minimizing the weight of the magnet system m. There were predefined restrictions on the F_L and the m, which were due to the measurement system available. The limits to be satisfied were: $F_L \geq 10$ μN and $m \leq 1$ kg.The numerical model was verified for the magnetic field using analytical methods from the literature. The numerical model was validated for the F_L using the experimental data provided by our colleagues.

Almost all results of this work were obtained assuming a constant velocity profile for the electrolyte (solid body approximation). This assumption reduces computing time substantially. The solid body approximation was validated using experimental data and, also, numerically, using the k-ϵ turbulence model. These tests showed very little difference in the F_L for a solid and a turbulent velocity profile (less than 5%). Therefore the optimized magnet dimensions for a solid body are taken to be valid for turbulent flow. The low Rm approximation ($Rm \ll 1$) showed that there was no need to couple the PDEs employed.

Symmetry conditions allowed us to reduce the computation domain by a factor of 4 for $N = 1$ and by a factor of 2 for $N > 1$, where N is the number of magnets in a Halbach array. The different magnet systems (Halbach arrays) were optimized using the optimization toolbox in MATLAB. In the optimization toolbox, *fmincon* function was used. Least square fit was used to obtain the polynomial expression for F_L. Validation of the polynomial expression was performed: optimization using 2nd and 4th order polynomials was accomplished for $N = 1$ and $N = 3$. As the difference between the results was negligible, the 2nd order polynomial was accepted, since it requires fewer objective function evaluations.

Sensitivity analysis of the optimal solution was carried out for v, σ, M, and the position of the channel relative to magnet system along the y and z axis (y_0 and z_0) for N=1, 5, and 9. The optimal magnet dimensions are insensitive to v, σ, and M and sensitive to y_0 and z_0. The sensitivity of F_L in respect of v and σ is approximately 1 and in respect of M about 2.05 for all N. A magnet system containing eighteen magnets ($N = 9$) and with optimized magnet dimensions proved to be the most suitable for given input data and constraints.

Acknowledgments

This piece of work would not have been possible without the kind help of many people and institutions. The following list is not exhaustive: Ulrich Lüdtke and Alban Pothérat, Rico Klein, Xiaodong Wang, Oleg Andreev, Yuri Kolesnikov, Dietmar Schulze, Vitaly Minchenya, Maxims Kirpo, Bojana Petković, Andre Wegfrass, Christian Diethold, Michael Werner, Michael Gramss, Mladen Zec, Gautam Pulugundla, Carmen Stelian, Bernd Halbedel, André Thess, Stefan Buchelt, Henning Schwanbeck, Gaby Böhme, Cindy Karcher, Susan Kubitz, Deutsche Forschungsgemeinschaft (grant GRK 1567/1). They all know how they helped but I want them to know that I am more than grateful.

Contents

Table of symbols

x, y, z	Cartesian coordinates
t	time (s)
$\partial/\partial t$	time derivative (1/s)
$\mathbf{e_x}, \mathbf{e_y}, \mathbf{e_z}$	unit vectors in Cartesian coordinates
$\mathbf{v}$	velocity vector filed (m/s)
$\mathbf{B}$	magnetic field and magnetic flux density (vector field) with B_x, B_y, and B_z components in a Cartesian coordinate system (T=Wb/m^2=kg$\cdot$ s$^{-2}\cdot$ A^{-1})
$\mathbf{J}$	eddy current density (vector field) with J_x, J_y, and J_z components in a Cartesian coordinate system (A/m^2)
$\mathbf{F_L}$	Lorentz force (vector field) with F_{Lx}, F_{Ly}, and F_{Lz} components in a Cartesian coordinate system (N=kg$\cdot$ m$\cdot$ s^{-2})
F_{Lx}, F_L and F	Lorentz drag force (N)
F'	polynomial approximation of the Lorentz drag force (N)
F_L^{max}	maximal Lorentz drag force (N)
$\mathbf{f_L}$	Lorentz force density (vector field) (N/m^3)
σ	electrical conductivity (S/m=s$^3\cdot$ A$^2\cdot$ kg$^{-1}\cdot$ m^{-3})
S	cross-section area and surface (m^2)
$\mathbf{B_r}$	remanence vector field (T)
$\mathbf{H_c}$	coercitivity vector field (A/m)
$\mathbf{M}$	magnetization vector field with M_x, M_y, and M_z components in a Cartesian coordinate system (A/m)
$\mathbf{E}$	electric field intensity (V/m=kg$\cdot$ m$\cdot$ s^{-3}A^{-1})
$\nabla \times \mathbf{a}$	curl operator of the vector field $\mathbf{a}$
$\nabla \cdot \mathbf{a}$	divergence operator of the vector field $\mathbf{a}$
∇a	gradient of a scalar a
$\mathbf{D}$	electric flux density vector field (C/m^2)
$\mathbf{H}$	magnetic field intensity vector field (A/m)
ρ	electric charge density (C/m^3) and density (kg/m^3)
ν	kinematic viscosity (m^2/s)

Ha	$L \cdot B\sqrt{\sigma/(\rho\nu)}$, Hartmann number
ϵ	permittivity (F/m)
μ_r	relative permeability
μ_0	absolute permeability ($\mu_0 \ = \ 4 \cdot \pi \cdot 10^{-7}$ H/m)
$\mu = \mu_0 \cdot \mu_r$	permeability (H/m)
ϕ	electric scalar potential (V) and unknown quantity in Chapter 3
$\mathbf{A}$	magnetic vector potential (Wb/m)
V	volume (m^3)
$\mathbf{n}$, $\hat{\mathbf{n}}$	outward normal unit vector
L	characteristic length (m)
M_0	characteristic magnetization (A/m)
M_s	surface magnetization (A/m)
V_0	characteristic velocity (m/s)
F_0	$\sigma V_0 \mu_0^2 M_0^2 L^3 \ = \ 2.97025 \cdot 10^{-3}$, characteristic Lorentz force (N)
m	magnet system weight (kg)
$m_0 \ = \ \rho L^3$	characteristic magnet system weight (kg)
$Rm \ = \ \sigma\mu \mathrm{v} L$	magnetic Reynolds number
Ω	domain
Ω_e	subdomain or element
$\mathfrak{L}$	differential operator
f	excitation function
e	element number
M	number of elements
n	number of nodes in an element
i, j	node number of an element e
N_j^e	interpolation function in an element e
$[K^e]$	$n \times n$ matrix of unknowns
$\{b^e\}$	$n \times 1$ column excitation vector
N	total number of unknowns; number of magnets in Halbach array
$\{R^e\}$	$n \times 1$ vector of residuals

$\mathbf{J_a}$	microscopic Ampere's current density in the volume of the magnet (A/m^2), see subsection 3.2.1
$\mathbf{J_{sa}}$	microscopic Ampere's current density on the surface of the magnet (A/m), see subsection 3.2.1
$\mathbf{R}$, $\mathbf{r}$, and $\mathbf{r'}$	vectors (m)
ϕ_m	scalar magnetic potential (A)
a, b, and c	permanent magnet dimensions (m)
$G(\mathbf{x}, \mathbf{x'})$	Green's function
$\rho_m = -\nabla \cdot \mathbf{M}$	volume charge density (A/m^2)
$\sigma_m = \mathbf{M} \cdot \hat{\mathbf{n}}$	surface charge density (A/m)
k, n, and m	indexes
h	distance from the magnet and channel height (m)
w	channel width (m)
ϵ_1	relative error by computation of the $B_z(h)$ in the vicinity of the rectangular permanent magnet (analytic vs. numeric)
ϵ_B	relative error by computation of the $B_y(x, y, z)$ profiles between two permanent magnets (analytic vs. numeric)
x_1, x_2, x_3, x_4	dimensions of the magnets (design variables) (m)
x_g	gap size between the magnet and electrolyte (m)
Δ_e	maximal element size by domain discretization (m)
K	calibration coefficient
$\dot{V}$	specific volumetric flow rate (m^3/s)
c_{ij} and c_i	coefficients of the polynomial
$G(x_i)$	inequality constraint for the magnet system weight (kg)
x_i^{min}, x_i^{max}	lower and upper bounds of the design variables x_i (m)
$x_i^{low}, x_i^{mid}, x_i^{up}$	lower, middle, and upper value of design variable x_i (m)
$\tilde{x}_i$	normalized (divided) by L design variable x_i ($\tilde{x}_i = x_i/L$)
Δ	normalized by L step size at validation of the polynomial expression for the objective function
ϵ_{3DV}	relative error on validation of the polynomial expression including 3 design variables, see subsection 4.2.5

$P(x_{1i}, x_{2j}, x_{3k})$	point in design space including 3 design variables
F/m	Ratio of Lorentz drag force to the magnet system weight, i.e. efficiency of the magnet system (N/kg)
ϵ_{4DV}	relative error on validation of the polynomial including 4 design variables, see subsection 4.4.3
$P(x_{1i}, x_{2j}, x_{3k}, x_{4l})$	point in design space including 4 design variables
D	distance between two permanent magnets or Halbach arrays (m)
L_{my}, L_{mz}	magnet dimensions along the y and z axes, respectively (m)
X	disturbance parameter
F^{opt}	optimal Lorentz drag force (N)
x_i^{opt}	optimal design variable (m)
m^{opt}	optimal magnet system weight (kg)
z_0	position of the magnet system vis à vis the channel along the z axis (m)
y_0	position of the magnet system vis à vis the channel along the y axis (m)
S_X	relative sensitivity
η	relative disturbance parameter by computing of S_X
δ	boundary layer thickness (m)
L_x	length of the electrolyte considered in the numerical model (m)
n_v	number of values for one design variable
q	order of a multivariate polynomial
n_p	number of peaks in the magnetization pattern M_y
n_1	number of odd magnets in a Halbach array
n_2	number of even magnets in a Halbach array

List of abbreviations

LFV	Lorentz Force Velocimetry
PM	permanent magnet
MS	magnet system
MHD	magnetohydrodynamics
SLP	sequential linear programming
AVM	adjoint variable method
Nd-Fe-B	neodymium-iron-boron
FE	finite elements
FEM	finite elements method
DOF	degrees of freedom
CPU	central processing unit
RAM	random access memory
RANS	Reynolds averaged Navier-Stokes
MEF	magnetic and electric field
SQP	sequential quadratic programming
NMR	nuclear magnetic resonance
PDE	partial differential equation
KKT	Karush-Kuhn-Tucker
FEA	finite elements analysis
DV	design variable
RMS	root-mean-square

Chapter 1

Introduction

Nowadays, in many industrial processes there exists a need to measure the flow rate of liquids. The precise measurement of the flow rate provides a reduction of costs and a product improvement. Besides the requirement on high accuracy of a measurement device, it must be flexible and reliable, which favours contactless methods.

Velocimetry in electrically conducting fluids is an old technique, and it is well developed. There are several principles of this technique, e.g.:
-Electric potential Velocimetry (non intrusive but requires contact);
-Lorentz Force Velocimetry (non intrusive and does not require contact) [1].

Lorentz Force Velocimetry (LFV) is a method by which the flow rate of electrically conducting fluids can be measured without physical contact. The interaction between fluid flow and constant transversal magnetic field is what underlies LFV in principle (see Figure 1.1(a)). The Figure shows the fluid flowing with a certain velocity $\mathbf{v}$ through the magnetic field $\mathbf{B}$ which is generated by two sets of stationary permanent magnets (PMs) [2].

As Faraday's law indicates, an eddy current $\mathbf{J}$ arises in the flow because there is relative motion between the flow and the primary magnetic field $\mathbf{B}$ [3]. The interaction between this eddy current and the magnetic field $\mathbf{B}$ produces a force which affects the flow, slowing it down. The name given to this braking force is the Lorentz force (F_L). According to Newton's third law (*actio est reactio*), an equal but opposite force will be acting on the magnet system (MS) through which the stream is passing, so that there is measurable drag on the MS. To measure this drag force is to measure the Lorentz force. The Lorentz force will be proportional to the velocity $\mathbf{v}$, the electrical conductivity of the

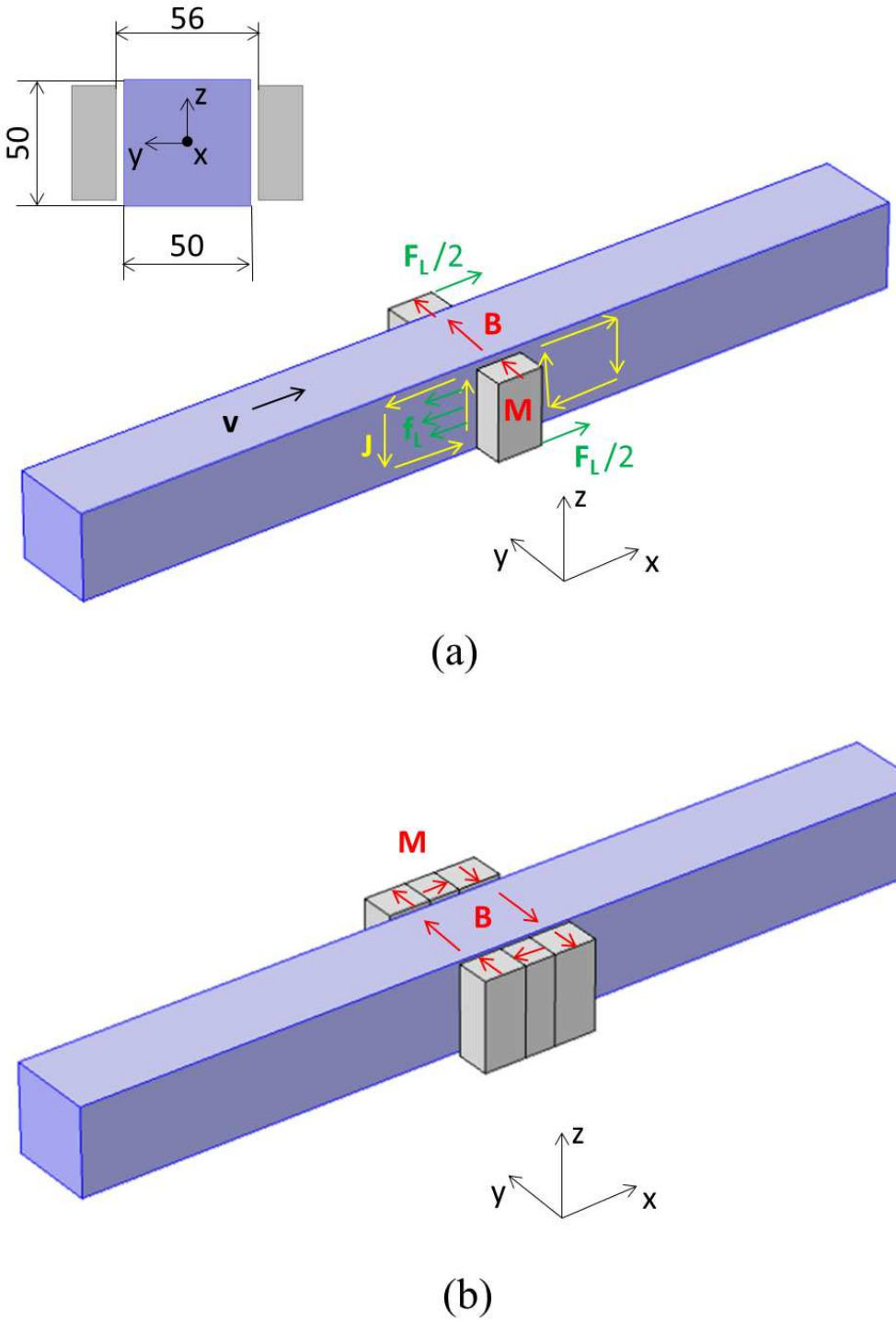

Figure 1.1: Geometry of the problem. The fluid flows with velocity **v**. The magnet system is here represented in two ways: firstly, in (a) by two magnets, one either side of the flow ($N = 1$) and, secondly, in (b) by two Halbach arrays containing three magnets either side of the flow ($N = 3$). An investigation of more complex configurations is also described in this dissertation. Yellow arrows represent the eddy current. Red arrows represent the magnetization and magnetic field. Green arrows represent the Lorentz force density and Lorentz force.

fluid σ, and the square of the magnetic flux density **B** [4]. Thus, if these parameters are known, the flow rate can be derived from the Lorentz force as measured in the MS.

The Lorentz force is widely exploited in industry and in research into magnetohydrodynamics (MHD). For example, the effect of the Lorentz force is used in channel-type induction furnaces to improve the mixing of the melt between the channel and the bath [5]. Another example of the use of F_L is the excitation into movement of liquid metal located in a homogeneous magnetic field. This is done by injecting electric current into this liquid metal [6]. The Hartmann number ($Ha = L \cdot B\sqrt{\sigma/(\rho\nu)}$) is used to estimate how strongly the liquid melt is affected by F_L. Here, L is the characteristic dimension, B is the characteristic magnetic field and σ, ρ and ν are respectively the electrical conductivity, density and kinematic viscosity of the fluid. For example, in [6] this number was in a range between 13.5 and 36. For the electrolyte under consideration in the present work $Ha < 1$ because of much lower electric conductivity, which means that the effect of the F_L on the flow is negligible and need not be taken into account.

LFV is a technique well-suited to measuring the flow rate of liquid metals [7], [8]. In the aluminum production process, LFV can be used to measure the flow rate in casting channels or casting ducts, so that the melt can be more accurately dosed during casting [9]. The present dissertation on "Numerical simulation and optimization of the magnet system for the Lorentz Force Velocimetry of low-conducting materials" is, however, part of a project which aims to develop LFV for electrolytes [10], [11]. For electrolytes, the Lorentz force is expected to be approximately a million times smaller than for liquid metals located in a similar magnetic field, since the electrical conductivity of electrolytes is about 6 orders of magnitude smaller than that of liquid metals. The expected value of the Lorentz force for the electrolyte under consideration lies between 10 and 100 μN.

If the channel cross-section dimensions and the distance between the magnets are fixed, then there are only two ways of increasing the Lorentz force. First, the velocity of the flow can be increased and, second, the magnetic field can be optimized. Magnetic field optimization is achieved by changing of the direction of the magnetization and the dimensions of the magnets. These two options are studied in the frame of this work.

Optimization of the magnetization directions of a permanent magnet array for an eddy current brake system was accomplished in 2010 by Choi et al., who designed a 2D finite element model and used sequential linear programming (SLP) and the adjoint variable method (AVM) to maximize the braking force [12]. The optimized magnetization

pattern corresponds with that of a Halbach array, which is described in [13].

Since the measurement system in use for the current research requires the weight of the MS to be less than 1 kg and the Lorentz force to be higher than 10 μN, the only way of generating a relatively high magnetic field is to use permanent magnets [14], [15]. As material for the permanent magnets, neodymium-iron-boron (Nd-Fe-B) was selected because of its high magnetization.

The parameters selected in the current investigation are as follows:

- electrolyte velocity v = 5 m/s (solid body approximation),
- electrolyte electrical conductivity $\sigma = 4$ S/m,
- electrolyte cross-section area $S = 0.05$ m $\times$ 0.05 m,
- distance between the magnets $D = 0.056$ m,
- remanence of the permanent magnets $B_r = 1.09$ T.

Unless otherwise stated, the results of this work were obtained using these data.

This dissertation consists of five chapters. In Chapter 2 the system of governing equations and boundary conditions are discussed. Chapter 3 is devoted to description, verification and validation of the numerical model of the LFV. In Chapter 4 the optimization algorithm for the magnet system is described and the results of optimization are presented. Finally, Chapter 5 concludes the results of this work.

Chapter 2

Problem formulation

2.1 Governing equations

2.1.1 The general differential form

Maxwell's equations are a set of fundamental equations governing all macroscopic electromagnetic phenomena [16]. For general time-varying fields, Maxwell's equations in differential form can be written as

$$\nabla \times \mathbf{E} + \frac{\partial \mathbf{B}}{\partial t} = 0, \qquad \text{(Faraday's law)} \tag{2.1}$$

$$\nabla \times \mathbf{H} - \frac{\partial \mathbf{D}}{\partial t} = \mathbf{J}, \qquad \text{(Maxwell-Ampere law)} \tag{2.2}$$

$$\nabla \cdot \mathbf{D} = \rho, \qquad \text{(Gauss's law)} \tag{2.3}$$

$$\nabla \cdot \mathbf{B} = 0, \qquad \text{(Gauss's law - magnetic)} \tag{2.4}$$

where $\mathbf{E}$ is the electric field intensity (V/m), $\mathbf{D}$ the electric flux density (C/m^2), $\mathbf{H}$ the magnetic field intensity (A/m), $\mathbf{B}$ the magnetic flux density (Wb/m^2), $\mathbf{J}$ the electric current density (A/m^2), and ρ the electric charge density (C/m^3).

Besides the Maxwell's system of equations there is another fundamental equation, which specifies the conservation of charge, and can be written as

$$\nabla \cdot \mathbf{J} = -\frac{\partial \rho}{\partial t}. \qquad \text{(continuity equation)} \tag{2.5}$$

Only three equations of the above five, (2.1)-(2.5), are independent and thus called independent equations. Either the equations (2.1)-(2.3), or the equations (2.1), (2.2), and (2.5) can be chosen as such independent equations.

2.1.2 Magnetostatic field equations

In case of a static field, i.e. when the field quantities do not vary with time, equations (2.1), (2.2), and (2.5) will be as follows:

$$\nabla \times \mathbf{E} = 0, \tag{2.6}$$

$$\nabla \times \mathbf{H} = \mathbf{J}, \tag{2.7}$$

$$\nabla \cdot \mathbf{J} = 0. \tag{2.8}$$

Equations (2.3) and (2.4) remain valid.

2.1.3 Constitutive relations

The system of Maxwell's equations is indefinite, since the number of unknowns exceeds the number of equations. To overcome this problem the constitutive relations are used which describe the macroscopic properties of the medium being investigated. They are as follows:

$$\mathbf{D} = \epsilon \mathbf{E}, \tag{2.9}$$

$$\mathbf{B} = \mu_0(\mathbf{H} + \mathbf{M}) \quad or \quad \mathbf{B} = \mu_0 \mu_r \mathbf{H} + \mathbf{B}_r, \tag{2.10}$$

$$\mathbf{J} = \sigma(\mathbf{E} + \mathbf{v} \times \mathbf{B}), \tag{2.11}$$

where ϵ, μ_r, and σ denote the permittivity (F/m), relative permeability, and conductivity (S/m) respectively of the medium. These parameters are tensors for anisotropic media and scalars for isotropic media. They are functions of position for inhomogeneous media and constants for homogeneous media. Further, $\mu_0 = 4\pi \cdot 10^{-7}$ H/m is the absolute permeability, $\mathbf{M}$ magnetization (A/m), and $\mathbf{B}_r$ remanence (T = Wb/m^2) of the medium. Equation (2.11) is Ohm's law taking into account the motional eddy currents due to relative motion between conductor and magnetic field and making use of the term $\mathbf{v} \times \mathbf{B}$.

2.2 Scalar and vector potentials

To solve Maxwell's equations, one should convert them into second order differential equations involving only one field quantity.

2.2.1 Scalar potential of the electrostatic field

The electrostatic field is governed by equations (2.3) and (2.6). The latter equation is satisfied by representing the electric field intensity $\mathbf{E}$ as

$$\mathbf{E} = -\nabla\phi, \tag{2.12}$$

where ϕ is the scalar potential.

2.2.2 Vector potential of the magnetostatic field

The magnetostatic field is governed by equations (2.4) and (2.7). Equation (2.4) is satisfied by representing the magnetic flux density $\mathbf{B}$ as

$$\mathbf{B} = \nabla \times \mathbf{A}, \tag{2.13}$$

where $\mathbf{A}$ is the vector potential. Substituting (2.13) and (2.10) into (2.7) yields the second order differential equation

$$\nabla \times \Big(\frac{1}{\mu}(\nabla \times \mathbf{A}) - \mathbf{M}\Big) = \mathbf{J}. \tag{2.14}$$

Equation (2.14) does not define $\mathbf{A}$ uniquely, because any function $\mathbf{A'} = \mathbf{A} + \nabla f$ is also a solution to the equation (2.14) for any f. To determine $\mathbf{A}$ uniquely an additional condition is required. This condition, which is also called as *gauge condition*, can be written as follows:

$$\nabla \cdot \mathbf{A} = 0. \tag{2.15}$$

2.3 Final system of equations

The final system of equations governing the problem described in Chapter 1 includes the equations (2.7), (2.8), (2.10), (2.11), (2.12), and (2.13). After some reformulations this system of equations can be written as follows:

$$\nabla \times \Big(\frac{1}{\mu}(\nabla \times \mathbf{A}) - \mathbf{M}\Big) - \sigma \mathbf{v} \times (\nabla \times \mathbf{A}) + \sigma \nabla \phi = 0, \tag{2.16}$$

$$\nabla \cdot [-\sigma \nabla \phi + \sigma \mathbf{v} \times (\nabla \times \mathbf{A})] = 0. \tag{2.17}$$

This type of formulation, which is also called *the quasi-static approach*, was successfully used in [17] to analyze changes of drag force on a permanent magnet (PM) moving along an electrically conducting plate with different spatial defects.

The Lorentz force density is the cross-product of the eddy current density and the magnetic flux density in the electrolyte. This can be expressed in terms of potential functions:

$$\mathbf{f_L} = \mathbf{J} \times \mathbf{B} = \sigma(\mathbf{v} \times (\nabla \times \mathbf{A}) - \nabla \phi) \times (\nabla \times \mathbf{A}). \tag{2.18}$$

The Lorentz force is the volume integral of the Lorentz force density:

$$\mathbf{F_L} = \int_V \mathbf{f_L} dV. \tag{2.19}$$

2.4 Boundary conditions

To solve the system of equations (2.16)-(2.17) the boundary conditions are necessary. At the interface between two media the so-called *continuity* boundary conditions are used [18], [19]:

$$\mathbf{n} \times (\mathbf{H}_1 - \mathbf{H}_2) = 0, \tag{2.20}$$

$$\mathbf{n} \cdot (\mathbf{J}_1 - \mathbf{J}_2) = 0, \tag{2.21}$$

where $\mathbf{n}$ is the normal unit vector on the boundary, and subscripts 1 and 2 denote the field properties inside and outside the boundary. For the external boundary, the magnetic

insulation and electric ground boundary conditions are applied

$$\mathbf{n} \times \mathbf{A} = 0, \tag{2.22}$$

$$\phi = 0. \tag{2.23}$$

2.5 Nondimensional system of equations for solid bar

To obtain a nondimensional system of equations it is necessary to define characteristic values of the parameters which are included in the system of equations (2.16)-(2.17). These values are as follows: $L = 0.05$ m (characteristic length), $\mu_0 = 4\pi 10^{-7}$ H/m (permeability of vacuum), $M_0 = B_r/\mu_0$=867394.44 A/m (characteristic magnetization of the magnets), $V_0 = 5$ m/s (characteristic electrolyte velocity), $\sigma = 4$ S/m (characteristic electrolyte conductivity), $F_0 = \sigma V_0 \mu_0^2 M_0^2 L^3 = 2.97025 \cdot 10^{-3}$ N (characteristic Lorentz force), and $m_0 = \rho \cdot L^3 = 0.9375$ kg (characteristic MS weight), where $\rho = 7500$ kg/m^3 is the density of the magnet material.

Now we can relate our problem parameters to the characteristic numbers as follows: $x = L \cdot \tilde{x}$, $y = L \cdot \tilde{y}$, $z = L \cdot \tilde{z}$, $\nabla = \tilde{\nabla}/L$, $\tilde{\nabla} = (\partial/\partial\tilde{x}, \partial/\partial\tilde{y}, \partial/\partial\tilde{z})^T$, $\mathbf{v} = V_0 \cdot \tilde{\mathbf{v}}$, $\mathbf{M} = M_0 \cdot \tilde{\mathbf{M}}$, $\mathbf{A} = \mu_0 M_0 L \cdot \tilde{\mathbf{A}}$, $\mathbf{H} = M_0 \cdot \tilde{\mathbf{H}}$, $\mathbf{B} = \mu_0 M_0 \cdot \tilde{\mathbf{B}}$, $\phi = \mu_0 V_0 M_0 L \cdot \tilde{\phi}$, and $\mathbf{J} = \sigma \mu_0 V_0 M_0 \cdot \tilde{\mathbf{J}}$. Here, parameters denoted with a tilde are nondimensional. After substitution of these relations into the system of equations (2.16)-(2.17) we obtain the nondimensional system of equations:

$$\tilde{\nabla} \times (\tilde{\nabla} \times \tilde{\mathbf{A}} - \tilde{\mathbf{M}}) = Rm(\tilde{\mathbf{v}} \times \tilde{\nabla} \times \tilde{\mathbf{A}} - \tilde{\nabla}\tilde{\phi}), \tag{2.24}$$

$$\tilde{\nabla} \cdot \tilde{\nabla}\tilde{\phi} = \tilde{\nabla} \cdot (\tilde{\mathbf{v}} \times \tilde{\nabla} \times \tilde{\mathbf{A}}). \tag{2.25}$$

The right hand side in equation (2.24) can be neglected, in the frame of the low Rm approximation (see [20] for its full derivation), since the magnetic Reynolds number $Rm = \sigma\mu V_0 L \approx 1.3 \cdot 10^{-6} \ll 1$ [21]. Physically, this equates to assuming that currents are generated by the interaction between the flow and the magnetic field but that although these currents are sufficiently strong to generate a Lorentz force that cannot be neglected, the magnetic field which they induce (through Ampere's law (2.7)) is very small compared to the externally generated one (here the field generated by the permanent magnets).

Consequently, the external magnetic field can be considered as imposed on the flow and $\tilde{\mathbf{A}}$ is solely determined by the electromagnetic quantities and the geometry. The electric potential $\tilde{\phi}$ on the other hand is determined by the current generated in the flow and still depends on $\tilde{\mathbf{v}}$. This approximation has been tested in a number of configurations, and has been found to lead to results that are practically indistinguishable from solutions of the full equations as soon as $Rm < 0.1$, as in duct flows [22]. The main benefit of the low-Rm approximation is that $\tilde{\mathbf{A}}$ and $\tilde{\phi}$ are mathematically decoupled, and can be calculated by first solving a simpler version of (2.24):

$$\tilde{\nabla} \times (\tilde{\nabla} \times \tilde{\mathbf{A}} - \tilde{\mathbf{M}}) = 0 \tag{2.26}$$

and then solving (2.25) using the solution of (2.26) for $\tilde{\mathbf{A}}$.
In other words, the system of equations (2.25)-(2.26) can be solved in two steps: first, equation (2.26) is solved in all problem subdomains regarding $\tilde{\mathbf{A}}$ and, second, equation (2.25) is solved only inside the electrolyte regarding $\tilde{\phi}$ for a given $\tilde{\mathbf{A}}$. Boundary conditions (2.20)-(2.23) stay unchanged. The only difference is that instead of dimensional parameters nondimensional ones are used.

2.6 Symmetry conditions

In the case of the magnet system with two permanent magnets magnetized along the y axis (see Figure 1.1(a)) only one quarter of the full geometry can be considered as shown in Figure 2.1(a). Here, the boundary conditions (2.22)-(2.23) were applied on the symmetry plane $z = 0$ and additional boundary conditions on the symmetry plane $y = 0$ were applied as follows:

$$\mathbf{n} \times \mathbf{H} = 0, \tag{2.27}$$

$$\mathbf{n} \cdot \mathbf{J} = 0. \tag{2.28}$$

In the case of the magnet system with two Halbach arrays only symmetry with respect to the $z = 0$ symmetry plane can be used with boundary conditions (2.22-2.23), because the magnetization directions inside the magnets are nonsymmetric with respect

to the $x = 0$ and $y = 0$ symmetry planes (see Figures 1.1(b) and 2.1(b)).

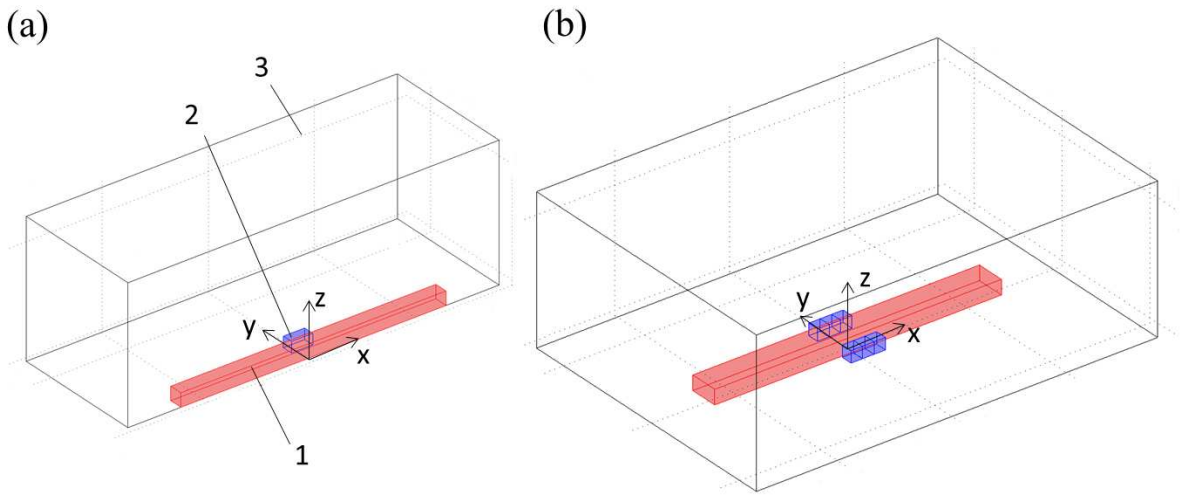

Figure 2.1: 1/4 of the full geometry for the magnet system containing two magnets (a) and 1/2 of the full geometry for the magnet system containing six magnets (b): 1 - electrolyte, 2 - magnet, 3 - air.

2.7 The solid bar approximation

Until now, only the electromagnetic part of the problem has been considered. To complete the system of equations, the Navier-Stokes equations which govern the evolution of velocity and pressure distributions in the duct should be added. In practical applications where the flow rate is high, the flow in the duct is turbulent, with intense fluctuations. The precise calculation of such a flow is a daunting challenge in its own right, which, fortunately, we did not need to face for the purpose of this work. As mentioned in section 2.5, in the low-Rm approximation, the magnetic flux $\mathbf{B}$ is independent of the velocity field $\mathbf{v}$, so the Lorentz force (2.18) only depends on $\mathbf{v}$ through the electric current $\mathbf{J}$. This dependence is linear, and therefore that of $\mathbf{F}_L$ on $\mathbf{v}$ is linear. This implies that the fluctuations of $\mathbf{v}$ do not contribute to the time-average of $\mathbf{F}_L$, and that only the time average of $\mathbf{v}$ does. Since the typical mean velocity profile of a turbulent duct flow is essentially flat in the bulk of the flow, with boundary layers of thickness δ developing along each of the duct walls, with $\delta \ll L$, the local error on $\mathbf{v}$ incurred by assuming that the flow behaves like a solid, moving at velocity $\mathbf{v} = V_0\mathbf{e}_x$ and, in turn on $\mathbf{F}_L$, is therefore of order δ/L. In section 3.4 it will be shown that the error in the calculated flow rate incurred by replacing the exact turbulent flow profile with a constant velocity profile

across the duct was significantly smaller than the degree of precision expected from the measurement system. On these grounds, we used this assumption, which removes the need for solving the full turbulent Navier-Stokes equations for a minute cost in terms of the final precision.

Chapter 3

Description of the numerical model

In this Chapter the numerical model will be described, starting with the basic steps of the Finite Element Method. Second, it will be shown how the numerical model was verified, by comparing its results with an analytical solution. Third, the validation of the numerical model will be shown. This was done by comparing the model's results with experimental data.

3.1 Basic steps of the Finite Element Method

The finite element method is a numerical technique for obtaining approximate solutions to boundary-value problems. In general, a boundary-value problem is defined by a governing differential equation in a domain Ω

$$\mathfrak{L}\phi = f \tag{3.1}$$

together with the boundary conditions on the boundary Γ that encloses the domain. In (3.1), $\mathfrak{L}$ is a differential operator, f the excitation function, and ϕ the unknown quantity.

The principle of the method is to replace an entire continuous domain by a number of subdomains called elements in which the unknown function is represented by simple interpolation functions with unknown coefficients. Thus, the original boundary-value problem with an infinite number of degrees of freedom is converted into a problem with a finite number of degrees of freedom. The solution of the whole system is approximated by a finite number of unknown coefficients. Then a set of algebraic equations or a system of equations is obtained by applying the Ritz variational or Galerkin procedure. Solution of the boundary-value problem is achieved by solving the system of equations. A finite

element analysis of a boundary-value problem includes the following steps:

1. Discretization or subdivision of the domain;
2. Selection of the interpolation functions;
3. Formulation of the system of equations;
4. Solution of the system of equations.

3.1.1 Domain discretization

The entire domain Ω is subdivided into a number of small domains Ω^e $(e = 1, ..., M)$, with M denoting the total number of subdomains or elements. In a three-dimensional consideration, the domain may be subdivided into tetrahedra, triangular prisms, or rectangular bricks, among which the tetrahedra are the simplest and best suited for arbitrary volume domains. The problem is formulated in terms of the unknown function ϕ at nodes associated with the elements. For implementation purposes, it is necessary to describe these nodes. A complete description of a node contains its coordinate values, local number, and global number. Numbering of nodes and elements requires some strategy. The finite element formulation usually results in a banded matrix whose bandwidth is determined by the maximum difference between the global numbers of two nodes in an element. Thus, the computer storage and processing cost can be reduced significantly by properly numbering the nodes to minimize the bandwidth.

3.1.2 Selection of interpolation functions

The COMSOL interpolation function serves to approximate an unknown solution within an element. The interpolation is usually selected to be a polynomial of 1^{st} (linear), 2^{nd} (quadratic), or higher order. Higher-order polynomials are more accurate but result in a more complicated formulation. Therefore, the simple linear or quadratic interpolation is widely used. An interpolated expression for the unknown solution in an element e is as follows:

$$\tilde{\phi}^e = \sum_{j=1}^{n} N_j^e \phi_j^e = \{N^e\}^T \{\phi^e\} = \{\phi^e\}^T \{N^e\} \tag{3.2}$$

where n is the number of nodes in the element, ϕ_j^e the value of ϕ at node j of the element, and N_j^e the interpolation function, which is also known as the expansion or basis function.

The highest order of N_j^e is referred to as the order of the element. E.g. if N_j^e is a linear function, the element e is a linear element. An important feature of the functions N_j^e is that they are nonzero only within element e, and vanish outside this element.

3.1.3 Formulation of the system of equations

According to Galerkin's method [16], for (3.1), the weighted residual for the eth element is given by

$$R_i^e = \int_{\Omega^e} N_i^e(\mathfrak{L}\tilde{\phi}^e - f)d\Omega, \qquad i = 1, 2, 3, ..., n. \tag{3.3}$$

Substituting (3.2) into (3.3) yields

$$R_i^e = \int_{\Omega^e} N_i^e \mathfrak{L}\{N^e\}^T d\Omega\{\phi^e\} - \int_{\Omega^e} f N_i^e d\Omega, \qquad i = 1, 2, 3, ..., n, \tag{3.4}$$

which can be written in matrix form as

$$\{R^e\} = [K^e]\{\phi^e\} - \{b^e\}. \tag{3.5}$$

Here $\{R^e\} = [R_1^e, R_2^e, ..., R_n^e]^T$, $[K^e]$ is an $n \times n$ matrix and $\{b^e\}$ an $n \times 1$ column vector with their elements given by

$$K_{ij}^e = \int_{\Omega^e} N_i^e \mathfrak{L} N_j^e d\Omega, \tag{3.6}$$

$$b_i^e = \int_{\Omega^e} f N_i^e d\Omega. \tag{3.7}$$

The operator $\mathfrak{L}$ is not required to be self-adjoint here. Thus, the elemental matrix $[K^e]$ is not necessarily symmetric. The weighted residual R_i associated with node i is a summation over the elements directly connected to node i. Therefore, we may expand (3.5) using the local and global relations and then sum it over each element

$$\{R\} = \sum_{e=1}^{M} \{\bar{R}^e\} = \sum_{e=1}^{M} ([\bar{K}^e]\{\bar{\phi}^e\} - \{\bar{b}^e\}). \tag{3.8}$$

The system of equations can then be obtained by setting (3.8) to zero

$$\sum_{e=1}^{M}([\bar{K}^e]\{\bar{\phi}^e\} - \{\bar{b}^e\}) = \{0\}, \tag{3.9}$$

or in matrix form:

$$[K]\{\phi\} = \{b\}. \tag{3.10}$$

This system of equations is solved by applying the required boundary conditions.

3.1.4 Solution of the system of equations

The resultant system of equations (3.10) can be solved using either a direct or an iterative method to find an unknown vector $\{\phi\}$. From this vector another parameters such as **B**, **H**, **J**, etc. can be derived.

The AC/DC module of the commercial software COMSOL Multiphysics was used to solve the system of partial differential equations (2.25)-(2.26) submitted to boundary conditions (2.20)-(2.23) and symmetry boundary conditions (2.27)-(2.28) [23]. The iterative FGMRES (flexible generalised minimum residual) solver was used as the linear system solver [24],[25]. The relative tolerance of the linear system solver was set to 10^{-6}. The *geometric multigrid* was used as a preconditioner of the linear system solver [26]. The successive over-relaxation methods SOR and SORU were chosen as a presmoother and postsmoother, respectively, for the preconditioner of the linear system solver [24]. The iterative GMRES (generalised minimum residual) solver was used as the coarse solver for the preconditioner of the linear system solver [27], [28]. Finally, the SSOR (symmetric successive over-relaxation method) was used as the preconditioner of the coarse solver [24].

3.1.5 Workstation description

Almost all computations in the context of this work were performed on a workstation with the following features:

- Operating system: Windows 7 Professional SP1 64-bit;

- Random access memory: 24 GB;

- Processor: Intel(R) Core (TM) i7 CPU 920 @ 2.67 GHz.

3.2 Verification of the numerical model concerning the magnetic field

In this section, the analytical methods will be described by which the magnetic field near the rectangular permanent magnet with known homogeneous magnetization distribution along one predefined direction was determined. There follows a description of the numerical model for this problem and the results from all methods are compared.

3.2.1 Method based on the distribution of the electric current [29], [30]

The magnetic field in the vicinity of the permanent magnet, if its magnetization is known, can be calculated using equivalent system of volume and surface microscopic Ampere's currents $\mathbf{J_a}$ and $\mathbf{J_{sa}}$, which are defined as

$$\mathbf{J_a}(\mathbf{r'}) = \nabla \times \mathbf{M}(\mathbf{r'}), \tag{3.11}$$

$$\mathbf{J_{sa}}(\mathbf{r'}) = \mathbf{M}(\mathbf{r'}) \times \hat{\mathbf{n}}, \tag{3.12}$$

where $\hat{\mathbf{n}}$ is unit vector normal to the surface of the magnet (see Figure 3.1).

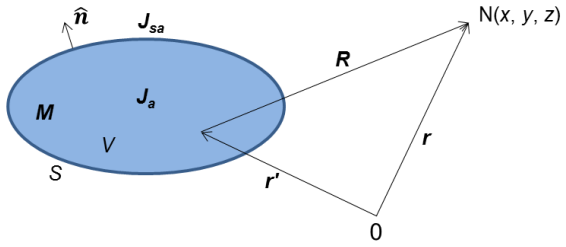

Figure 3.1: Sketch for the computation of the magnetic field near a permanent magnet.

The magnetic vector potential is related to these currents as

$$\mathbf{A}(\mathbf{r}) = \frac{\mu_0}{4\pi} \int_V \mathbf{J_a}(\mathbf{r'}) \frac{dV'}{R} + \frac{\mu_0}{4\pi} \oint_S \mathbf{J_{sa}}(\mathbf{r'}) \frac{dS'}{R}, \tag{3.13}$$

where $\mathbf{R} = |\mathbf{r} - \mathbf{r'}| = \sqrt{(x-x')^2 + (y-y')^2 + (z-z')^2}$.

Finally, magnetic flux density is determined using (2.13). In respect of the rectan-

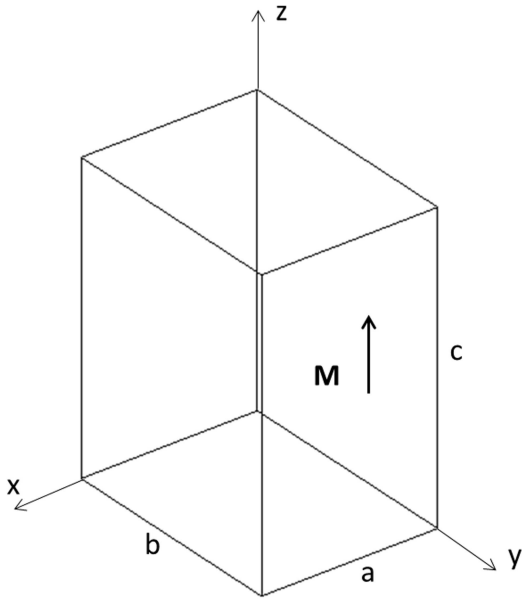

Figure 3.2: Rectangular permanent magnet. M denotes the magnetization, a, b and c denote the dimensions of the magnet along the x, y and z axes.

gular permanent magnet in Figure 3.2, the equation (3.13) can be rewritten as

$$\mathbf{A}(\mathbf{r}) = \frac{\mu_0}{4\pi} \oint_S \mathbf{M}(\mathbf{r'}) \times \hat{\mathbf{n}} \frac{dS'}{R}. \tag{3.14}$$

Further, decomposing $\mathbf{M} \times \hat{\mathbf{n}} = \begin{vmatrix} \hat{\mathbf{x}} & \hat{\mathbf{y}} & \hat{\mathbf{z}} \\ M_x & M_y & M_z \\ n_x & n_y & n_z \end{vmatrix} = \hat{\mathbf{x}}(n_z M_y - n_y M_z) + \hat{\mathbf{y}}(n_x M_z - n_z M_x) + \hat{\mathbf{z}}(n_y M_x - n_x M_y)$

$\mathbf{M} \times \hat{\mathbf{n}}$ on each surface of the magnet is found:

$\mathbf{M} \times \hat{\mathbf{n}}(y = b) = -n_y M_z \cdot \hat{\mathbf{x}}$,

$\mathbf{M} \times \hat{\mathbf{n}}(y = 0) = n_y M_z \cdot \hat{\mathbf{x}}$,

$\mathbf{M} \times \hat{\mathbf{n}}(x = a) = n_x M_z \cdot \hat{\mathbf{y}}$,

$\mathbf{M} \times \hat{\mathbf{n}}(x = 0) = -n_x M_z \cdot \hat{\mathbf{y}}$,

$\mathbf{M} \times \hat{\mathbf{n}}(z = c) = 0$,

$\mathbf{M} \times \hat{\mathbf{n}}(z = 0) = 0$.

Now (3.14) can be written as

$$\mathbf{A}(\mathbf{r}) = \frac{\mu_0 M}{4\pi}(-\int_0^a \int_0^c \frac{dx'dz'}{\sqrt{(x-x')^2+(y-b)^2+(z-z')^2}} + \int_0^a \int_0^c \frac{dx'dz'}{\sqrt{(x-x')^2+(y-0)^2+(z-z')^2}})\hat{\mathbf{x}} + \frac{\mu_0 M}{4\pi}(\int_0^b \int_0^c \frac{dy'dz'}{\sqrt{(x-a)^2+(y-y')^2+(z-z')^2}} - \int_0^b \int_0^c \frac{dy'dz'}{\sqrt{(x-0)^2+(y-y')^2+(z-z')^2}})\hat{\mathbf{y}}. \quad (3.15)$$

In (3.15) we deal with the integral which can be decomposed as follows:

$$I(\alpha, x_1, y_1, x_2, y_2) = \int_{x_1}^{x_2} \int_{y_1}^{y_2} \frac{dxdy}{\sqrt{\alpha^2+x^2+y^2}} = x_2 ln\frac{y_2+\sqrt{\alpha^2+x_2^2+y_2^2}}{y_1+\sqrt{\alpha^2+x_2^2+y_1^2}} + x_1 ln\frac{y_1+\sqrt{\alpha^2+x_1^2+y_1^2}}{y_2+\sqrt{\alpha^2+x_1^2+y_2^2}} + y_2 ln\frac{x_2+\sqrt{\alpha^2+x_2^2+y_2^2}}{x_1+\sqrt{\alpha^2+x_1^2+y_2^2}} + y_1 ln\frac{x_1+\sqrt{\alpha^2+x_1^2+y_1^2}}{x_2+\sqrt{\alpha^2+x_2^2+y_1^2}} + |\alpha| arctg\frac{y_2 x_1}{|\alpha|\sqrt{\alpha^2+x_1^2+y_2^2}} - |\alpha| arctg\frac{y_2 x_2}{|\alpha|\sqrt{\alpha^2+x_2^2+y_2^2}} + |\alpha| arctg\frac{y_1 x_2}{|\alpha|\sqrt{\alpha^2+x_2^2+y_1^2}} - |\alpha| arctg\frac{y_1 x_1}{|\alpha|\sqrt{\alpha^2+x_1^2+y_1^2}}. \quad (3.16)$$

Now the magnetic vector potential in any point with coordinates (x, y, z) can be determined as

$\mathbf{A} = A_x(x,y,z)\cdot\hat{\mathbf{x}} + A_y(x,y,z)\cdot\hat{\mathbf{y}}$, where

$A_x = \frac{\mu_0 M}{4\pi}[I(y,x,z,x-a,z-c) - I(y-b,x,z,x-a,z-c)]$ and

$A_y = \frac{\mu_0 M}{4\pi}[I(x-a,z,y,z-c,y-b) - I(x,z,y,z-c,y-b)]$.

The magnetic flux density is determined in accordance with (2.13) as follows:

$$\mathbf{B} = \begin{vmatrix} \hat{\mathbf{x}} & \hat{\mathbf{y}} & \hat{\mathbf{z}} \\ \frac{\partial}{\partial x} & \frac{\partial}{\partial y} & \frac{\partial}{\partial z} \\ A_x & A_y & 0 \end{vmatrix} = B_x\cdot\hat{\mathbf{x}} + B_y\cdot\hat{\mathbf{y}} + B_z\cdot\hat{\mathbf{z}}, \text{ where}$$

$B_x = -\frac{\partial A_y(x,y,z)}{\partial z}$, $B_y = \frac{\partial A_x(x,y,z)}{\partial z}$, and $B_z = \frac{\partial A_y(x,y,z)}{\partial x} - \frac{\partial A_x(x,y,z)}{\partial y}$.

3.2.2 Method based on the distribution of the charge [13]

For current-free regions $\nabla \times \mathbf{H} = 0$ and $\nabla \cdot \mathbf{B} = 0$. The irrotational field $\mathbf{H}$ can be expressed using a scalar magnetic potential ϕ_m as

$$\mathbf{H} = -\nabla\phi_m. \tag{3.17}$$

Substituting (3.17) and the constitutive relation $\mathbf{B} = \mu_0(\mathbf{H}+\mathbf{M})$ into $\nabla\cdot\mathbf{B} = 0$ we obtain

$$\nabla^2\phi_m = \nabla \cdot \mathbf{M}. \tag{3.18}$$

We can represent the solution of (3.18) in the integral form using the free space Green's function G(**x**,**x'**)

$$\phi_m(\mathbf{x}) = \int G(\mathbf{x}, \mathbf{x'})\nabla' \cdot \mathbf{M}(\mathbf{x'})dv' = -\frac{1}{4\pi}\int \frac{\nabla' \cdot \mathbf{M}(\mathbf{x'})}{|\mathbf{x} - \mathbf{x'}|}dv', \tag{3.19}$$

where **x** is the observation point and **x'** is the source point. If **M** is confined to a volume V and falls abruptly to zero outside of this volume, (3.19) becomes

$$\phi_m(\mathbf{x}) = -\frac{1}{4\pi}\int_V \frac{\nabla' \cdot \mathbf{M}(\mathbf{x'})}{|\mathbf{x} - \mathbf{x'}|}dv' + \frac{1}{4\pi}\oint_S \frac{\mathbf{M}(\mathbf{x'}) \cdot \hat{\mathbf{n}}}{|\mathbf{x} - \mathbf{x'}|}ds', \tag{3.20}$$

where S is the surface that bounds V, and $\hat{\mathbf{n}}$ is the outward unit normal to S. In (3.20) $\rho_m = -\nabla \cdot \mathbf{M}$ is the volume charge density and $\sigma_m = \mathbf{M} \cdot \hat{\mathbf{n}}$ is the surface charge density.

If the magnet is in free space, $\mathbf{B} = \mu_0\mathbf{H}$ and from (3.17) and (3.20) we have

$$\mathbf{B}(\mathbf{x}) = \frac{\mu_0}{4\pi}\int_V \frac{\rho_m(\mathbf{x'})(\mathbf{x} - \mathbf{x'})}{|\mathbf{x} - \mathbf{x'}|^3}dv' + \frac{\mu_0}{4\pi}\oint_S \frac{\sigma_m(\mathbf{x'})(\mathbf{x} - \mathbf{x'})}{|\mathbf{x} - \mathbf{x'}|^3}ds'. \tag{3.21}$$

Assuming that the magnetization is $\mathbf{M} = M_s\hat{\mathbf{z}}$ and choosing a coordinate system located at the center of the magnet, one can denote the positions of the edges of the magnet with respect to the x, y, and z axes as $(x_1,\ x_2)$, $(y_1,\ y_2)$, $(z_1,\ z_2)$, respectively. First, the magnet is reduced to an equivalent charge distribution. Since **M** is irrotational, the volume charge density is zero, $\rho_m = -\nabla \cdot \mathbf{M} = 0$. There exists a surface charge density

$$\sigma_m = \begin{cases} M_s & (z = z_2) \\ -M_s & (z = z_1). \end{cases}$$

The **B**-field follows from (3.21)

$$\mathbf{B}(x,y,z) = \frac{\mu_0 M_s}{4\pi} \sum_{k=1}^{2} (-1)^k \int_{y_1}^{y_2} \int_{x_1}^{x_2} \frac{[(x-x')\hat{\mathbf{x}} + (y-y')\hat{\mathbf{y}} + (z-z_k)\hat{\mathbf{z}}]dx'dy'}{[(x-x')^2 + (y-y')^2 + (z-z_k)^2]^{3/2}}. \quad (3.22)$$

The z-component of the **B**-field is given by

$$B_z(x,y,z) = -\frac{\mu_0 M_s}{4\pi} \sum_{k=1}^{2} (-1)^k \int_{y_1}^{y_2} \int_{x_1}^{x_2} \frac{(z-z_k)dx'dy'}{[(x-x')^2 + (y-y')^2 + (z-z_k)^2]^{3/2}}. \quad (3.23)$$

The x' integration is performed using a change of variable $\alpha = x - x'$,

$$B_z(x,y,z) = -\frac{\mu_0 M_s}{4\pi} \int_{y_1}^{y_2} \int_{x-x_1}^{x-x_2} \frac{z-z_k}{[\alpha^2 + (y-y')^2 + (z-z_k)^2]^{3/2}} d\alpha dy' =$$
$$\frac{\mu_0 M_s}{4\pi} \sum_{k=1}^{2} \sum_{n=1}^{2} (-1)^{k+n+1} (z-z_k)(x-x_n) \times$$
$$\int_{y_1}^{y_2} \frac{dy'}{[(y-y')^2 + (z-z_k)^2]\sqrt{(y-y')^2 + (x-x_n)^2 + (z-z_k)^2}}. \quad (3.24)$$

The remaining y' integration is performed using a change of variable $\gamma = y - y'$. This gives

$$B_z(x,y,z) = \frac{\mu_0 M_s}{4\pi} \sum_{k=1}^{2} \sum_{n=1}^{2} \sum_{m=1}^{2} (-1)^{k+n+m} \times$$
$$\arctan\Big[\frac{(x-x_n)(y-y_m)}{(z-z_k)[(x-x_n)^2 + (y-y_m)^2 + (z-z_k)^2]^{1/2}}\Big]. \quad (3.25)$$

3.2.3 Numerical model

The numerical model was developed using COMSOL Multiphysics. The model is governed by (2.16) and (2.17) as well as by boundary conditions (2.20)-(2.23). It consists of two subregions: magnet and air (see Figure 3.3). The rectangular magnet is magnetized along the z axis and has the dimensions a, b, and c along the x, y, and z axes respectively, as shown in Figure 3.2. We used two types of vector Lagrange elements: quadratic in model 1 and cubic in model 2. As shown in Figure 3.3, the magnet is located at the center of the air region which is a cube with the linear dimensions equal to 0.5 m. The

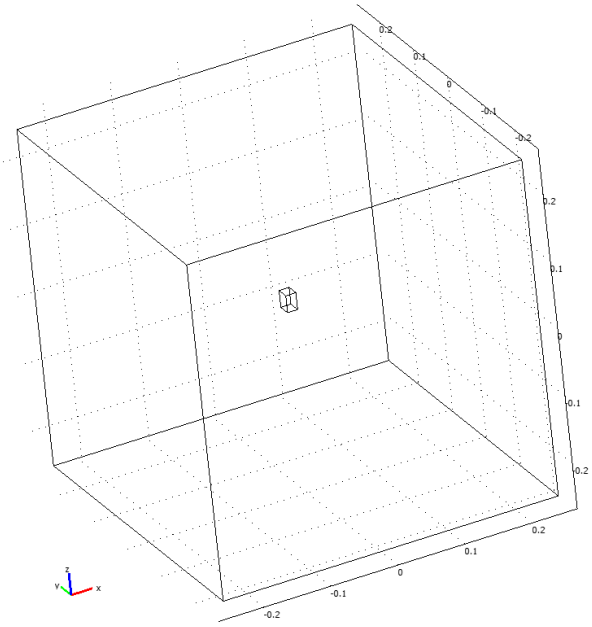

Figure 3.3: Subdomains of the FE model: magnet and air.

mesh consists of tetrahedral elements. Inside the magnet the maximum element size was chosen to be 4 mm. The air region was discretized using a predefined normal mesh size. Figure 3.4 shows the two-dimensional view in the $y-z$ symmetry plane of the FE model before and after the mesh generation. Table 3.1 summarizes the properties of each model.

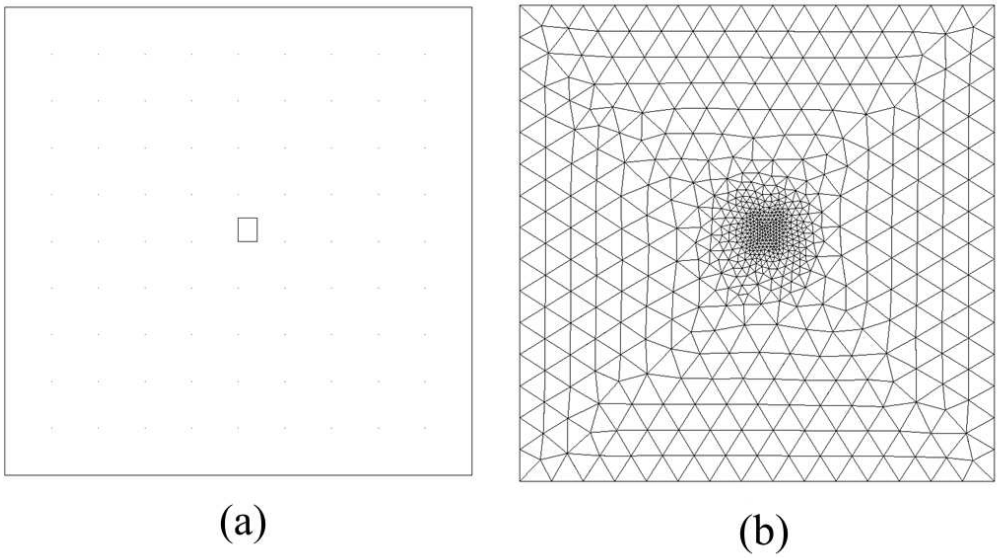

Figure 3.4: Two-dimensional view in the $y-z$ plane of finite elements model (a) before and (b) after the mesh generation.

Table 3.1: Properties of the finite elements models to compute the **B**-field near the rectangular permanent magnet magnetized along the z axis, as shown in Figure 3.2.

Model	1	2
Type of elements	quadratic	cubic
Number of elements	26125	26125
Number of degrees of freedom	207985	617225
Computation time (s)	5.5	46.4

3.2.4 Results and discussion

The z-component of the magnetic flux density B_z was determined analytically and numerically along the z axis of the rectangular magnet (shown in Figure 3.2) using following parameters: $B_r = 1.09$ T, $\mu_r = 1$, $a = 0.015$ m, $b = 0.02$ m, $c = 0.025$ m. We used two analytical methods described in subsection 3.2.1 and 3.2.2 and denoted them as the analytical method 1 and 2 respectively. Two numerical models correspond to the model described in subsection 3.2.3 and differ from each other only in the order of their elements.

Figure 3.5 shows how the obtained magnetic flux density B_z depends on the distance h from the middle point of the magnet surface along the z axis. The ratios between the magnetic flux density B_z obtained using analytical model 1 and the magnetic flux density B_z obtained using the three other methods are plotted in Figure 3.6.

The analytically obtained results are in very good agreement, whereas there is certain discrepancy between the analytical and numerical results. This discrepancy is higher for the numerical model 1, since this model uses second-order elements, which are less accurate than third-order elements. Nevertheless, in the most important region near the magnet ($h < 0.02$ m), where the **B**-field decreases from its highest value by a factor of ten, the discrepancy is sufficiently small (less than 2 %). The relative error for analytical results shown in Figure 3.5 can be calculated using the following expression:

$$\epsilon_1 = \sqrt{\sum_{i=1}^{21}(B_{z,analytic1}(i) - B_{z,analytic2}(i))^2 / \sum_{i=1}^{21}(B_{z,analytic1}(i))^2} = 1.1 \cdot 10^{-5}. \qquad (3.26)$$

The relative error between $B_{z,analytic1}$ and $B_{z,numeric1}$ was calculated similarly and is equal to $\epsilon_2 = 0.0046$. Finally, the relative error between $B_{z,analytic1}$ and $B_{z,numeric2}$ is $\epsilon_3 = 7.8 \cdot 10^{-4}$.

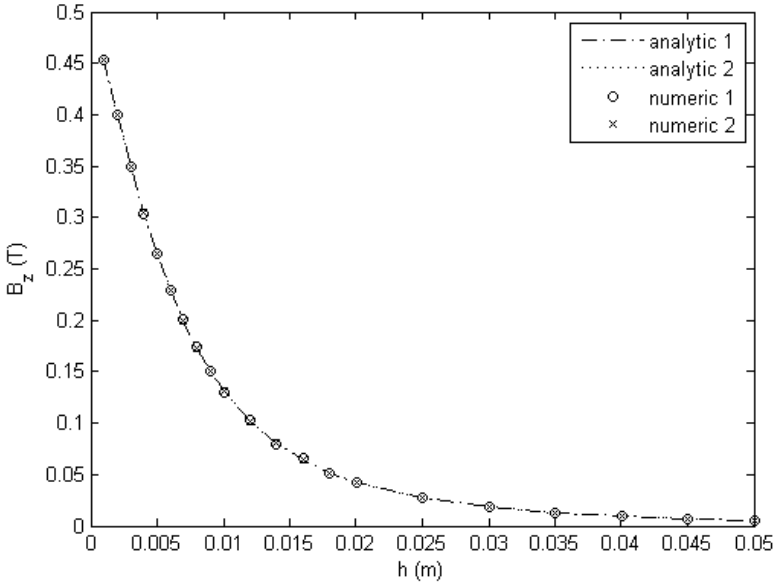

Figure 3.5: Numerically and analytically calculated magnetic flux density B_z: $x = a/2$, $y = b/2$, z varies between c and $c + 0.05$ m (see Figure 3.2).

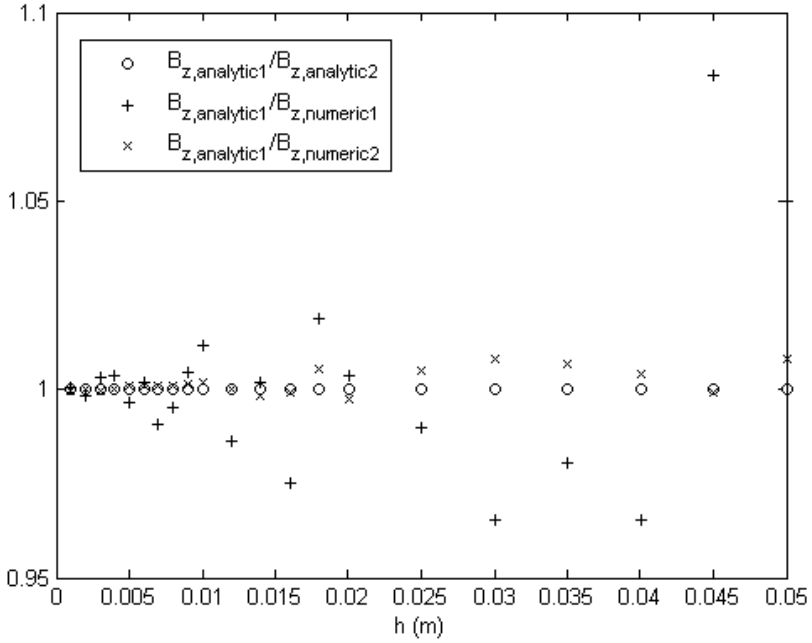

Figure 3.6: Ratios $B_{z,analytic1}/B_{z,analytic2}$, $B_{z,analytic1}/B_{z,numeric1}$, and $B_{z,analytic1}/B_{z,numeric2}$ depending on h.

3.2.5 Mesh study

In this subsection, the magnet system with two permanent magnets, as shown in Figure 1.1(a), is under consideration. Three different mesh sizes are used inside the electrolyte and magnets to obtain the y-component of the magnetic flux density along three axes: along the y axis when $x = z = 0$, along the z axis when $x = y = 0$, and along the x axis when $y = z = 0$. Here, x, y, and z are Cartesian coordinates starting from the

middle point between the magnets. The magnets have fixed dimensions: $x_1 = x_3 = 0.05$ m (along the x and z axis) and $x_2 = 0.025$ m (along the y axis). The air domain dimensions are 0.7 m along the x axis and 0.5 m along the y and z axes. The mesh inside the air domain was generated using the predefined *normal* mesh size [23]. All subdomains were discretized using second order Lagrangian tetrahedral elements. The results were compared with the analytical solution given in subsection 3.2.2. Table 3.2 summarizes the FEM parameters for each model. Here, Δ_e denotes the maximal element size inside the electrolyte and magnets. Figure 3.7 shows the magnetic flux density profiles $B_y(0, y, 0)$ and $B_y(x, 0, 0)$ obtained analytically and numerically. The $B_y(0, 0, z)$ profile is similar to the $B_y(x, 0, 0)$ profile and therefore is not shown. The relative error between the analytically and numerically obtained magnetic flux density B_y has been calculated for each curve as follows:

$$\epsilon_B = \sqrt{\sum_{i=1}^{21}(B_{y1i} - B_{y2i})^2 / \sum_{i=1}^{21}(B_{y1i})^2}. \tag{3.27}$$

Here, B_{y1i} and B_{y2i} denote the value of the magnetic flux density B_y at the ith point, obtained analytically and numerically respectively. Maximal relative error for each model is given in Table 3.2. The relative error decreases by decreasing the element size inside the magnets and electrolyte. However it is slightly higher for $\Delta_e = 4$ mm than for $\Delta_e = 5$ mm, but still sufficiently small. The reason for this behaviour is that we used the free unstructured mesh and second order elements. This combination causes the numerical error which cannot be eluded by decreasing the element size Δ_e less than 5 mm. For the rest of this work mesh with the maximum element size $\Delta_e = 5$ mm was used inside the electrolyte and the magnets, unless otherwise stated. It is optimal both in terms of accuracy and computational cost.

Table 3.2: FEM parameters for each model by the mesh study. DOF stands for degrees of freedom.

Model	1	2	3
Δ_e (mm)	5	4	6
Number of elements	314460	554926	200017
Number of DOF	2416897	4261003	1539096
CPU time (s)	80	139	51
$\epsilon_{B,max}$	0.0038	0.0042	0.0041

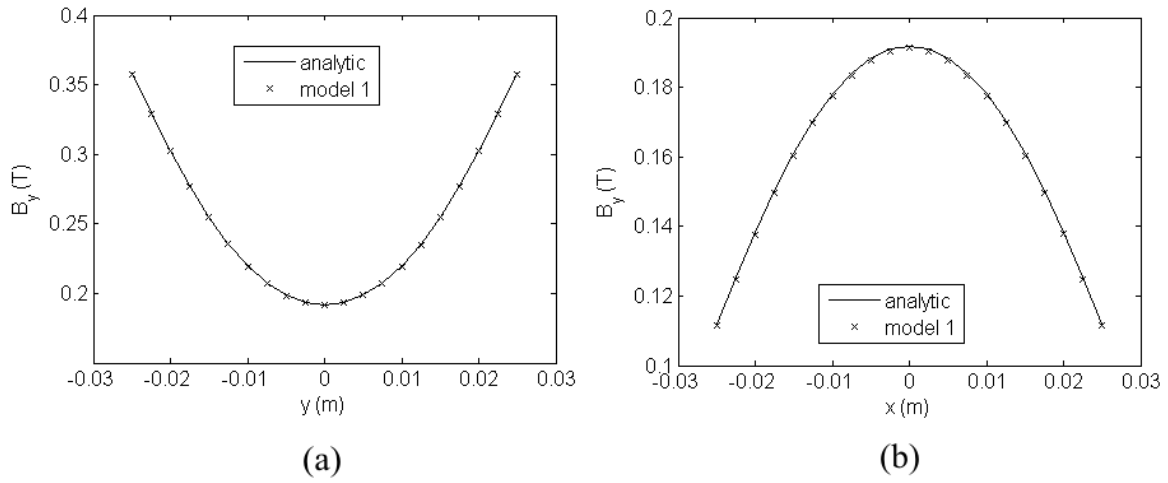

Figure 3.7: Magnetic flux density profiles: (a) $B_y(0, y, 0)$ and (b) $B_y(x, 0, 0)$.

3.3 Validation of the numerical model concerning the drag force

3.3.1 Description of the experiment

Experiments using an aluminum bar were performed to validate the numerical model. These experiments followed the experiments described in [31]. The new experiments differ in that the velocity range was extended to 0.2 m/s by using a new linear drive. The bar was moved with a constant velocity through the magnet system containing two permanent magnet blocks and an iron yoke. Each permanent magnet block was composed of small permanent magnet bars with dimensions 20 mm × 20 mm × 100 mm. The permanent magnet material was again Nd-Fe-B, but with slightly different properties compared to the permanent magnet material described in Chapter 1.

The properties of the magnets are given in the next subsection. The overall dimensions of the dry calibration experiment in the $y - z$ plane are shown in millimeters in Figure 3.8. The overall dimensions of the magnet blocks and iron yoke along the x axis are 140 mm and 160 mm, respectively.

3.3.2 Description of the numerical model

The new numerical model was developed using COMSOL Multiphysics and is governed by partial differential equations (2.16)-(2.17) as well as by boundary conditions (2.20)-(2.23). The model includes seven subdomains: one for the bar, two for the mag-

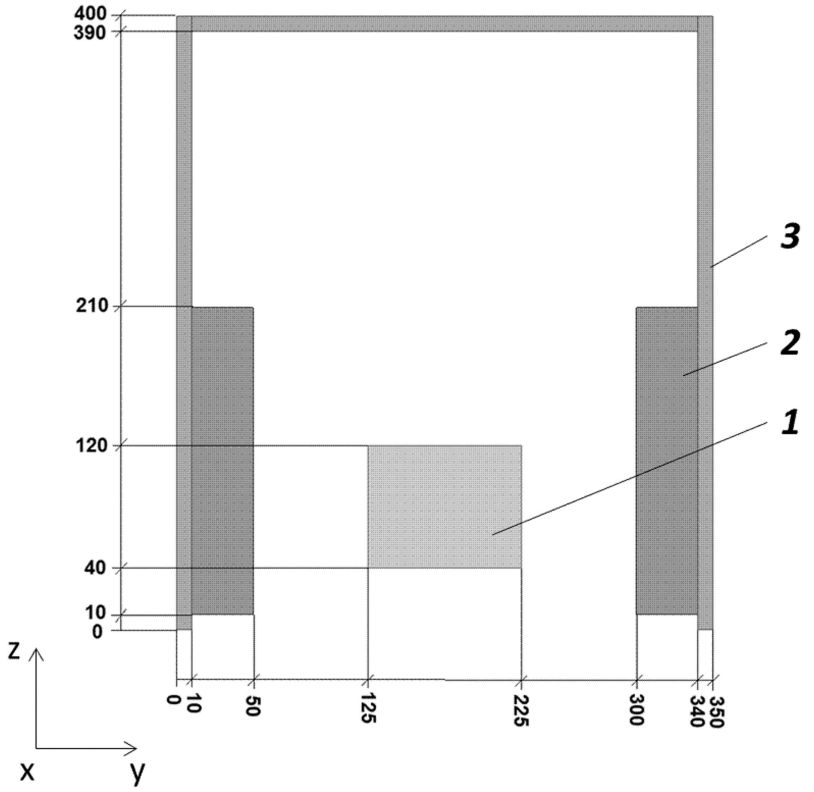

Figure 3.8: Dry calibration experiment: 1 - aluminum bar, 2 - permanent magnet, 3 - iron yoke.

nets, three for the iron yoke, and one for the air (see Figure 3.9). The air subdomain has the dimensions 3 m, 1.75 m and 2 m along the x, y and z axes respectively. A second-order tetrahedral mesh was used to discretize the model. Figure 3.10 shows the two-dimensional view of the subdomains without the mesh in the air region (a) and with the mesh in the air region (b). Table 3.3 summarizes the model properties. The following parameters

Table 3.3: Properties of the numerical model for the dry calibration experiment for v = 0.05 m/s.

Number of elements	255416
Number of DOF	1961291
CPU time (s)	1906
Type of elements	quadratic
Δ_e in the bar (m)	0.012
Δ_e in the magnet (m)	0.03
Δ_e in the iron yoke (m)	0.007
Δ_e in the air (m)	extremely coarse (predefined)
RAM (GB)	4.1
Number of linear solver iterations	192
Number of nonlinear solver iterations	25

constituted our input data: electrical conductivity of the bar $\sigma = 22 \cdot 10^6$ S/m, PM re-

manence $B_r = 1.38$ T, PM coercitivity $H_c = -0.9 \cdot 10^6$ A/m, and a nonlinear BH-curve for *steel 1008* as the material for the iron yoke.

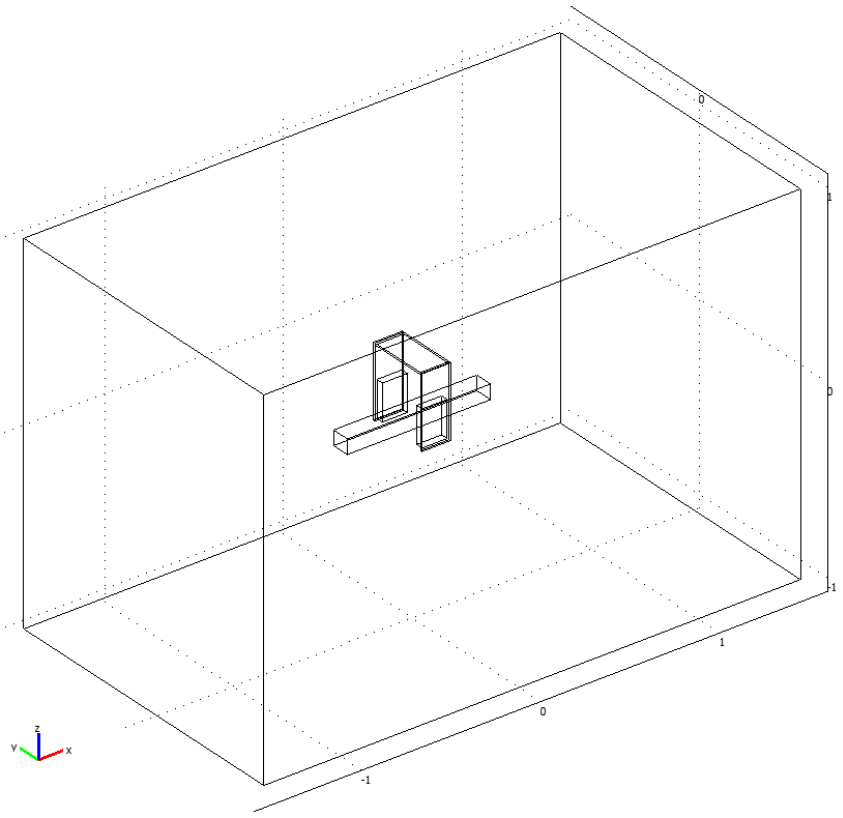

Figure 3.9: Subdomains of the numerical model for the dry calibration experiment.

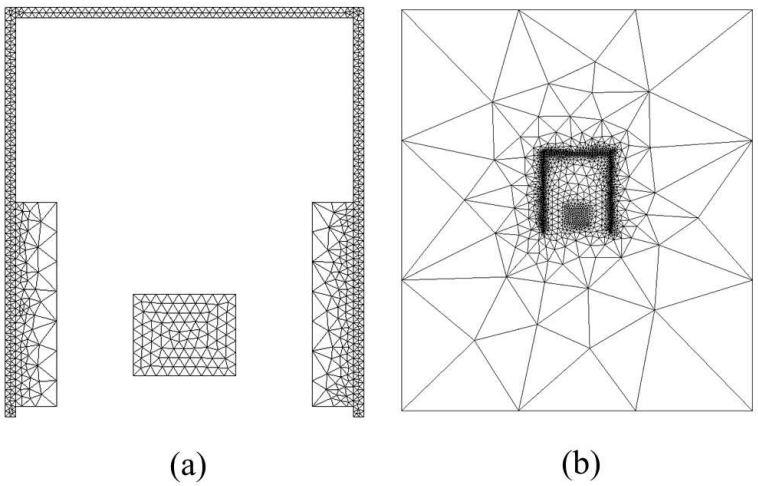

Figure 3.10: Mesh in subdomains of the numerical model for the dry calibration experiment: (a) - without the mesh in the air region; (b) - with the mesh in the air region.

3.3.3 Results and discussion

Figure 3.11 shows the numerically and experimentally obtained dependency of the drag force on the velocity of the bar. The results are in good agreement. The difference between the experimentally and numerically obtained drag force is for the most part less than 5 %. This difference is caused by uncertainties of the physical properties used in the numerical model, namely σ, B_r, and H_c. Furthermore, it must be taken into account that there is some deflection of the velocity caused by the control system of the linear drive. In addition, positioning deviations affected the measurement result.

The relative error between the experimentally and numerically obtained drag force was calculated as follows:

$$\epsilon_F = \sqrt{\sum_{i=1}^{9}(F_{exp}(i) - F_{num}(i))^2 / \sum_{i=1}^{9}(F_{exp}(i))^2} = 0.0242. \tag{3.28}$$

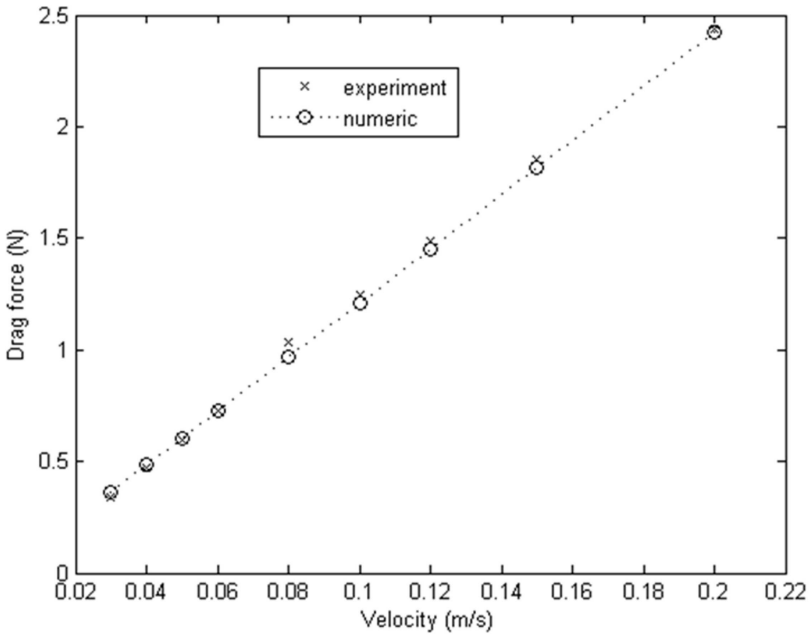

Figure 3.11: Drag force against the bar velocity.

3.4 Validation of the solid bar approximation

In this subsection, results from three numerical models are compared with the experimental results of [10], on a geometric configuration similar to that shown in Figure 1.1(a). Table 3.4 lists the most important parameters of the models as well as the full Lorentz force obtained in each model. In all three models, only one quarter of the full geometry has been considered, taking advantage of symmetry boundary conditions on $z = 0$ and $y = 0$ symmetry planes. The models differ from each other in respect of the fluid motion considered: models 1 and 2 assume a solid body motion, with constant velocity of the electrolyte while model 3 features turbulent flow of the electrolyte, which was modeled using the k-ϵ model in the chemical engineering module of COMSOL Multiphysics [48],[49]. Model 1 differs from models 2 and 3 in the mesh features and length of the electrolyte considered: $L_x = 0.5$ m in model 1 and $L_x = 1.5$ m in models 2 and 3. Figure 3.12 shows the subdomains of the model 1 before and after the mesh generation. Figure 3.13 shows the subdomains of the models 2 and 3 before and after the mesh generation.

Table 3.4: Comparison of numerical models: solid body versus turbulent flow. RANS and MEF stand for Reynolds Averaged Navier-Stokes and Magnetic and Electric Field equations respectively.

Model	1	2	3
Type of motion	solid body	solid body	turbulent flow
Total number of elements	255326	2227992	2227992
Total number of DOF	1997880	17265894	17265894
CPU time (s)	80	9173	6236 (RANS)+11707(MEF)
Full F_L (N)	$2.523 \cdot 10^{-5}$	$2.524 \cdot 10^{-5}$	$2.503 \cdot 10^{-5}$

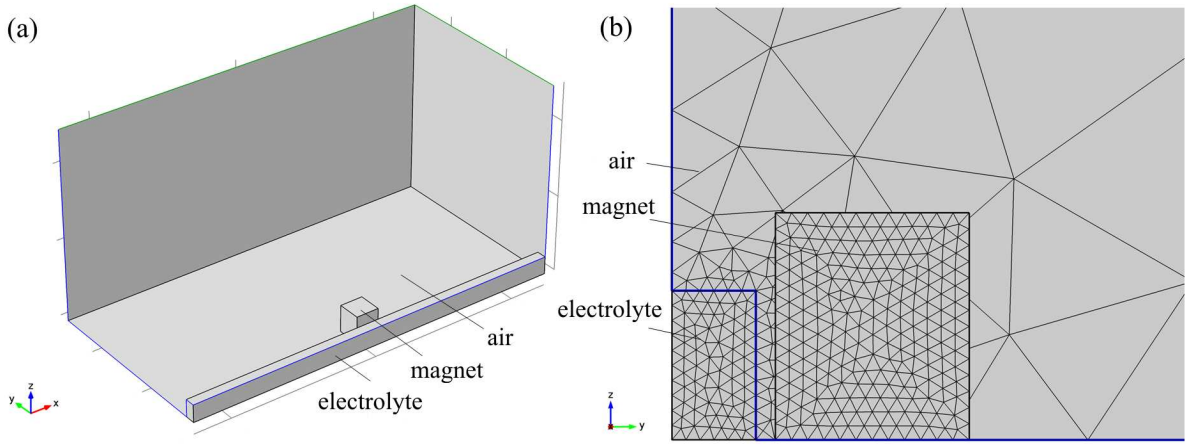

Figure 3.12: Subdomains of the model 1 before and after the mesh generation.

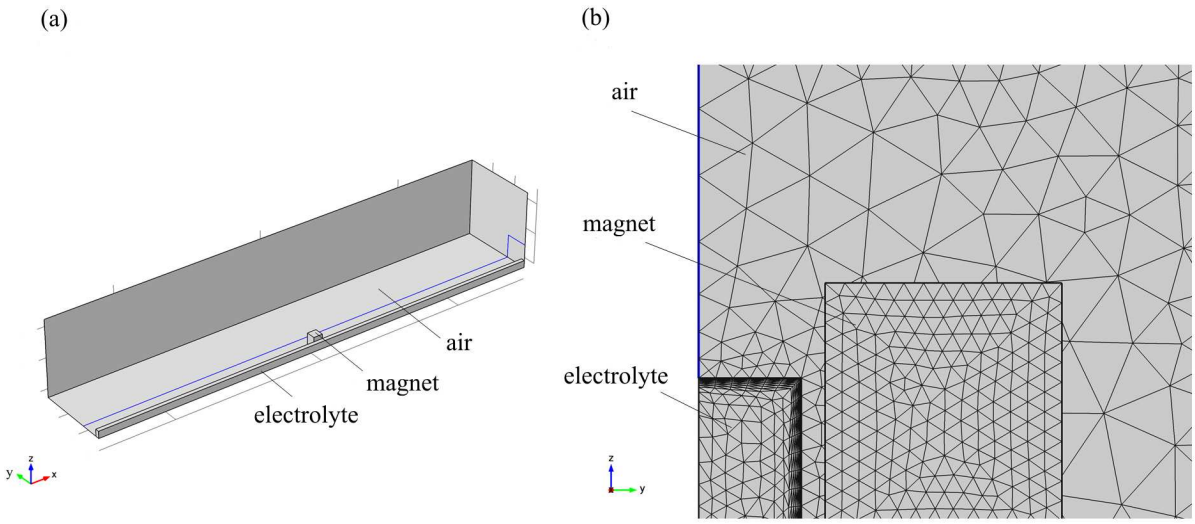

Figure 3.13: Subdomains of the models 2 and 3 before and after the mesh generation.

The experimental parameters in [10] differ slightly from the data given in Chapter 1. The magnet system contained two magnets. The dimensions of each magnet were: $x_1 = x_2 = 0.03$ m and $x_3 = 0.07$ m. The distance between the magnets was $D = 0.032$ m. The channel cross-section dimensions were $w = 0.03$ m (along the y axis) and $h = 0.05$ m (along the z axis). The channel wall thickness was equal to 0.002 m, so that the active cross-section dimension of electrolyte was $S = 0.026 \times 0.046$ m^2. The velocity of electrolyte was fixed to $\mathrm{v}_x = 4$ m/s. The magnetic properties of the magnets ($B_r = 1.34$ T and $\mu_r = 1$) were adjusted to fit the experimentally measured magnetic field component B_y in the middle point between the magnets which was equal to 0.41 T.

It should be mentioned that in case of turbulent flow of the electrolyte the logarithmic wall function was used as the boundary condition on the walls. This function requires a finer mesh size near the walls (see Figure 3.13(b)). A boundary layer mesh with eight layers was used to satisfy this requirement. Moreover, full channel length ($L_x = 1.5$ m) was considered in the case of turbulent flow to mimic the developed turbulent flow in the channel. All these factors caused a substantial increase in the number of elements in model 3. To compare the numerical results, the same mesh was used in model 2 for solid body motion. It is evident from Table 3.4 that the obtained Lorentz drag force is almost the same for all numerical models. Since the CPU time of model 1 is much less than of models 2 and 3, similar mesh settings were used for the rest of the work.

Figure 3.14 shows one-dimensional plots of magnetic flux density B_y, velocity v_x,

eddy current density J_z, and Lorentz force density f_{Lx} along the y axis at $x = 0$ and $z = 0$ obtained using models 2 and 3. The results from model 1 are almost the same as those from model 2 and therefore not shown here. It can be seen from Figure 3.14 that the different velocity profile in the channel causes different eddy current distribution and Lorentz force distribution in electrolyte. Roughly, the higher the velocity, the higher the eddy current density and the higher the Lorentz force density. Near the wall the solid body velocity approximation is higher than the velocity of the turbulent flow (see Figure 3.14(b)). The eddy current density is also higher in this region for the solid body than for the turbulent flow (see Figure 3.14(c)). Finally, the Lorentz force density is also higher in this region for the solid body (see Figure 3.14(d)). Note that the Lorentz force density in the electrolyte is to a considerable degree negative, since it acts opposite to the velocity of the electrolyte (see Figure 1.1(a)).

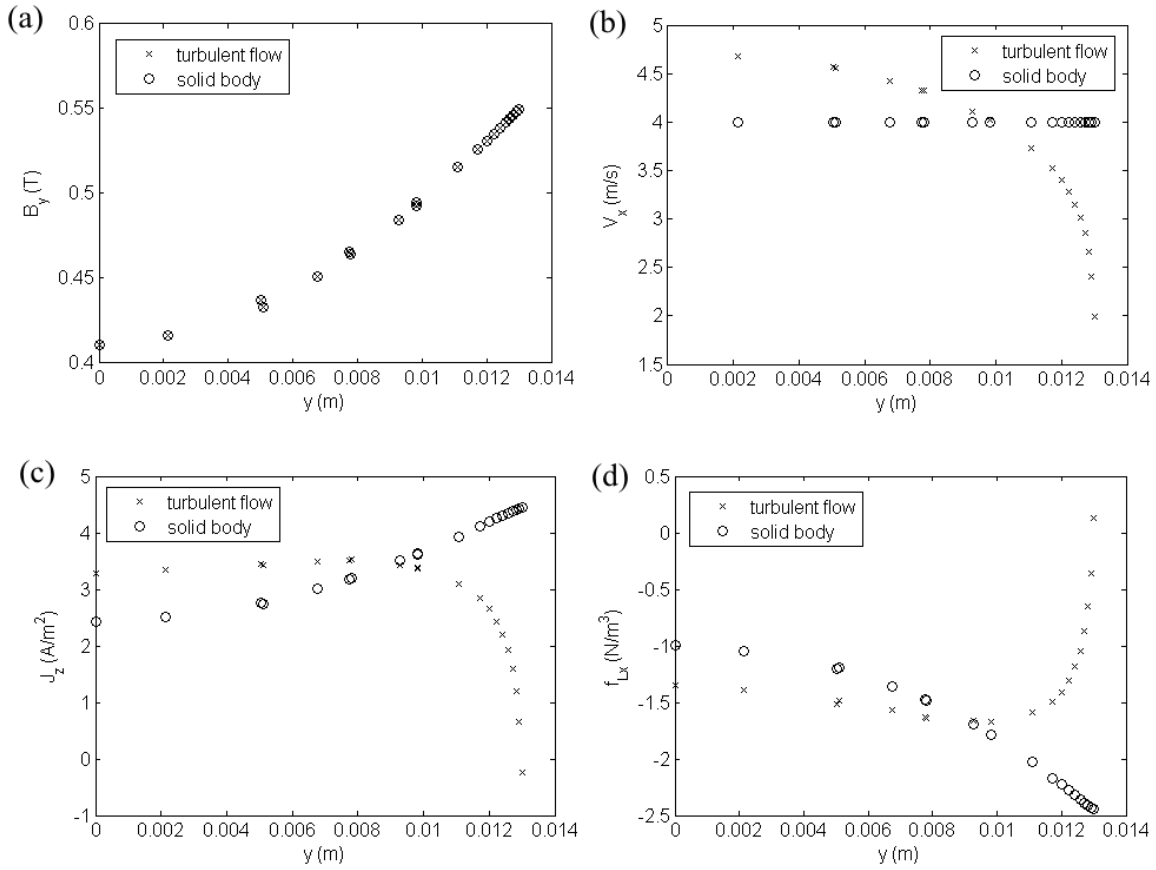

Figure 3.14: One-dimensional plots of magnetic flux density B_y, velocity v_x, eddy current density J_z, and Lorentz force density f_{Lx} along the y axis at $x = 0$ and $z = 0$ obtained using models 2 and 3.

Figure 3.15 displays the experimentally and numerically obtained Lorentz drag force against the velocity of the electrolyte. The results are in good agreement. Because of the

considerable lower CPU time and insignificant difference in the results, numerical models with features similar to those used in model 1 were used for subsequent investigation.

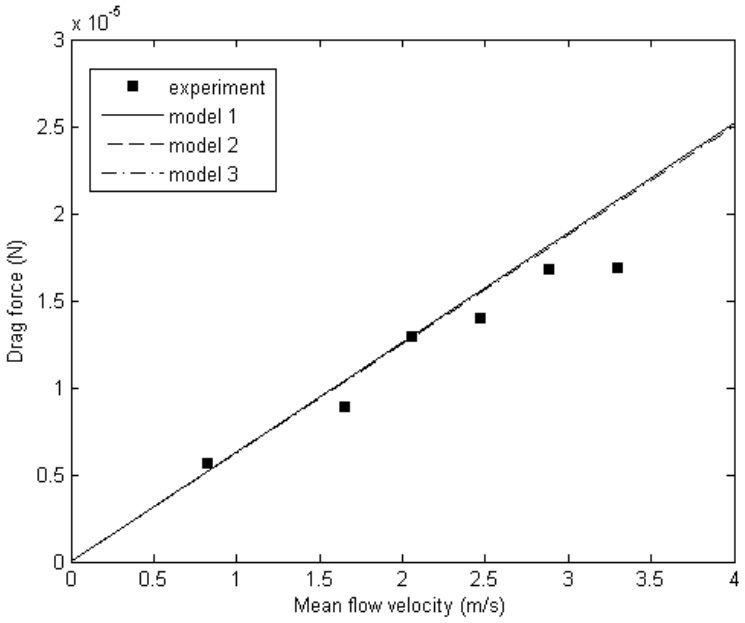

Figure 3.15: Experimentally and numerically obtained Lorentz drag force against the velocity of electrolyte.

3.5 Validation of the low Rm approximation

This section considers two numerical formulations of the problem stated in Chapter 1. The magnet system considered is that with two permanent magnets. The dimensions of the magnets are $x_1 = 0.04$ m, $x_2 = 0.02$ m, and $x_3 = 0.04$ m along the x, y, and z axes respectively.

The first formulation is given in section 2.3 of this dissertation. The second formulation will be given in this section. It is assumed that because of small magnetic Reynolds number (see section 2.5), equation (2.16) can be simplified as follows:

$$\nabla \times \Big(\frac{1}{\mu}(\nabla \times \mathbf{A}) - \mathbf{M}\Big) = 0 \tag{3.29}$$

In equation (3.29) the eddy current term is neglected. Solving this equation in all problem subdomains including the air region gives the primary magnetic field due to the magnetization of the magnets and neglects the secondary magnetic field due to the eddy

currents within the electrolyte. We compared the magnetic flux density profile $B_y(0, y, 0)$ for these two formulations using formula (3.27) and the relative error is sufficiently small ($\epsilon_B = 1.61 \cdot 10^{-6}$), which proves that the secondary magnetic field can be neglected.

Equation (2.17) was solved within electrolyte subdomain after solving equation (3.29) by a given **A** field. The boundary conditions were the same for both formulations. The difference between obtained Lorentz forces was also negligibly small ($F_{L1} = 1.321493 \cdot 10^{-5}$ N and $F_{L2} = 1.321467 \cdot 10^{-5}$ N).

Chapter 4

Magnet system optimization

The optimization of the magnet system for LFV of electrolytes took place in two steps. First, selection of the magnet system components; second, optimization of the magnetization directions and magnet dimensions.

The primary question was whether to use permanent magnets or solenoidal coils to generate the magnetic field. After preliminary calculations and a literature survey, PMs were chosen, since the MS weight is restricted, and only PMs can generate a relatively high magnetic field with an operating weight of less than 1 kg [15].

The next question to be answered was whether to use an iron yoke in the LFV for electrolytes or not. To answer this question, two magnet systems were simulated: one with an iron yoke and the other built exactly like it but without an iron yoke. The results showed that the magnet system without an iron yoke is much more efficient, in fact approximately twice as efficient, efficiency being defined as the ratio between the drag force and the MS weight [32], [33], [34].

Another important task was finding the optimal dimensions and arrangement of the permanent magnet system. To do so, the iterative optimization technique *sequential quadratic programming* (SQP) was used which is contained in the MATLAB optimization toolbox [35], [36], [37].

Besides the magnet system with two PMs, other magnet systems, which are also called Halbach arrays [12], [13], [39], were investigated and compared. A Halbach array is a set of permanent magnets which provides one-sided magnetic flux [43]. Halbach arrays are used in different areas of industry and high-tech applications: in magnetic bearings, brushless AC motors, wiggler magnets of particle accelerators, nuclear magnetic

resonance (NMR) devices, and magnetically levitating systems. In [44] and [45] directions of magnetization within the magnet sets were optimized to obtain maximal attractive force and magnetic field on the surface of the set. Sequential linear programming and the adjoint method were used as optimization methods. Halbach arrays appeared to provide the highest attractive force and magnetic flux on the surface for a given geometry. Thus, it is reasonable to apply a Halbach array pattern in the development of the magnet system for Lorentz Force Velocimetry.

4.1 Optimization procedure

With a tool enabling us to numerically calculate the force F_L exerted on the magnet system, the next task was to optimize the magnet arrangement in order to maximize F_L. It is necessary to maximize F_L, because our measurement system cannot measure forces lower than 10 μN. In other words, by achieving the highest possible Lorentz force, we would increase the resolution of the measurement system for lower flow velocities and lower electric conductivities.

The magnet system is made of two Halbach arrays placed opposite each other on either side of the channel. Each array consists of N rectangular magnets, with magnetization pointing alternatively in the x and y directions (see Figure 4.25). The two arrays are designed so that opposite pairs of magnets are of the same dimension. All magnets have the same size x_2 and x_3 in the y and z direction but magnets with streamwise and upstreamwise spins may have different dimensions x_4 from magnets with crosswise spins (see Figure 4.24).

The optimization is subject to constraints regarding dimensions and weight of the magnet system. For the application at stake, the magnet density is $\rho = 7500$ kg/m^3 and the maximum allowed weight is m. Mathematically, the finding of the magnet system that maximizes the Lorentz force is formulated as the optimization problem of maximizing F_L,

subject to the following constraints:

$$G(x_1, x_2, x_3, x_4) \leq m,$$

$$x_1^{min} \leq x_1 \leq x_1^{max}, \tag{4.1}$$

$$x_2^{min} \leq x_2 \leq x_2^{max}, \tag{4.2}$$

$$x_3^{min} \leq x_3 \leq x_3^{max}, \tag{4.3}$$

$$\text{and for} \quad N > 1$$

$$x_4^{min} \leq x_4 \leq x_4^{max}, \tag{4.4}$$

where the weight of the magnet system

$$G(x_1, x_2, x_3, x_4) = 2\rho E((N+1)/2)x_1 x_2 x_3 + 2\rho E((N-1)/2)x_4 x_2 x_3 \tag{4.5}$$

must remain below its specified maximum value m, and where $E(N)$ is the integer part of N. Since $F_L(x_1, x_2, x_3, x_4)$ is not known analytically, it must be calculated on a discrete 3- or 4-dimensional grid. The value of F_L at each point is obtained by the numerical resolution of system (2.16)-(2.17) with the boundary conditions already established, following the method outlined in section 3.1.4.

To obtaining a precise estimate of optimal design variable by direct application of a standard optimization method onto a single grid, a fine grid resolution would be necessary. Unfortunately, since each point requires the numerical resolution of a PDE, the computational cost becomes prohibitive even at moderate resolutions. It was therefore decided to adopt an alternative approach which is much less computationally intensive and incurs practically no penalty for the final precision attained. Taking advantage of the smooth variations of F_L against each of the design variables, we first calculated F_L on a coarse grid, with n_v values per design variable. These "exact" values were fitted with a multivariate polynomial of order q, from which it is straightforward to extract a maximum. The coarse grid was then refined with a new grid, again with n_v values per design variable but, this time, restricted to a volume of 50 % of the spanned interval for each variable, and centered on the location of the coarse maximum. The procedure was then iterated until the desired precision was reached, as summarized in Figure 4.13.

This was our procedure: At step zero of the optimization routine for a given m, the initial values of design variables $x_i = (x_i^{max} + x_i^{min})/2$ as well as their lower and upper bounds (x_i^{min} and x_i^{max}) with a coarse step size $\Delta x_i = (x_i^{max} - x_i^{min})/2$ are defined roughly (see Table 4.9): i.e., for each variable three values are defined. In the first step, the drag force is computed at these points using the numerical model described in Chapter 3. At the second step, the drag force is fitted using polynomial of order q. At the third step, the optimization problem is solved. If the required precision has been reached, then the optimization routine is stopped; otherwise the design space around the optimizer is refined ($\Delta x_i^{new} = \Delta x_i/2$) and the procedure returns to step 1 (see Figure 4.13).

To solve the optimization problem (4.1-4.5) the *fmincon* function was used from the optimization toolbox in MATLAB [37], [35]. This function finds the minimum of constrained nonlinear multivariate function F_L. The *fmincon* function attempts to find a constrained minimum of a scalar function of several variables starting at an initial estimate. This is generally referred to as *constrained nonlinear optimization* or *nonlinear programming*. The method of *fmincon* is gradient-based, designed to work on problems where the objective function and constraint functions are both continuous and have continuous first derivatives. The active-set algorithm and sequential quadratic programming method were applied in using the *fmincon* function. In this method, the function solves a quadratic programming (QP) subproblem at each iteration. An estimate of the Hessian of the Lagrangian is updated at each iteration using the Broyden-Fletcher-Goldfarb-Shanno (BFGS) formula [38]. A line search is performed using a merit function similar to that proposed in [38]. The QP subproblem is solved using an active set strategy similar to that described in [36].

The *fmincon* function is focused on the solution of the Karush-Kuhn-Tucker (KKT) equations, which are necessary conditions for optimality for a constrained optimization problem. For a smooth constrained optimization problem

$$\min_{\mathbf{x}} f(\mathbf{x}) \qquad \text{subject to} \qquad \mathbf{g}(\mathbf{x}) \leq 0, \tag{4.6}$$

where $\mathbf{g}$ is the vector representing all inequality constraints and $\mathbf{x}$ is the vector of design

variables (bounds and nonlinear constraints), the KKT conditions are:

$$\nabla f(\mathbf{x}^*) + \sum_{i=1}^{n} \lambda_i \nabla g_i(\mathbf{x}^*) = 0, \tag{4.7}$$

$$\lambda_i \cdot g_i(\mathbf{x}^*) = 0, \tag{4.8}$$

$$\lambda_i \geq 0, \qquad i = 1, ..., n. \tag{4.9}$$

The equation (4.7) describes a canceling of the gradients between the objective function and the active constraints at the solution point $\mathbf{x}^*$. For the gradients to be canceled, Lagrange multipliers λ_i are necessary to balance the deviations in magnitude of the objective function and constraint gradients. Because only active constraints are included in this canceling operation, constraints that are not active must not be included in this operation and so are given Lagrange multipliers equal to zero. This is stated implicitly in the equations (4.8) and (4.9).

The optimality measures associated with (4.7) and (4.8) are respectively

$$\|\nabla f(\mathbf{x}) + \sum_{i=1}^{n} \lambda_i \nabla g_i(\mathbf{x})\|, \tag{4.10}$$

$$\|\lambda_i \cdot g_i(\mathbf{x})\|. \tag{4.11}$$

The norm in (4.11) means infinity norm (maximum) of the vector $\lambda_i \cdot g_i(\mathbf{x})$. The combined optimality measure is the maximum of the values calculated in (4.10) and (4.11). If this combined optimality measure is less than termination tolerance on the function value ($\epsilon_{TolFun} = 10^{-9}$), solver iterations end.

To illustrate the design space, the objective function, the nonlinear constraint and the optimal point, it is convenient to consider the optimization problem with two design variables. To do so, the magnet system with two magnets shown in Figure 4.2 can be considered as follows. The design variables are linear dimensions of the magnets: x_1 is the length (along the x axis), x_2 is the width (along the y axis) and x_3 is the height (along the z axis). The input data are given in Chapter 1. To deal with two design variables, we fixed $x_2 = 0.0175$ m. Figure 4.1 shows the level lines of the objective function (negative Lorentz force) which is minimized over design space 0.02 m $\leq x_1 \leq$0.03 m and 0.04 m$\leq x_3 \leq$0.05 m subject to the inequality constraint $G = 2 \cdot 7500 \cdot 0.0175 x_1 x_3 - 0.32 \leq 0$, i.e. $m = 0.32$ kg. The objective function was fitted with a polynomial of second order using least square

fit and had the following form: $F(x_1, x_3) = -(c_1 x_1^2 + c_2 x_1 x_3 + c_3 x_1 + c_4 x_3^2 + c_5 x_3 + c_6)$, where $c_1 = -6.89353e-3$, $c_2 = 6.72299e-3$, $c_3 = 3.84385e-4$, $c_4 = -4.57709e-3$, $c_5 = 4.20421e-4$, $c_6 = -1.30944e-5$ are coefficients of the polynomial. The solution of this problem was found using the *fmincon* function at point $x_1^{opt} = 0.027$ m, $x_3^{opt} = 0.0451$ m in which $F = -1.0106e-5$ N (point P in Figure 4.1). The Lagrange multiplier was equal to $\lambda = 2.6628e-5$ in this point. In other words, the solution of this optimization problem is the point where KKT conditions are satisfied, i.e. gradients of G and F are canceled. It is important to note that F denotes the Lorentz drag force F_L (we dropped the index $_L$ for convenience). The same notation is used for the rest of this work.

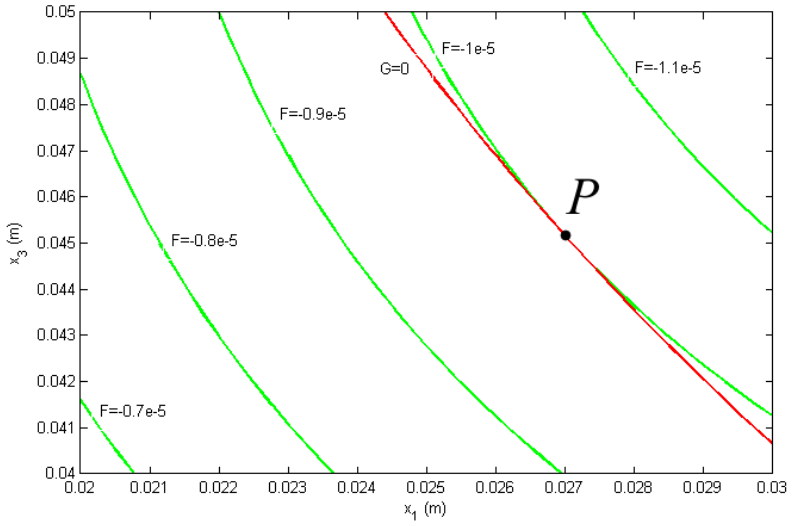

Figure 4.1: Example of graphical optimization for two design variables. Green lines represent the level lines of the objective function F and the red line represents inequality constraint G.

4.2 Magnet system containing two permanent magnets

Turning first to the magnet system containing two permanent magnets (see Figure 4.2): two identical magnets were located symmetrically with respect to the channel and to each other. Variables x_1, x_2, and x_3 denote the length, width, and height of the magnets respectively. The arrows on the magnets denote the direction of magnetization. This direction was chosen because it corresponds to the highest drag force found in preliminary calculations.

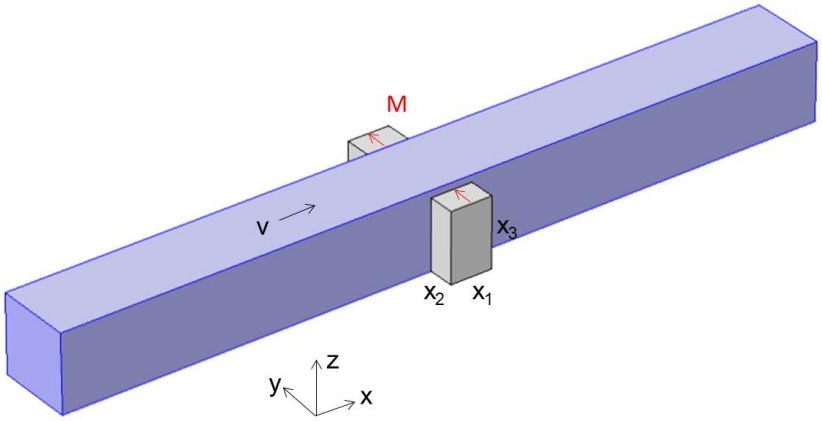

Figure 4.2: Magnet system containing two permanent magnets.

4.2.1 Description of the numerical model

The numerical model was developed using COMSOL Multiphysics. The input parameters are given in Chapter 1. The model is governed by the system of equations (2.16)-(2.17) as well as by boundary conditions (2.20)-(2.23). The model includes four subdomains: one for the electrolyte, two for the magnets, and one for the air (see Figure 4.3). We used the optimized dimensions for the magnets x_1, x_2, and x_3 in this model, which are 0.027 m, 0.0175 m, and 0.0452 m respectively. The process of finding these dimensions is described in the next subsections. The air subdomain had the dimensions 0.7 m, 0.5 m, and 0.5 m along the x, y, and z axes respectively. A second-order tetrahedral mesh was used to discretize the model. Figure 4.4 shows the two-dimensional view of the subdomains without the mesh in the air subdomain (a) and with the mesh in the air subdomain (b). Figure 4.5 shows the magnetic flux density vector plot in the $z = 0$ symmetry plane in the electrolyte. Figure 4.6 shows the current density vector plot in the $y = 0$ symmetry plane in the electrolyte. Table 4.1 summarizes the properties of the numerical model.

4.2.2 Parametric study

Along with the design variables x_1, x_2, and x_3 we introduced the design variable x_g that corresponds to the gap between the magnets and the electrolyte. Parametric analysis was performed to better understand the four-variable issue. Figure 4.7 shows the drag force F plotted against the design variables x_i and x_g divided (or normalized)

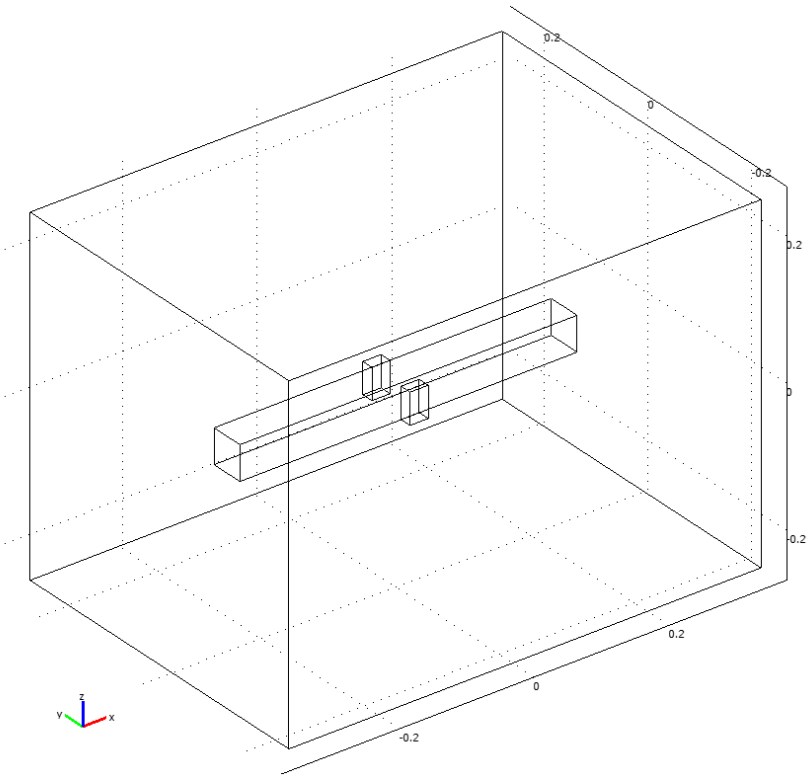

Figure 4.3: Subdomains of the numerical model for the MS with 2 PMs.

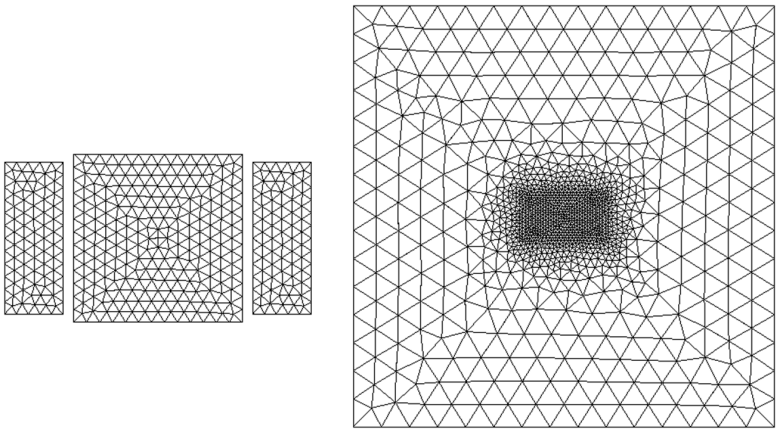

(a) (b)

Figure 4.4: Two-dimensional view of the subdomains in the $x = 0$ symmetry plane: (a) without the mesh in the air subdomain and (b) with the mesh in the air subdomain.

by the characteristic length of the channel cross-section L. Each curve corresponds to the variation of a single design variable while the other three variables remain constant. Drag force grows nonlinearly with increasing x_1, x_2, and x_3 and declines nonlinearly with increasing x_g. All curves in Figure 4.7 tend to saturate after a certain x_i/L. This behavior can be better recognized on considering Figure 4.8, which plots the ratio between the drag force and MS weight against the nondimensional design variables x_i/L and x_g/L. All curves in Figure 4.8, except F/m depending on x_g, have one peak, after which they

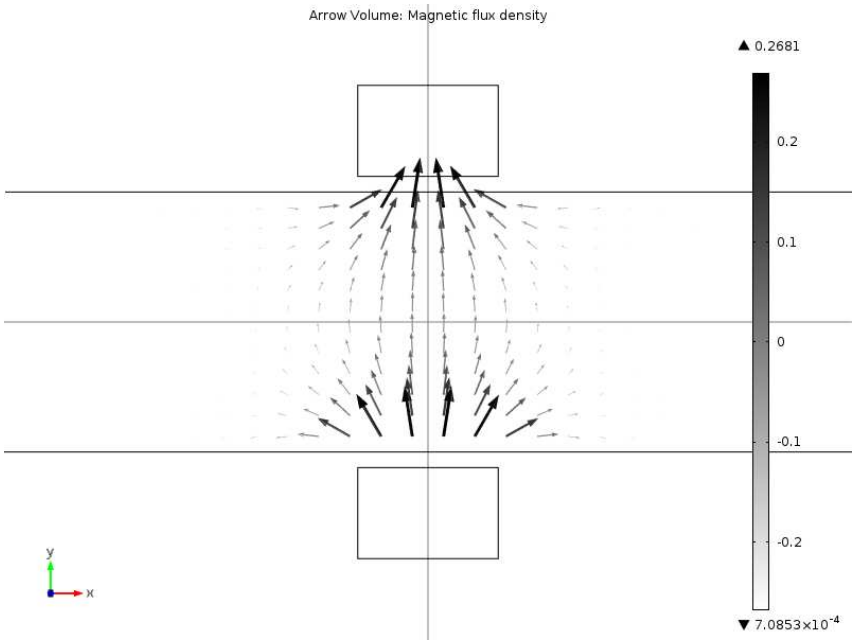

Figure 4.5: Magnetic flux density **B** (T) vector plot in the $z = 0$ symmetry plane in the electrolyte.

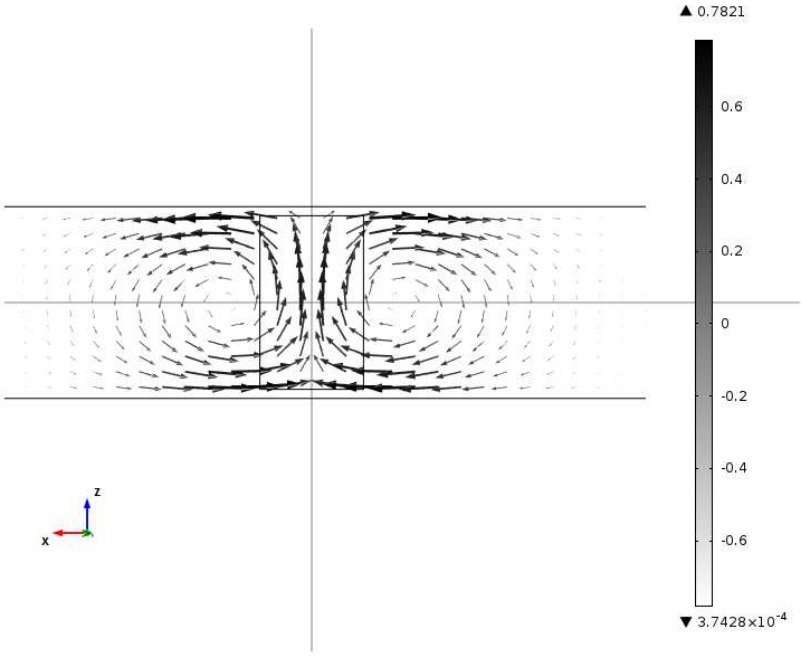

Figure 4.6: Current density **J** (A/m^2) vector plot in the $y = 0$ symmetry plane in the electrolyte.

decline. Figures 4.7 and 4.8 reveal firstly that to increase the drag force the design variable x_g must be minimized and secondly that optimal values of the variables x_1, x_2, and x_3 must be found that satisfy the problem constraints and provide the highest drag force at a given MS weight. The gap between the electrolyte and the magnets was fixed at $x_g = 3$ mm. This gap size comprises the wall thickness of the channel (2 mm) and the air gap (1 mm).

Table 4.1: Properties of the numerical model for the MS with two PMs.

Number of elements	524287
Number of DOF	4026082
CPU time (s)	160
Type of elements	quadratic
Δ_e in the bar (m)	0.004
Δ_e in the magnet (m)	0.004
Δ_e in the air (m)	normal (predefined)
RAM (GB)	7.6
Number of linear solver iterations	7

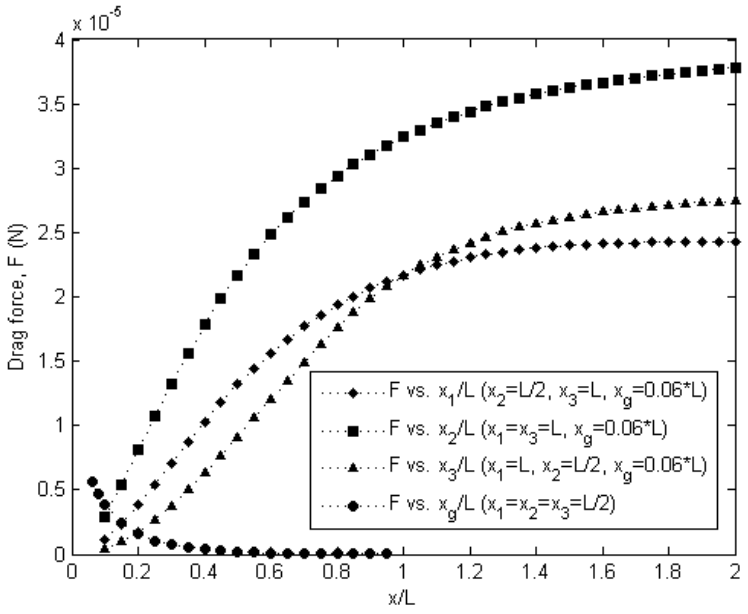

Figure 4.7: Drag force F in relation to x_1/L, x_2/L, x_3/L, and x_g/L, where $L = 0.05$ m is the characteristic length.

To compare different magnet systems it is reasonable to use a nondimensional parameter, such as the calibration coefficient K, which is defined as follows:

$$K = \frac{F}{\sigma \cdot B^2 \cdot L \cdot \dot{V}}. \tag{4.12}$$

Here, F is the drag force, B the characteristic magnetic field, e.g. in the middle point between the magnets, and $\dot{V} = L^2 \cdot \mathrm{v}$ the specific volumetric flow rate in the channel. Figure 4.9 displays the calibration coefficient K against x_i/L and x_g/L. It is notable that K decreases nonlinearly with increasing x_i/L. Furthermore, saturation appears after certain x_i. It is important to mention that for the magnet system used in the dry

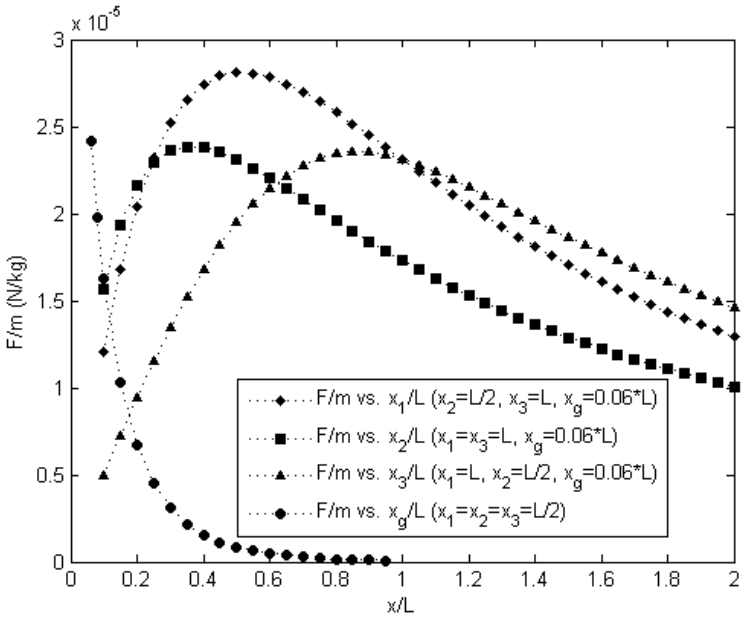

Figure 4.8: Ratio between the drag force and MS weight F/m in relation to x_1/L, x_2/L, x_3/L, and x_g/L, where $L = 0.05$ m is the characteristic length.

calibration experiment (see section 3.3 and Figure 3.8) the calibration coefficient is equal to $K = 0.069$. For the magnet system without an iron yoke this coefficient can reach values approximately 6 times higher (see Figure 4.9). Here, only values of K corresponding to a drag force higher than 10 μN were taken into account. As must be clear from the previous discussion, it is necessary to maximize the calibration coefficient.

4.2.3 Optimization algorithm for three design variables using the surface fitting tool in MATLAB

In this subsection the optimization algorithm will be described for the case of a magnet system with two permanent magnets and three design variables (see Figure 4.2). From the previous investigation it was found that the design variable x_g must be as small as possible, whereas the variables x_1, x_2, and x_3 must be optimized to obtain the maximal drag force at a given MS weight. The design variable x_g was fixed at 3 mm because of the design conditions. The other design variables are restricted by using lower and upper boundaries to form a so-called design space. The objective function $F = F(x_1, x_2, x_3)$ is the drag (or Lorentz) force. It depends on the design variables and must be maximized at the limited weight of the permanent magnets, so that the nonlinear inequality constraint

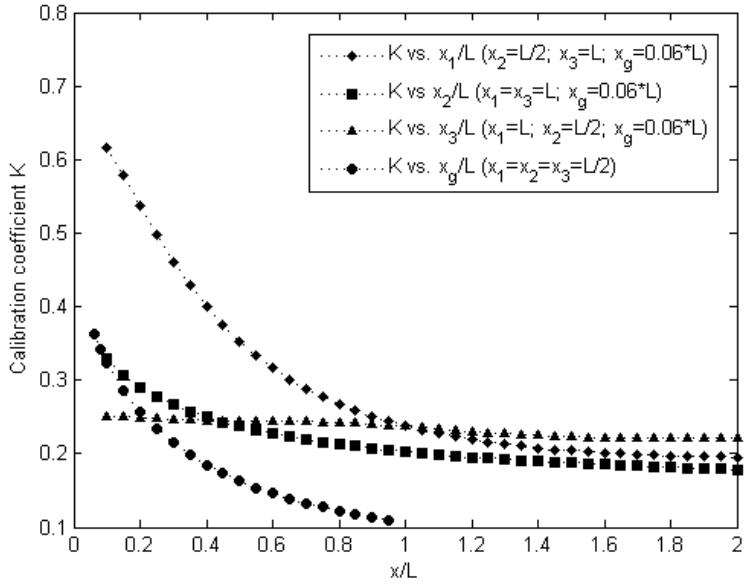

Figure 4.9: Calibration coefficient K in relation to x_1/L, x_2/L, x_3/L, and x_g/L, where $L = 0.05$ m is the characteristic length.

$G(x_1, x_2, x_3) \leq 0$ is fulfilled. In general, the optimization problem can be formulated as follows [35], [40]:

$$\begin{gathered} \textit{Maximize } F(x_i) \textit{ (or Minimize } -F(x_i)) \\ \textit{Subject to } G(x_i) \leq 0, \\ x_i^{min} \leq x_i \leq x_i^{max}, i = 1, 2, 3. \end{gathered} \tag{4.13}$$

The main difficulty in (4.13) is to find an expression for the objective function. Since there are only three design variables, one of them can be kept constant, e.g. x_2. Then the discrete function $F(x_1, x_3)$ can be obtained using the numerical model described in subsection 4.2.1. Afterwards, the polynomial approximation F' of F can be found using the surface fitting tool in MATLAB [37]. Then the optimization problem can be formulated as follows [40], [47]:

$$\begin{gathered} \textit{Minimize } -F'(x_1, x_3) = -(c_{00} + c_{10}x_1 + c_{01}x_3 + c_{20}x_1^2 + c_{11}x_1x_3 + c_{02}x_3^2 \\ + c_{30}x_1^3 + c_{21}x_1^2x_3 + c_{12}x_1x_3^2 + c_{03}x_3^3 + c_{40}x_1^4 + c_{31}x_1^3x_3 + c_{22}x_1^2x_3^2 \\ + c_{13}x_1x_3^3 + c_{04}x_3^4 + c_{50}x_1^5 + c_{41}x_1^4x_3 + c_{32}x_1^3x_3^2 + c_{23}x_1^2x_3^3 + c_{14}x_1x_3^4 + c_{05}x_3^5) \\ \textit{Subject to } 2 \cdot \rho \cdot x_1 \cdot x_2 \cdot x_3 - m \leq 0, \\ x_2 = const, x_i^{min} \leq x_i \leq x_i^{max}, i = 1, 3. \end{gathered} \tag{4.14}$$

Here, c_{ij} are coefficients of the polynomial, $\rho = 7500$ kg/m^3 is the density of the permanent magnets, and m is the magnet system weight. The nonlinear optimization problem with inequality constraints (4.14) is then solved using the function *fmincon* in MATLAB. Thus, for any one x_2, only one maximum of F can be found which satisfies the inequality constraint $G(x_i) \leq 0$ as well as the lower and upper bounds for design variables x_i. Figure 4.10 shows an example of the approximated function $F(x_1, x_3)$ for $x_2 = 17.5$ mm. For this case, the input data are given in Chapter 1. The points in Figure 4.10 correspond to the numerically obtained drag force, whereas the surface corresponds to the polynomial approximation. This approximation is very accurate. The difference between F and F' is less than 1 %.

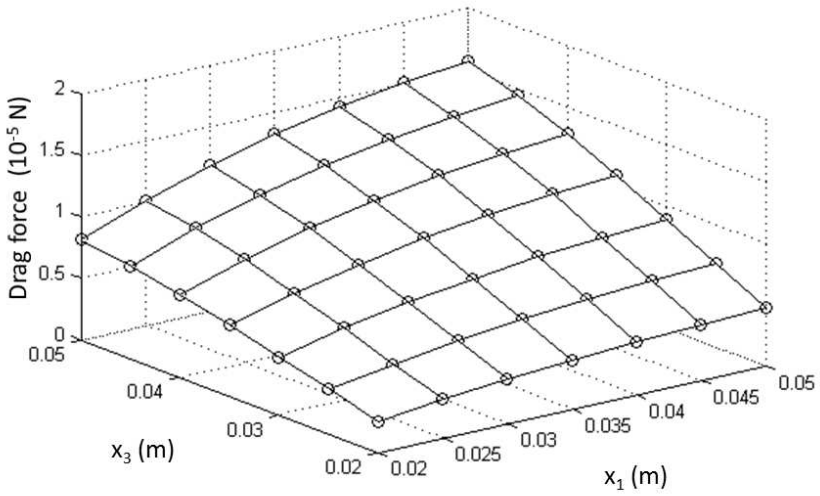

Figure 4.10: Approximated drag force as a function of length x_1 and height x_3 of PM in the case of the magnet system with 2 PMs, $x_2 = 17.5$ mm, $x_g = 3$ mm.

To find the maximal Lorentz force for a given magnet system weight using the optimization toolbox in MATLAB, it is convenient to use a polynomial as an objective function. In this case, the optimization procedure is performed very quickly (less than 2 seconds). For the FEA-evaluation of the objective function, the optimization procedure is much slower, taking several hours. The solution obtained using the polynomial is, moreover, much more accurate, which was proved by comparing these two approaches for finding the optimal dimensions for a magnet system with two permanent magnets. To obtain the Lorentz force polynomial for one fixed design variable, it was necessary to carry out about 50 FEA-evaluations. One FEA-evaluation takes approximately 2 minutes. Although this was relatively time consuming, we were able to obtain very accurate results

using the polynomial approximation of the objective function.

Using the algorithm described above, it is possible to obtain the maximal drag force F_{max} for fixed MS weight m and thickness x_2 of the magnets. Figure 4.11 shows the dependencies of the maximal drag force F_{max} on x_2 for different values of m. The drag force reaches its maximal value at a different x_2 for every MS weight m. This Figure also makes the nonlinear behavior of all dependencies of F_{max} on x_2 clear. Moreover, as the MS weight increases, so does the optimal x_2.

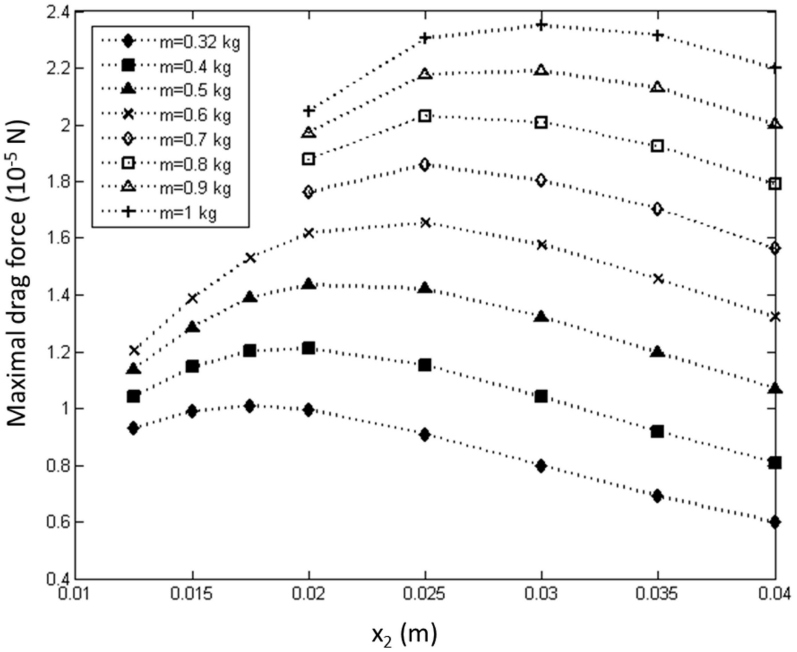

Figure 4.11: Maximal drag force F_{max} in relation to the thickness of PMs x_2 for different MS weight m in case of MS with 2 PMs, $x_g = 3$ mm, $B_r = 1.09$ T, $\rho = 7500$ kg/m^3; x_1 and x_3 are optimized to obtain the maximal drag force F_{max} at the fixed MS weight m

The maximal drag force in relation to the MS weight is represented in Figure 4.12, where it can be seen that there is almost linear dependence of the maximal drag force F_{max} on the MS weight m. Figure 4.12 also depicts the maximal drag force ratio to the MS weight F_{max}/m in relation to the MS weight. It indicates monotonic decay of F_{max}/m as m increases. At a MS weight of less than 320 g the required drag force of 10 μN is not achievable for the MS with two PMs. Therefore the corresponding curve in Figure 4.12 starts at $m = 0.32$ kg.

Looking at Figure 4.12, it becomes obvious that the optimal magnet system weight in the case of a magnet system with two PMs is 0.32 kg, since this weight corresponds to the drag force of 10 μN and to the highest efficiency. Corresponding design variables are

given in Table 4.2. The calibration coefficient K is in this case 0.379.

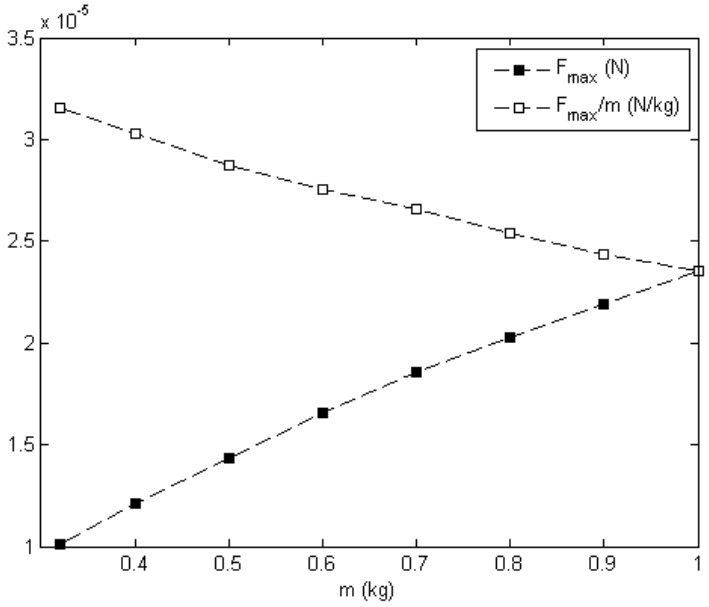

Figure 4.12: Maximal drag force F_{max} and its ratio to the MS weight in relation to the MS weight m in case of MS with two PMs.

Table 4.2: Optimization results for different magnet systems.

Magnet system	x_1 (m)	x_2 (m)	x_3 (m)	F_{max} (N)	m (kg)	F_{max}/m (N/kg)
2 PM	0.027	0.0175	0.0452	1.0e-5	0.32	3.125e-5
6 PM	0.0162	0.0125	0.044	2.45e-5	0.4	6.137e-5
10 PM	0.0136	0.01	0.0392	2.8e-5	0.4	6.99e-5

4.2.4 Optimization algorithm for three design variables using Least Square Fit

The optimization algorithm described in subsection 4.2.3 could be simplified, if were possible to find the polynomial $F(x_1, x_2, x_3)$. Then one would be able to remove the loop with changing x_2 and thus to considerably improve the speed, ease and accuracy of the optimization process. The optimization problem (4.13) could be then rewritten as [41]:

$$\begin{aligned} &Minimize \quad (-1) \cdot F(x_1, x_2, x_3) \\ &Subject \quad to \quad 2 \cdot \rho \cdot x_1 \cdot x_2 \cdot x_3 - m \leq 0 \\ &x_i^{low} \leq x_i \leq x_i^{up}, i = 1, ..., 3 \end{aligned} \tag{4.15}$$

The optimization flow chart is shown in Figure 4.13. First, the design space is initialized, i.e. for each design variable the lower, middle and upper values and the step

size are defined: $x_i = [x_i^{low} x_i^{mid} x_i^{up}]$, $\Delta x_i = x_i^{up} - x_i^{mid} = x_i^{mid} - x_i^{low}$. Second, the objective function is calculated for the given values of variables using the numerical model described previously. The polynomial expression of F($\mathbf{x}$) is obtained using the least square fit [35], [42]. It includes ten terms up to second order [41]:

$$F(x_1, x_2, x_3) = c_1 x_1^2 + c_2 x_1 x_2 + c_3 x_1 x_3 + c_4 x_1 + c_5 x_2^2 + c_6 x_2 x_3 + c_7 x_2 + c_8 x_3^2 + c_9 x_3 + c_{10}. \quad (4.16)$$

Here, c_i, i=1,...,10 are the coefficients of the polynomial. Once the polynomial has been obtained for the magnet system with its particular parameters, the optimization problem (4.15) can be formulated and solved. After that the step size Δx_i is refined around the optimizer x_i^{opt}. The new step size is $\Delta x_i^{new} = \Delta x_i / 3$. Then steps 1-3 of the optimization flow chart are repeated to obtain more accurate results.

Several tests gave the same results with this optimization technique as with the technique described in subsection 4.2.3. Usually, $\Delta x_i = 0.015$ m and one refinement were enough to reach the required precision. To perform the optimization process for given MS and its weight using polynomial (4.16) it is necessary to perform only 2·27=54 objective function evaluations, which is about five times fewer operations than were required using technique described in subsection 4.2.3.

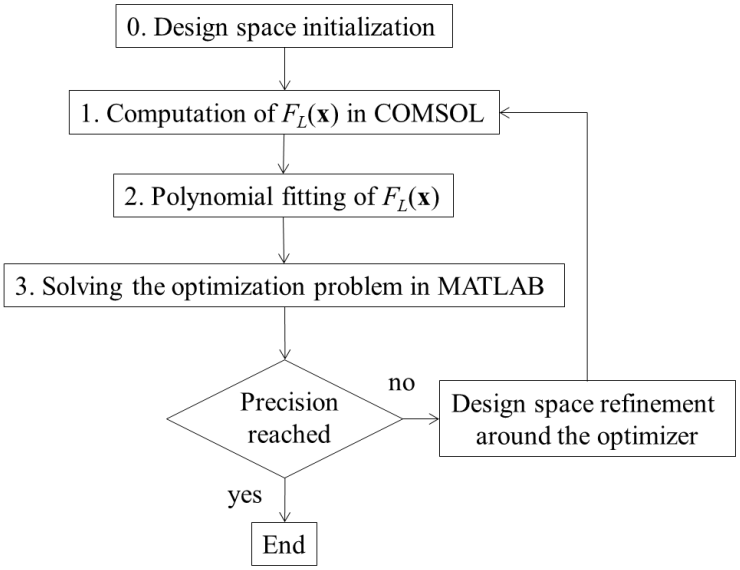

Figure 4.13: Optimization flow chart.

4.2.5 Validation of the polynomial expression for the objective function

The 2^{nd} order polynomial expression (4.16) was validated by comparison with 4^{th} order polynomial expression. The normalized by L design variables were bounded as follows: x_1/L=[0.49 0.69], x_2/L=[0.254 0.454], and x_3/L=[0.72 0.92]. To obtain the polynomial (4.16) the normalized step size $\Delta x_i/L = 0.1$ was used, i.e. the objective function was evaluated at three values of each design variable requiring 3^3=27 objective function evaluations.

The 4^{th} order polynomial has the following form:

$$F(x_1, x_2, x_3) = \sum_{r=1}^{35} c_r x_1^j x_2^k x_3^l, \quad 0 \leq j + k + l \leq 4, \tag{4.17}$$

where c_r are coefficients of the polynomial, $j = \{0, 1, 2, 3, 4\}$, $k = \{0, 1, 2, 3, 4\}$ and $l = \{0, 1, 2, 3, 4\}$. To obtain the polynomial (4.17) the normalized step size $\Delta x_i/L = 0.05$ was used, i.e. the objective function was evaluated at five values of each design variable requiring 5^3=125 objective function evaluations. The polynomials (4.16) and (4.17) were compared using the following expression:

$$\epsilon_{3DV} = \sqrt{\sum_{i=1}^{11}\sum_{j=1}^{11}\sum_{k=1}^{11}(F_{i,j,k} - F'_{i,j,k})^2 / \sum_{i=1}^{11}\sum_{j=1}^{11}\sum_{k=1}^{11} F^2_{i,j,k}} = 0.0025. \tag{4.18}$$

Here, $F_{i,j,k}$ and $F'_{i,j,k}$ are the objective function values evaluated using polynomials (4.16) and (4.17) at point $P(x_{1i}, x_{2j}, x_{3k})$ of the design space. In other words, each design variable had 11 values with the step size $\Delta x_i/L = 0.02$. It is notable that the relative error ϵ_{3DV} is sufficiently small. This means that the 2^{nd} and 4^{th} order polynomials provide almost the same values of the objective function at the same point P in the design space.

Table 4.3 lists the normalized by F_0 and L optimization results obtained using two polynomials (of 2^{nd} and 4^{th} order) for $m = 0.32$ kg. It is evident that the results obtained by using the 2^{nd} and the 4^{th} order polynomial for the objective function are almost the same. It will thus be acceptable to use the 2^{nd} order polynomial in the optimization procedure, since it requires considerably fewer objective function evaluations at each optimization step (27 instead of 125).

Table 4.3: Normalized optimization results using the 2^{nd} and the 4^{th} order polynomials for 3 DV ($m = 0.32$ kg).

Polynomial	F^{opt}/F_0	x_1^{opt}/L	x_2^{opt}/L	x_3^{opt}/L
2^{nd} order	3.397e-3	0.536	0.354	0.898
4^{th} order	3.404e-3	0.540	0.350	0.904
relative error	0.0021	0.0075	0.0113	0.0067

4.2.6 Effect of the averaged velocity profile on the optimization results

In this section, the effect of the averaged in time velocity profile on the optimization results is studied. In work [50] the averaged velocity profile in square channel with cross-section dimensions 50 mm × 50 mm was measured. The inlet velocity was 1 m/s. The goal of this section is to compare the optimization results for this experimental velocity profile and for solid body profile ($V = 1$ m/s).

The experimental velocity profile was fitted using the polynomial of order $q = 20$. Such high order of the polynomial was used to decrease the RMS error which was less than 0.02. Figure 4.14 plots the experimental velocity profile in the channel along the z axis. Figure 4.15 shows the fitted velocity profile on plane $x = 0$ from [50].

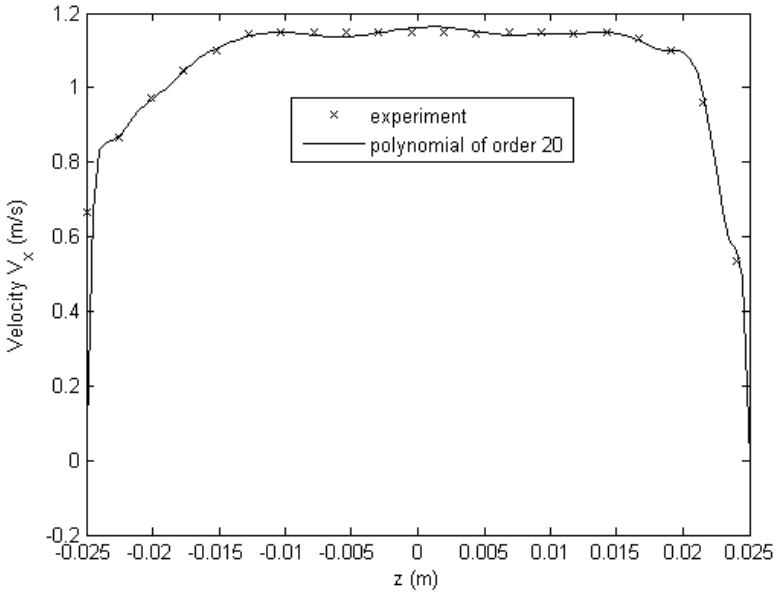

Figure 4.14: Experimental [50] and fitted velocity profile along the z axis in the channel with square cross-section $S = 50 \times 50$ mm^2, $V_{inlet} = 1$ m/s.

The optimization results for both experimental (fitted) and constant ($V = 1$ m/s) velocity profile for the magnet system with two magnets are given in Table 4.4. For

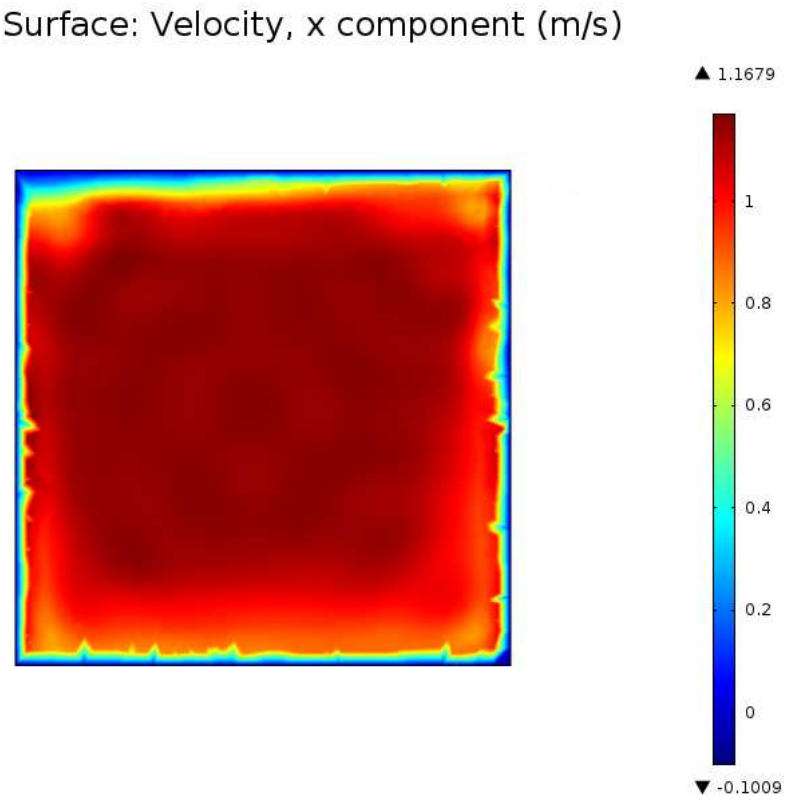

Figure 4.15: Fitted velocity profile on plane $x = 0$ from [50], $V_{inlet} = 1$ m/s .

Table 4.4: Optimization results for both experimental (fitted) and constant ($V = 1$ m/s) velocity profile for the magnet system with two magnets.

m/m_0	F^{opt}/F_0	x_1^{opt}/L	x_2^{opt}/L	x_3^{opt}/L
solid body ($V = 1$ m/s)				
1.067	1.586e-3	0.804	0.608	1.09
0.96	1.481e-3	0.79	0.57	1.066
0.8533	1.369e-3	0.752	0.54	1.052
0.7467	1.248e-3	0.716	0.508	1.026
turbulent flow ($V_{inlet} = 1$ m/s)				
1.067	1.622e-3	0.804	0.608	1.09
0.96	1.514e-3	0.802	0.566	1.056
0.8533	1.397e-3	0.772	0.536	1.032
0.7467	1.270e-3	0.716	0.508	1.026

$m/m_0 = 1.067$ and 0.7467 the optimizer (optimal dimensions of the magnets) is the same. Overall, the optimal Lorentz force for turbulent flow is about 2 % higher than for solid body. The optimization results are very similar for turbulent flow and for solid body approximation.

4.3 Magnetization pattern analysis inside the magnet

The analysis of the magnetization pattern inside the magnet was performed. Two types of magnetization pattern were investigated: periodic (see Figure 4.16) and Halbach array pattern.

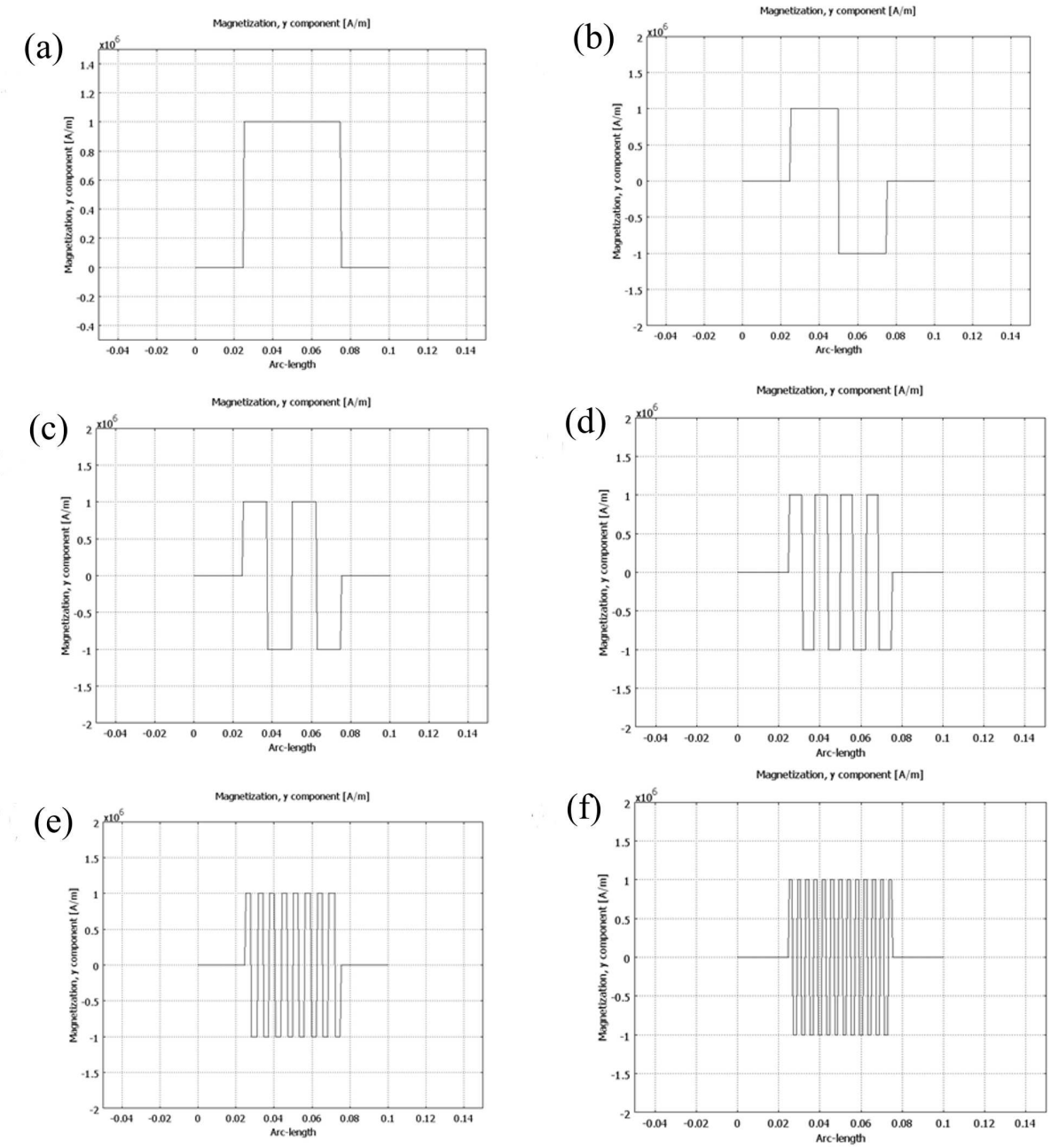

Figure 4.16: Magnetization pattern M_y in the magnet along the x-axis: (a) homogeneous, (b) alternating with 2 peaks, (c) alternating with 4 peaks, (d) alternating with 8 peaks, (e) alternating with 16 peaks, (f) alternating with 25 peaks.

We considered two magnet arrangements: one-sided and two-sided (see Figure 4.17). The input data are in accordance with the data given in Chapter 1. Only the magneti-

zation is slightly different for convenience: $M = 10^6$ A/m. The linear dimensions of the magnets are 50 mm, 25 mm, and 50 mm along the x, y, and z axes respectively.

First, the magnet in the one-sided arrangement and two magnets in the two-sided arrangements were magnetized along the x, y, and z axes respectively. The calculated drag force in the case of magnetization along the y axis is considerably higher than in the other two cases (see Table 4.5).

Table 4.5: Magnetization pattern analysis in the one- and two-sided PM arrangement.

Magnetization direction	Number of peaks	Drag force (N) for the one-sided PM arrangement	Drag force (N) for the two-sided PM arrangement
x	1	7.841e-6	1.261e-5
y	1	1.178e-5	2.881e-5
z	1	9.897e-7	2.725e-6

Further, the periodic magnetization pattern M_y along the x axis of the magnet was analyzed (see Figure 4.16). Figure 4.18(a) shows the drag force against the number of peaks n_p in the magnetization pattern M_y along the x axis inside the magnet for the one-sided and two-sided permanent magnet arrangements. It is notable that the drag force reaches its maximal value when $n_p = 2$ for both arrangements and decreases on further increase of n_p. Figure 4.18(b) plots the drag force ratio to the magnet system weight against n_p. It is evident that the two-sided PM arrangement is more efficient, since it provides a higher value for F/m.

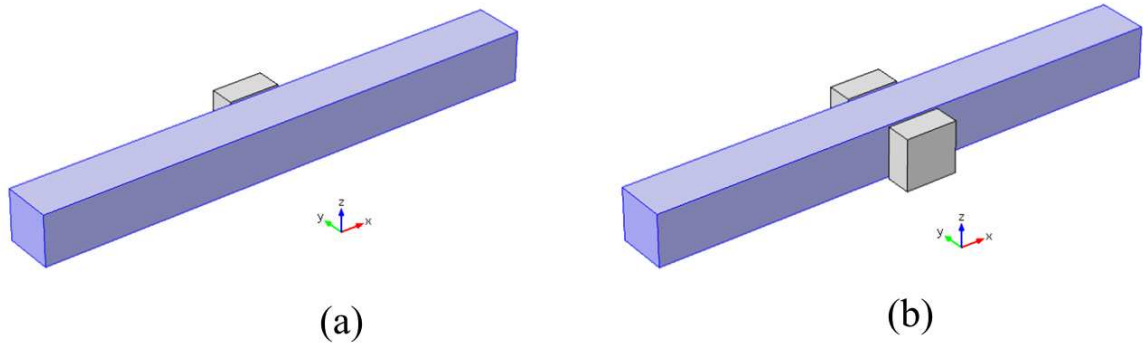

Figure 4.17: Permanent magnet arrangements: (a) one-sided and (b) two-sided.

After the periodic magnetization pattern in the one-sided and two-sided PM arrangements had been analyzed, the Halbach array pattern was investigated. Figure 4.19

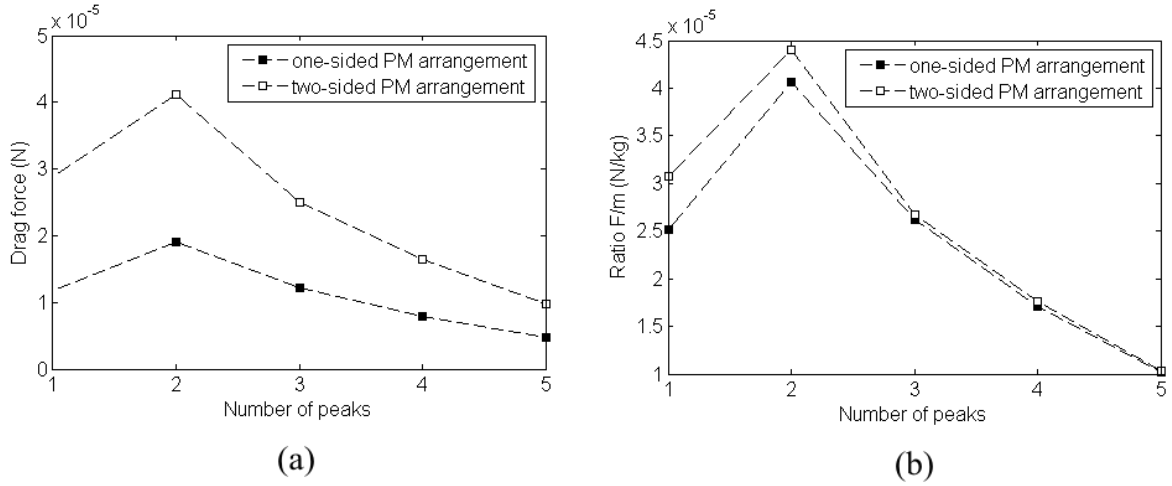

Figure 4.18: Drag force (a) and its ratio to MS weight (b) plotted against number of peaks for both one- and two-sided PM arrangements.

shows Halbach magnetization patterns for a two-sided PM arrangement. A one-sided Halbach pattern is, on the other hand, obtained by removing one of the Halbach arrays from either side of the two-sided Halbach arrangement. The arrows in Figure 4.19 show the direction of magnetization. Here we assumed that all magnets in the array have the same dimensions. The overall linear dimensions of each array along the x, y, and z axes are 50 mm, 25 mm, and 50 mm respectively. Input data are in accordance with the data given in Chapter 1 except for the magnetization, which is equal to 10^6 A/m.

Figure 4.20 plots the drag force (a) and its ratio to the MS weight (b) against the number of the magnets in one side of the Halbach array for both one- and two-sided Halbach arrays. Although the maximal drag force was obtained for 3 PMs per side ($N = 3$), whether in a one-sided or two-sided array (see Figure 4.19(c)), the two-sided Halbach array is more efficient than the one-sided Halbach array, since it provides higher efficiency, F/m (see Figure 4.20(b)). Moreover, the two-sided Halbach array provides $(F/m)_{max} \approx 6.6 \cdot 10^{-5}$ N/kg and the two-sided PM arrangement only $(F/m)_{max} \approx 4.5 \cdot 10^{-5}$ N/kg for the same MS weight, which proves that the Halbach array is more efficient than is the PM arrangement with a periodic magnetization pattern.

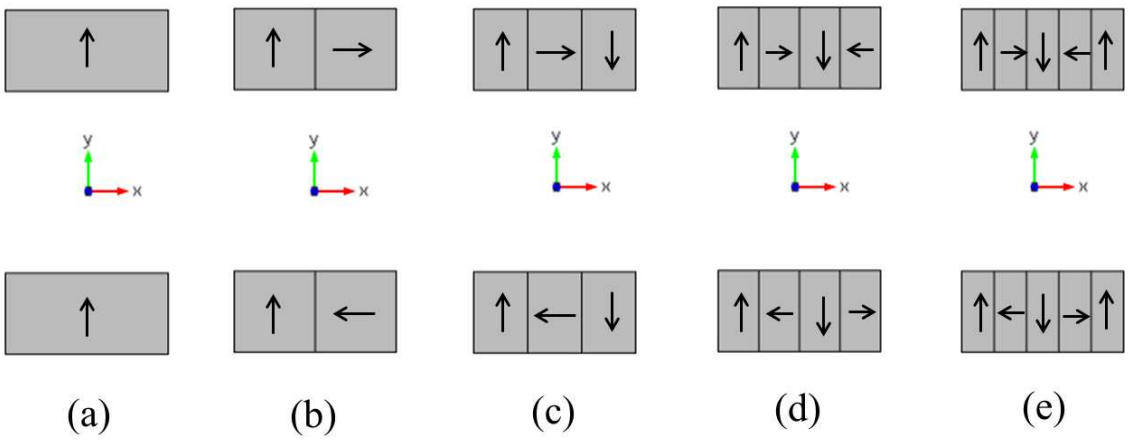

Figure 4.19: Two-sided Halbach arrays containing (a) 2 PMs, (b) 4 PMs, (c) 6 PMs, (d) 8 PMs, and (e) 10 PMs.

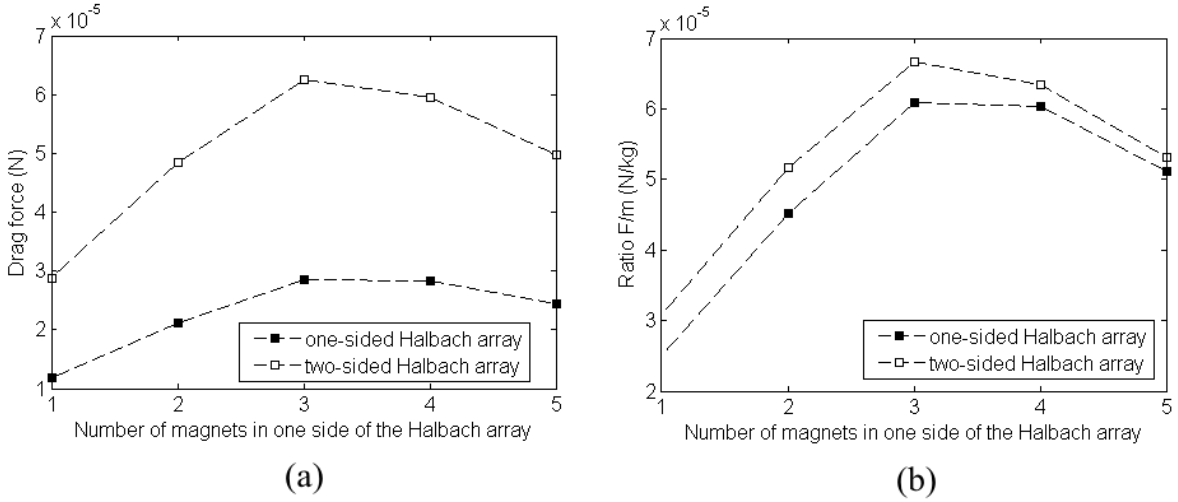

Figure 4.20: (a) Drag force plotted against number of magnets in one side of the Halbach array, for both one- and two-sided Halbach arrays; (b) ratio of drag force to MS weight plotted against number of magnets in one side of the Halbach array, for both one- and two-sided Halbach arrays.

4.4 Magnet system containing two Halbach arrays

4.4.1 Optimization of the magnet dimensions with three design variables using surface fitting tool

The magnet systems containing two Halbach arrays with $N = 3$ (in total 6 PMs) and $N = 5$ (in total 10 PMs) were investigated using the algorithm described in subsection 4.2.3 (see Figure 4.21(b) and (c)). One important assumption was made: all magnets had the same dimensions x_1, x_2, and x_3 along the x, y, and z axes, meaning that there were again only three design variables considered. The input data for this subsection are

given in Chapter 1. The maximal drag force in relation to the MS weight for each magnet system considered is represented in Figure 4.22. The maximal drag force F_{max} achieved by each magnet system depends in almost linear fashion on the MS weight m. To achieve the required drag force of 10 μN the MS weight of the MS with either 6 or 10 PMs is significantly less than for the MS with 2 PMs. Finally, Figure 4.23 depicts the maximal drag force ratio to the MS weight in relation to the MS weight for each considered MS.

The magnet system with 10 PMs is more efficient than the other two magnet systems, because it provides higher efficiency, F/m, at the same magnet system weight. Table 4.2 summarizes the optimization results for the magnet systems with 2, 6, and 10 PMs respectively.

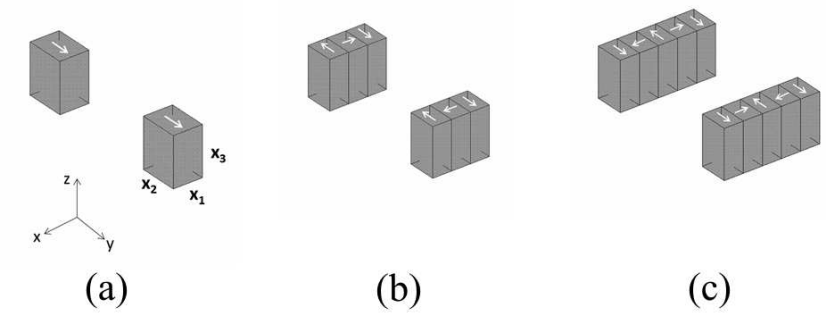

Figure 4.21: Magnet system with (a) 2, (b) 6, and (c) 10 PMs. Arrows depict the magnetization directions.

4.4.2 Optimization of the magnet dimensions with four design variables using Least Square Fit

In this subsection we consider the magnet system with two Halbach arrays (see Figure 4.24). Here, the number of magnets in each array is 3 ($N = 3$). Magnet systems containing two Halbach arrays with 5, 7 and 9 magnets in each array were also investigated (see Figure 4.25). The magnetization pattern in Figure 4.25 is identical to the pattern in a multipolar wiggler of the sort used for imparting periodic magnetic fields to electron beams so as to obtain laser beams or radiated beams [46]. As one can see in Figure 4.24, the optimization problem must be in respect of four design variables: odd and even magnets in the Halbach array can have different lengths (x_1 and x_4). Thus, the optimization problem (4.13) is as follows:

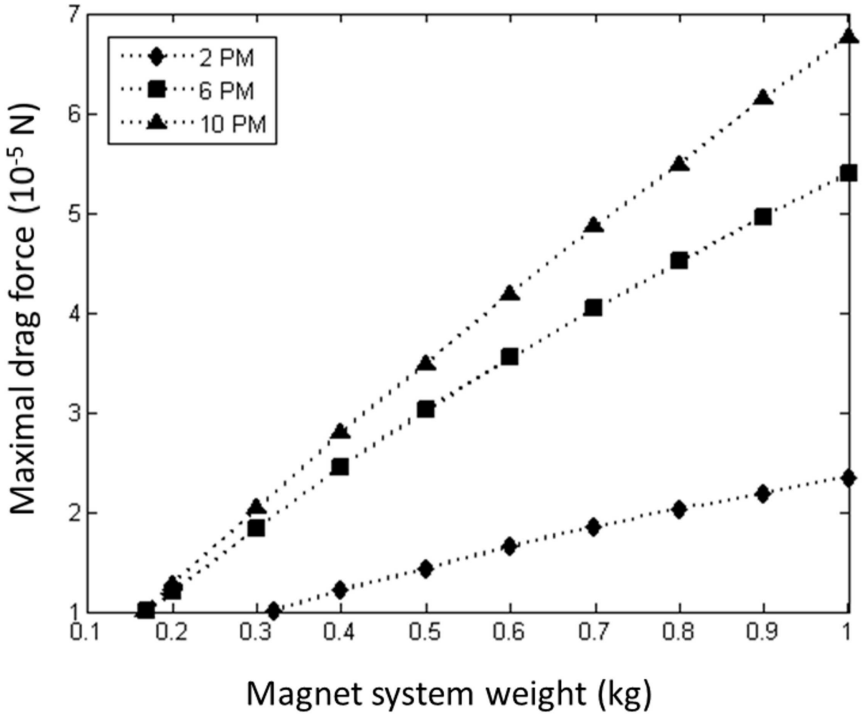

Figure 4.22: Maximal drag force F_{max} in relation to the MS weight m for MSs with 2, 6, and 10 PMs.

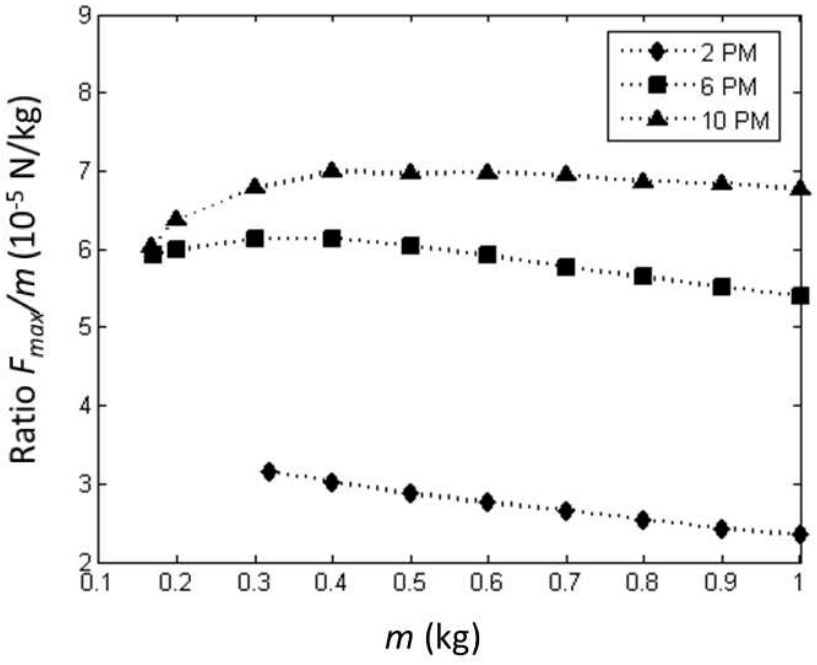

Figure 4.23: The ratio between the maximal drag force and the MS weight F_{max}/m plotted against the MS weight m for MSs with 2, 6, and 10 PMs.

$$\begin{aligned} &Minimize \quad (-1) \cdot F(x_1, x_2, x_3, x_4) \\ &Subject \quad to \quad 2 \cdot \rho \cdot x_2 \cdot x_3(n_1 \cdot x_1 + n_2 \cdot x_4) - m \leq 0, \\ &x_i^{low} \leq x_i \leq x_i^{up}, i = 1, ..., 4. \end{aligned} \tag{4.19}$$

Here, n_1 and n_2 are respectively the amounts of odd and even magnets in the Halbach array. Note that the odd magnets in the Halbach array are always magnetized along the y axis (crosswise spins) and the even magnets along the x axis (spanwise spins). The polynomial expression for the objective function (4.16) is here changed to:

$$F(x_1, x_2, x_3, x_4) = c_1 x_1^2 + c_2 x_1 x_2 + c_3 x_1 x_3 + c_4 x_1 x_4 + c_5 x_1 + c_6 x_2^2 + c_7 x_2 x_3 + c_8 x_2 x_4 + c_9 x_2 + c_{10} x_3^2 + c_{11} x_3 x_4 + c_{12} x_3 + c_{13} x_4^2 + c_{14} x_4 + c_{15}. \tag{4.20}$$

Here, c_i, i=1,...,15 are the coefficients of the polynomial. Once the polynomial has been obtained, the optimization problem (4.19) can be formulated and solved. After that, the step size Δx_i is refined around the optimizer ($\Delta x_i^{new} = \Delta x_i/2$) and stages 1, 2, and 3 of the optimization flow chart are repeated to obtain more accurate results (see subsection 4.2.4 and Figure 4.13). Here, $\Delta x_i = 0.01$ m and one refinement were enough to achieve required precision. Note that the additional design variable requires $3^4 - 3^3$=54 additional objective function evaluations at each optimization loop.

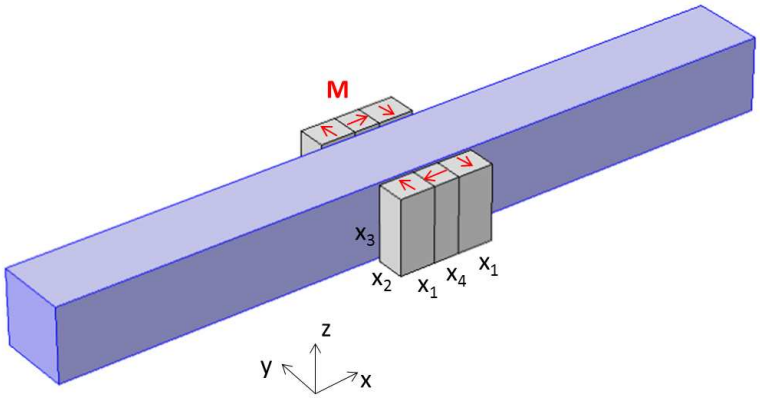

Figure 4.24: Magnet system comprising two Halbach arrays with 3 magnets in each array ($N = 3$).

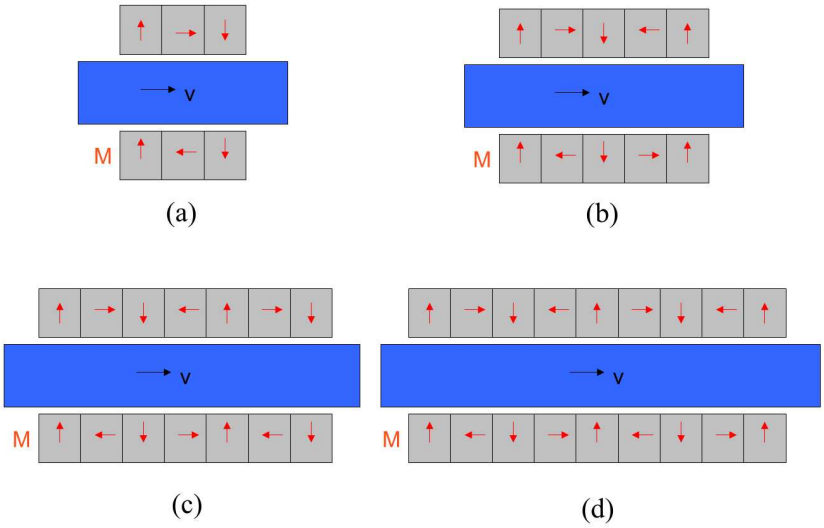

Figure 4.25: Top view of the electrolyte and the magnet system with two Halbach arrays: (a) N=3, (b) N=5, (c) N=7, and (d) N=9 magnets in each array.

4.4.3 Validation of the polynomial expression for the objective function

In this subsection, a magnet system with two Halbach arrays containing 6 magnets is under consideration (see Figure 4.24). The aim of this subsection was to compare the optimization results using the 2^{nd} and 4^{th} order polynomial expression of the objective function. The main input data are those given in Chapter 1. The design variables normalized by L are bounded as follows: x_1/L=[0.424 0.624], x_2/L=[0.302 0.502], x_3/L=[0.832 1.032], and x_4/L=[0.28 0.48]. The 2^{nd} order polynomial is given by (4.20). The 4^{th} order polynomial has the following form:

$$F(x_1, x_2, x_3, x_4) = \sum_{r=1}^{70} c_r x_1^j x_2^k x_3^l x_4^p, \quad 0 \leq j + k + l + p \leq 4, \tag{4.21}$$

where c_r are coefficients of the polynomial, $j = \{0, 1, 2, 3, 4\}$, $k = \{0, 1, 2, 3, 4\}$, $l = \{0, 1, 2, 3, 4\}$ and $p = \{0, 1, 2, 3, 4\}$. To obtain the polynomial (4.20) the normalized step size $\Delta x_i/L = 0.1$ was used, i.e. for each design variable three values were fixed, requiring 3^4=81 objective function evaluations in COMSOL Multiphysics. And to obtain the polynomial (4.21) the normalized step size $\Delta x_i/L = 0.05$ was used, i.e. five values for each design variable were fixed, requiring 5^4=625 objective function evaluations. The

polynomials (4.20) and (4.21) were compared using the following expression:

$$\epsilon_{4DV} = \sqrt{\sum_{i=1}^{11}\sum_{j=1}^{11}\sum_{k=1}^{11}\sum_{l=1}^{11}(F_{i,j,k,l} - F'_{i,j,k,l})^2 / \sum_{i=1}^{11}\sum_{j=1}^{11}\sum_{k=1}^{11}\sum_{l=1}^{11}F^2_{i,j,k,l}} = 0.0024. \qquad (4.22)$$

Here, $F_{i,j,k,l}$ and $F'_{i,j,k,l}$ are objective function values evaluated using polynomials (4.20) and (4.21) at point $P(x_{1i}, x_{2j}, x_{3k}, x_{4l})$ in the design space, respectively. The normalized step size used in (4.22) was $\Delta x_i/L = 0.02$. The relative error ϵ_{4DV} is sufficiently small. Thus, both polynomials provide almost the same objective function values at the same point P in design space.

Table 4.6 summarizes the normalized optimization results using both 2^{nd} and 4^{th} order polynomials for $m = 1$ kg. As in subsection 4.2.5, the optimization results are almost

Table 4.6: Normalized optimization results using 2^{nd} and 4^{th} order polynomial including 4 DV ($m = 1$ kg).

Polynomial	F^{opt}/F_0	x_1^{opt}/L	x_2^{opt}/L	x_3^{opt}/L	x_4^{opt}/L
2^{nd} order	1.844e-2	0.51	0.396	0.980	0.350
4^{th} order	1.848e-2	0.51	0.394	0.988	0.346
relative error	0.0025	0	0.0051	0.0082	0.0114

the same whether one uses the 2^{nd} or the 4^{th} order polynomial for the objective function. Thus, the 2^{nd} order polynomial can be used to optimize the magnet system with two Halbach arrays and four design variables, which is a substantial saving in computational effort.

4.4.4 Optimization of the number of magnets in two-sided Halbach arrays at constant magnet system weight

By keeping the magnet system weight constant it is possible to analyze the parameters of two-sided Halbach arrays which contain any number of equally dimensioned permanent magnets. Since Halbach arrays containing up to 10 magnets have already been reported on, this subsection is concerned with Halbach arrays containing 14, 18, 22, and 26 PMs. Figure 4.26 shows the geometry of a two-sided Halbach array containing 14 PMs ($N = 7$). Assuming that all magnets in the Halbach array have the same dimensions along the x, y, and z axes and that the MS weight is constant, e.g. 1 kg, one can derive the

nonlinear equality constraint, where 14 is the total number of magnets and 7500 kg/m^3 is the magnet density, and x_1, x_2, and x_3 are the linear dimensions of the magnets (see Figure 4.26):

$$14 \cdot 7500 \cdot x_1 \cdot x_2 \cdot x_3 = 1. \tag{4.23}$$

Further, by fixing x_2, e.g. $x_2 = 0.01$ m, the nonlinear equality constraint can be written as:

$$x_3 = \frac{1}{1050 \cdot x_1}. \tag{4.24}$$

Variable x_1 can then be changed, e.g. in the range from 0.01 m to 0.025 m in sufficiently small steps of, e.g. 0.0025 m. Parameter x_3 is related to x_1 in accordance with (4.24). Figure 4.27(a) plots the drag force against the variable x_1 with fixed $x_2 = 0.01$ m. It is evident that the maximal drag force is achieved at $x_1 = 0.0175$ m (variation 4). But this is not the absolute maximum, since this result was obtained for $x_2 = 0.01$ m and will change if x_2 is changing, as shown in Figure 4.27(b). The absolute maximal drag force for the magnet system shown in Figure 4.26 taking into account nonlinear equality constraint (4.23) was obtained by $x_1 = 0.0175$ m, $x_2 = 0.0125$ m, and $x_3 = 0.0435$ m, and is equal to $7.295 \cdot 10^{-5}$ N (see Figure 4.27(b)).

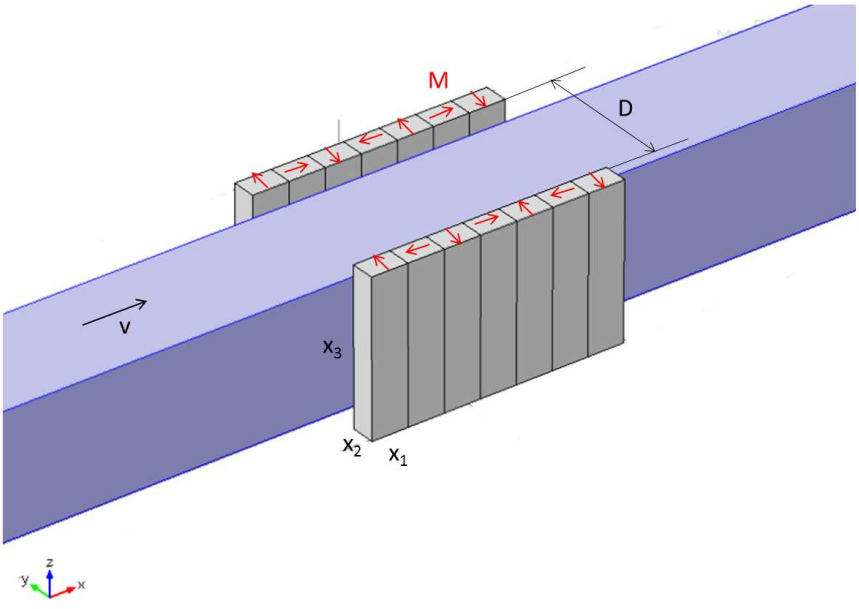

Figure 4.26: Geometry of two-sided Halbach array containing 14 PMs.

The same principle was used to analyze the magnet systems containing 18, 22, and 26 PMs. The magnetization pattern of these systems is analogous to pattern shown in

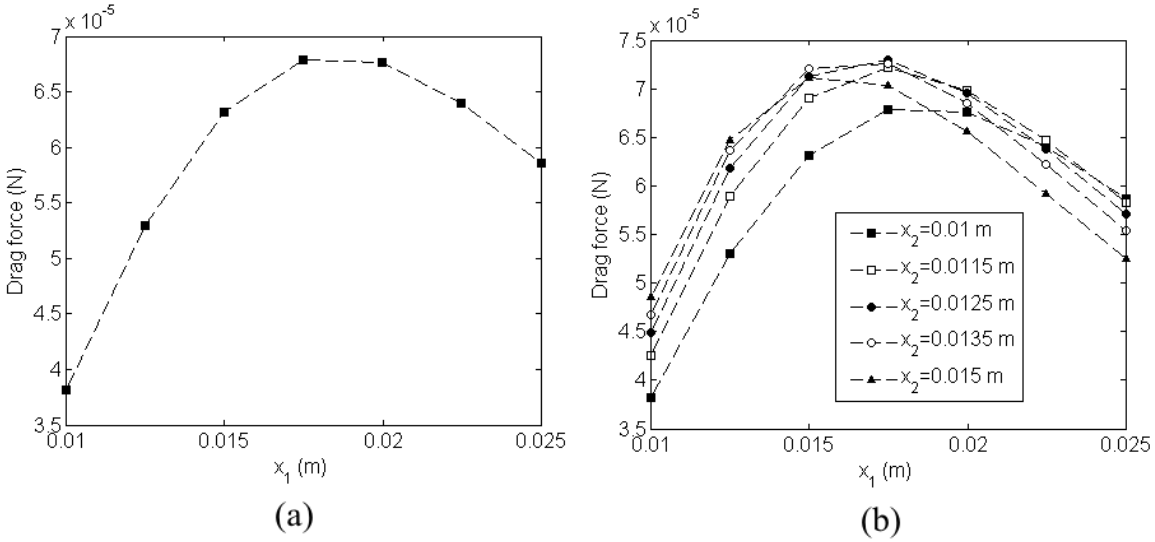

Figure 4.27: Drag force plotted against variable x_1 (a) for $x_2 = 0.01$ m and (b) for a different x_2.

Figure 4.25. The nonlinear equality constraint (4.23) is changed concerning the number of the magnets, e.g. for the magnet system including 18 PMs equation (4.23) is as follows: $18 \cdot 7500 \cdot x_1 \cdot x_2 \cdot x_3 = 1$. Table 4.7 summarizes the optimization results obtained for each magnet system and Figure 4.28 shows the maximal drag force against the number of permanent magnets in the magnet system when $m = 1$ kg. The results illustrate that at $m = 1$ kg and assuming that all magnets in the Halbach array have same dimensions x_1, x_2, and x_3 the maximum Lorentz force F_{max} increases nonlinearly with N, but saturates at $N = 11$. Two-sided Halbach array with $N = 9$ (with 18 magnets, see Figure 4.25(d)) represents a good compromise between efficiency and simplicity.

Table 4.7: Optimization results for two-sided Halbach arrays and with various numbers of magnets ($m = 1$ kg).

Number of PMs	x_1^{opt} (m)	x_2^{opt} (m)	x_3^{opt} (m)	Maximal drag force (N)
2	0.0409	0.03	0.0544	2.35e-5
6	0.0218	0.02	0.051	5.397e-5
10	0.0186	0.015	0.0478	6.762e-5
14	0.0175	0.0125	0.0435	7.295e-5
18	0.015	0.0115	0.0429	7.552e-5
22	0.015	0.01	0.0404	7.664e-5
26	0.015	0.009	0.038	7.596e-5

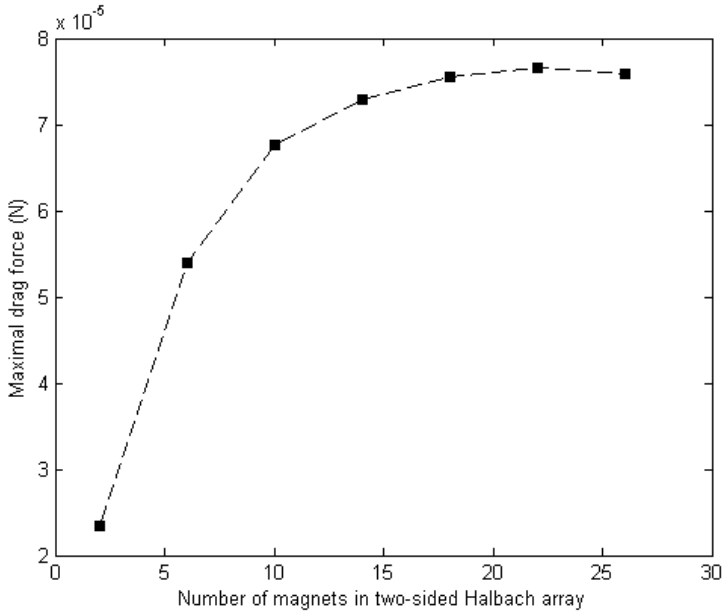

Figure 4.28: Maximal drag force plotted against number of PMs in two-sided Halbach array ($m = 1$ kg).

4.4.5 Optimization of longitudinal dimensions of the magnets in two-sided Halbach arrays at constant magnet system weight

This subsection reports on modeling the effect of changing the longitudinal dimensions of the odd and even magnets in a two-sided Halbach array on the drag force. Figure 4.29 shows a two-sided Halbach array with 6 PMs ($N = 3$). The magnet dimensions L_{my} and L_{mz} are fixed and equal to 0.02 m and 0.051 m, respectively, for all magnets. These dimensions were found in the previous subsection for $m = 1$ kg (see Table 4.7). The longitudinal dimensions of the magnets in the odd rows are denoted by x_1 and in the even row by x_4 (see Figure 4.29). The equality constraint then can be written as

$$2 \cdot 7500 \cdot L_{my} \cdot L_{mz}(2 \cdot x_1 + x_4) = 1. \tag{4.25}$$

From (4.25) following relation can be derived

$$x_4 = (1 - 30.6 \cdot x_1)/15.3. \tag{4.26}$$

Then variable x_1 was changed ranging from 0.018 m to 0.026 m in 0.5 mm steps. Variable x_4 was changed in accordance with relation (4.26). Figure 4.30 plots the drag force against the variable x_1. The maximal drag force, achieved at $x_1 = 0.024$ m and

$x_4 = 0.0174$ m, proved to be $5.48 \cdot 10^{-5}$ N. This value is approximately 1.5 % higher than value achieved previously for $x_1 = x_4 = 0.0218$ m (see Table 4.7).

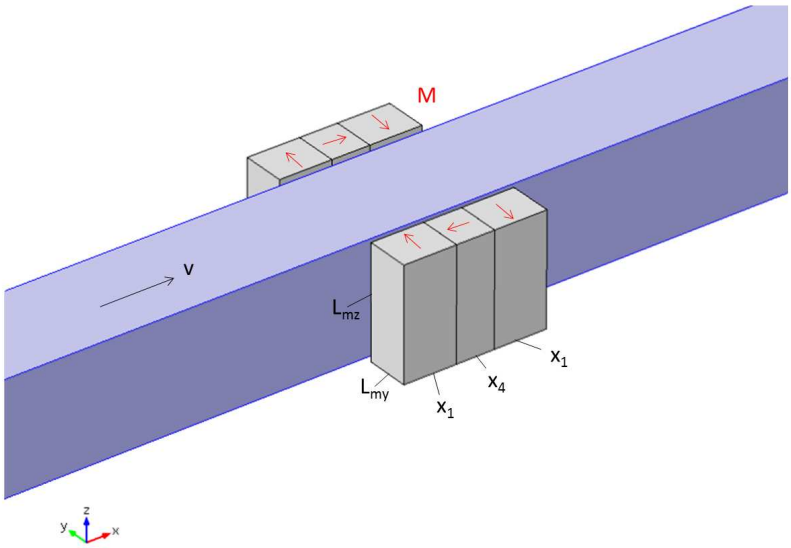

Figure 4.29: Two-sided Halbach array containing 6 PMs with different longitudinal magnets dimensions in odd and even rows.

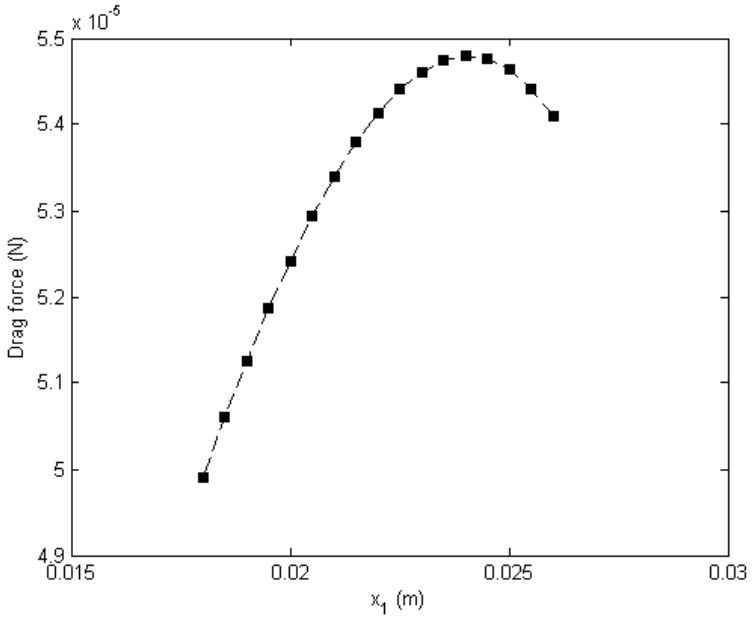

Figure 4.30: Drag force against variable x_1 for a two-sided Halbach array containing 6 PMs (see Figure 4.29).

The same principle was used to investigate two-sided Halbach arrays including 10, 14, and 18 PMs. The equality constraint can be written for each Halbach array as follows:

- for Halbach array containing 10 PMs ($N = 5$):

$$2 \cdot 7500 \cdot 0.015 \cdot 0.0478(3 \cdot x_1 + 2 \cdot x_4) = 1 => x_4 = (1 - 32.265 \cdot x_1)/21.51, \qquad (4.27)$$

- for Halbach array containing 14 PMs ($N = 7$):

$$2 \cdot 7500 \cdot 0.0125 \cdot 0.0435(4 \cdot x_1 + 3 \cdot x_4) = 1 => x_4 = (1 - 32.625 \cdot x_1)/24.46875, \quad (4.28)$$

- and for Halbach array containing 18 PMs ($N = 9$):

$$2 \cdot 7500 \cdot 0.0115 \cdot 0.0429(5 \cdot x_1 + 4 \cdot x_4) = 1 => x_4 = (1 - 37.00125 \cdot x_1)/29.601. \quad (4.29)$$

Table 4.8 summarizes the results of this subsection. The effect of changing the longitudinal dimensions of the magnets in Halbach arrays on the drag force is not significant. The drag force can be increased only by 1.5 % for a Halbach array with 6 PMs, by 0.6 % for a Halbach array with 10 PMs, by 0.3 % for a Halbach array with 14 PMs, and by 0.1 % for a Halbach array with 18 PMs.

Table 4.8: Optimization results for different two-sided Halbach arrays and different length of odd and even magnets in arrays ($m = 1$ kg).

Halbach array	L_{my} (m)	L_{mz} (m)	x_1^{opt} (m)	x_4^{opt} (m)	Maximal drag force (N)
6 PM	0.02	0.051	0.024	0.0174	5.48e-5
10 PM	0.015	0.0478	0.02	0.0165	6.803e-5
14 PM	0.0125	0.0435	0.019	0.0155	7.319e-5
18 PM	0.0115	0.0429	0.0155	0.0144	7.559e-5

4.5 Optimization results

The initial optimization parameters for all cases studied are gathered in Table 4.9. The maximum streamwise component of the Lorentz force and its ratio to the maximum

Table 4.9: Parameters defining the initial constraints applied on magnet systems.

N	m/m_0	x_1^{min}/L	x_1^{max}/L	x_2^{min}/L	x_2^{max}/L	x_3^{min}/L	x_3^{max}/L	x_4^{min}/L	x_4^{max}/L
1	1.067	0.4	1.4	0.2	0.8	0.4	1.4	n/a	n/a
3	1.067	0.2	0.8	0.2	0.8	0.6	1.2	0.2	0.8
5	1.067	0.2	0.8	0.15	0.75	0.6	1.2	0.2	0.8
7	1.067	0.2	0.6	0.15	0.55	0.6	1	0.2	0.6
9	1.067	0.2	0.6	0.15	0.55	0.6	1	0.2	0.6

weight of the magnet system are plotted against the maximum weight of the magnet system in Figures 4.31 (a) and (b), respectively. Unsurprisingly, the maximum Lorentz

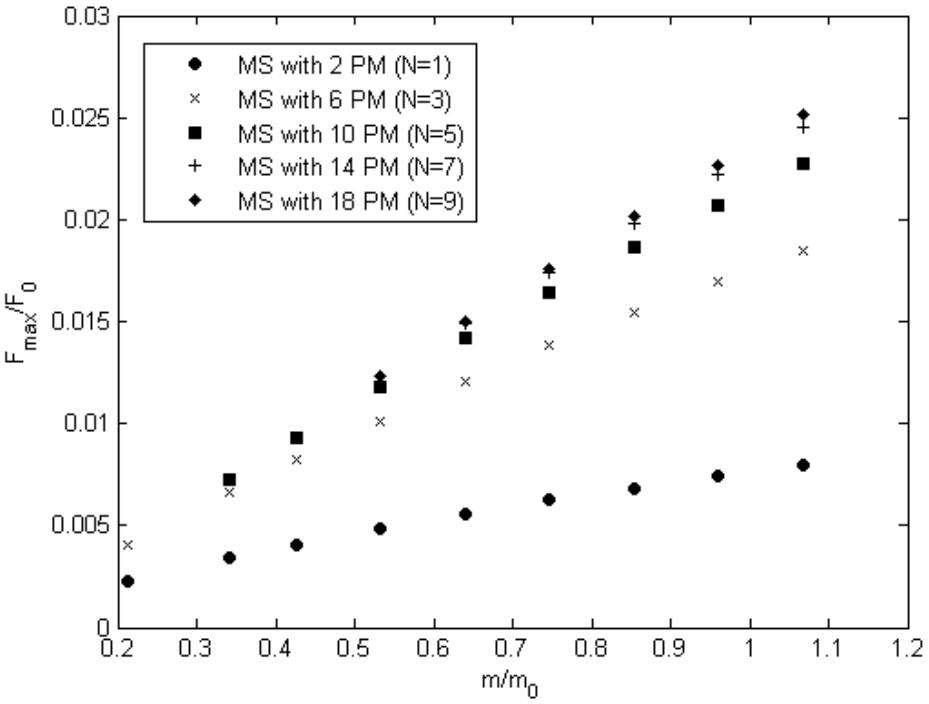

(a)

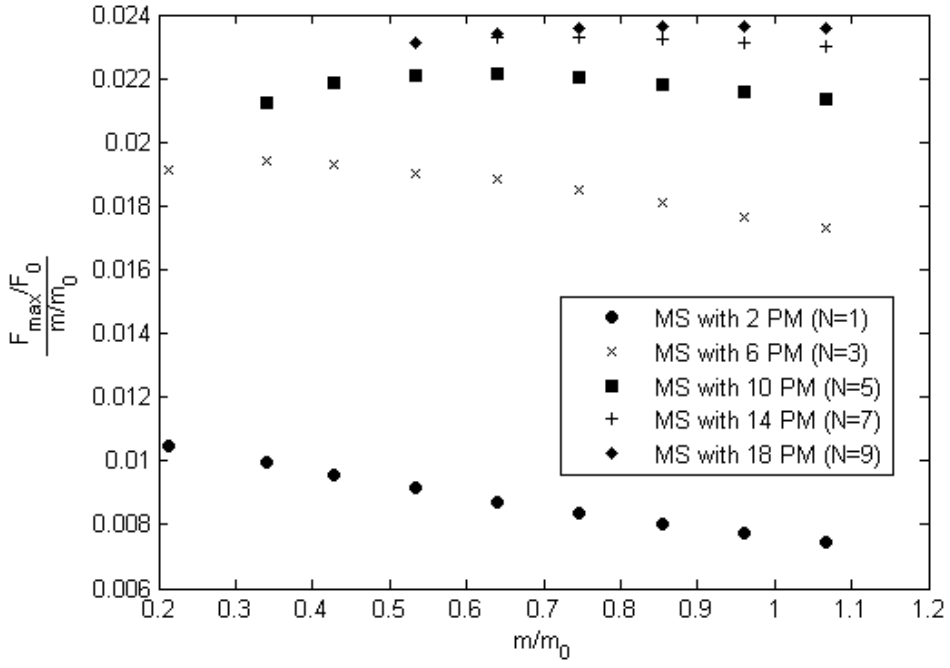

(b)

Figure 4.31: (a) maximum Lorentz drag force plotted against the maximum weight of the magnet system; (b) ratio between the maximum Lorentz drag force and the maximum weight of the magnet system plotted against the maximum weight of the magnet system.

force increases with the weight (or mass) of the magnet system, regardless of the chosen magnet configuration (parametrized by N). This also explains why the optimal mass is always the maximum mass imposed. For a given mass, however, the Lorentz force increases with N but saturates. Interestingly, the variations of F_{max} are strongly sub-linear for smaller N but become more and more linear for larger N, suggesting that for low mass systems $N = 3$ already nearly produces the maximum Lorentz force, whereas for $m/m_0 \in [0.4\ 1]$, $N = 7$ is the best compromise between optimal Lorentz force and simplicity, as the Lorentz force is practically the same as for $N = 9$ over this interval. One can expect that more complex magnet systems become advantageous for $m/m_0 > 1$. The subject of variations in the ratio of the maximum Lorentz force to the maximum system weight versus m is more complex: while it decreases for $N = 1$ but presents a maximum when $N > 1$, this maximum is not very clearly marked and occurs at mildly increasing magnet system weight when N increases, but varies little in value between $N = 3$ and $N = 9$. While $N = 3$ brings a significant enhancement of this ratio over $N = 1$, more complex magnet systems ($N > 3$) bring relatively little further improvement.

Optimal dimensions of the magnets for $N = 1, 3, 7$, and 9 are plotted against the maximum magnet system's weight in Figure 4.32. All of them increase with m. For $N = 1$ (magnet system with two magnets) they increase sub-linearly with m and the optimal streamwise aspect ratio of the magnets x_3^{opt}/x_1^{opt} decreases from 1.68 (at $m/m_0 = 0.3413$) to 1.36 (at $m/m_0 = 1.067$), as shown in Figure 4.33(a). The optimal spanwise aspect ratio of the magnets x_2^{opt}/x_1^{opt} increases from 0.66 (at $m/m_0 = 0.3413$) to 0.76 (at $m/m_0 = 1.067$). Thus, magnets of the optimizing and heavier systems made of a single pair of magnets are closer to a cubic shape. A similar tendency is observed for magnet systems based on Halbach arrays ($N > 1$). The dependence of the optimal aspect ratios on m however becomes weaker as N increases, and optimal magnet shape tend to become shorter along the streamwise and spanwise direction: e.g., for $N = 9$, the optimal ratio x_3^{opt}/x_1^{opt} is almost constant (around 2.43) while the ratio x_2^{opt}/x_1^{opt} varies from 0.53 (at $m/m_0 = 0.427$) to 0.67 (at $m/m_0 = 1.067$). Also, odd magnets (magnetized along the y axis) are slightly more elongated in the x direction than the even magnets (magnetized along the x axis). This tendency accentuates for heavier system with a ratio x_4^{opt}/x_1^{opt} decreasing from 0.98 (at $m/m_0 = 0.427$) to 0.88 (at $m/m_0 = 1.067$), as shown in Figure

4.33(d).

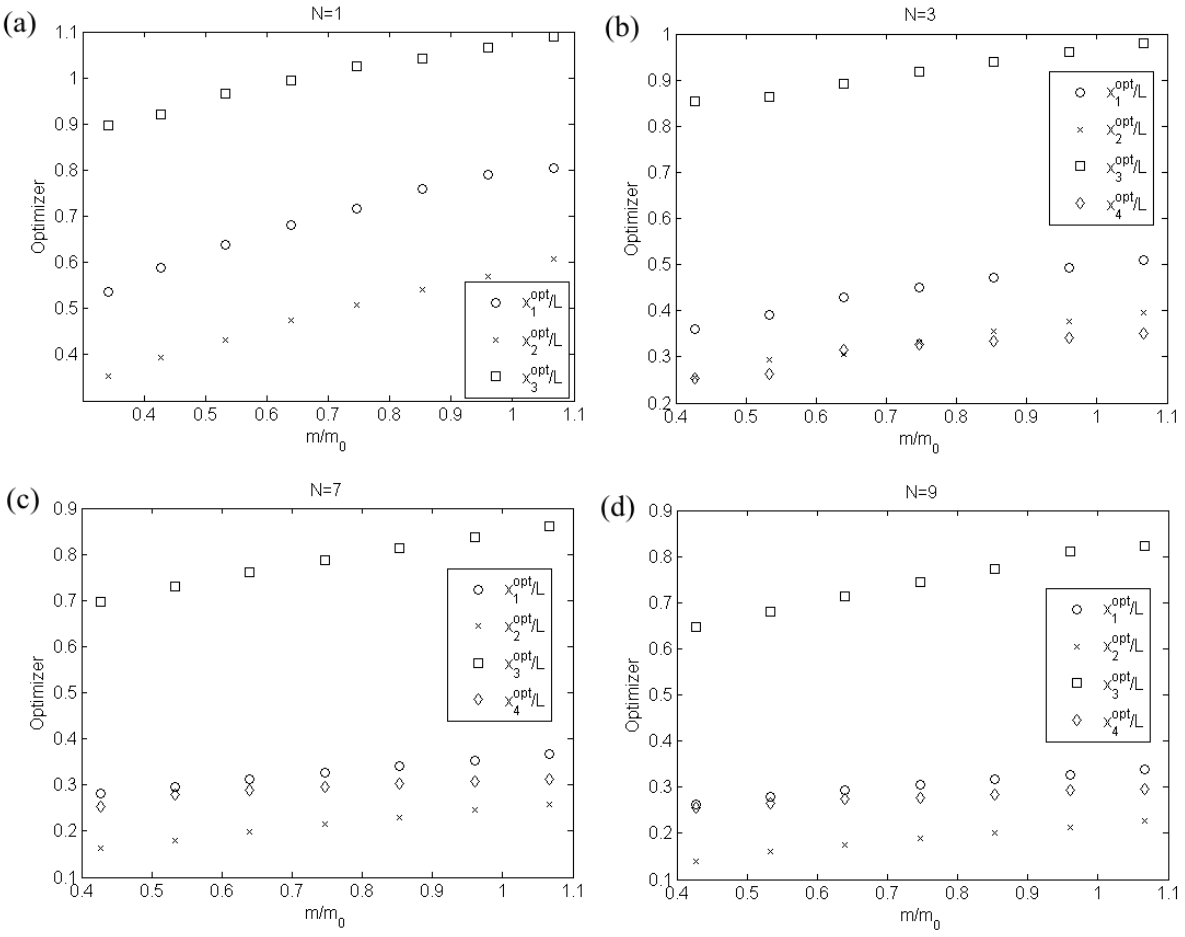

Figure 4.32: Optimal dimensions of the magnets for: (a) $N = 1$, (b) $N = 3$, (c) $N = 7$, and (d) $N = 9$ plotted against the maximum weight of the magnet system.

The features of the magnet systems yielding the highest efficiency $(F_L^{opt}/F_0)/(m/m_0)$ for each value of N are gathered in table 4.10. Overall, in the interval of m/m_0 we considered, the most efficient magnet system is a two-sided Halbach array including eighteen magnets ($N = 9$), since it provides both the highest Lorentz drag force and efficiency. One could expect that the performances of the magnet system would continue to increase at higher values of N. The corresponding optimal mass would, however, increase beyond the values of interest in this work, which were set to ensure a relatively compact system ($m \leq 1$ kg).

The optimization results for each considered magnet system and its mass are given in appendix A.

Figures 4.34 - 4.39 show contour plots of the y component of the magnetic flux

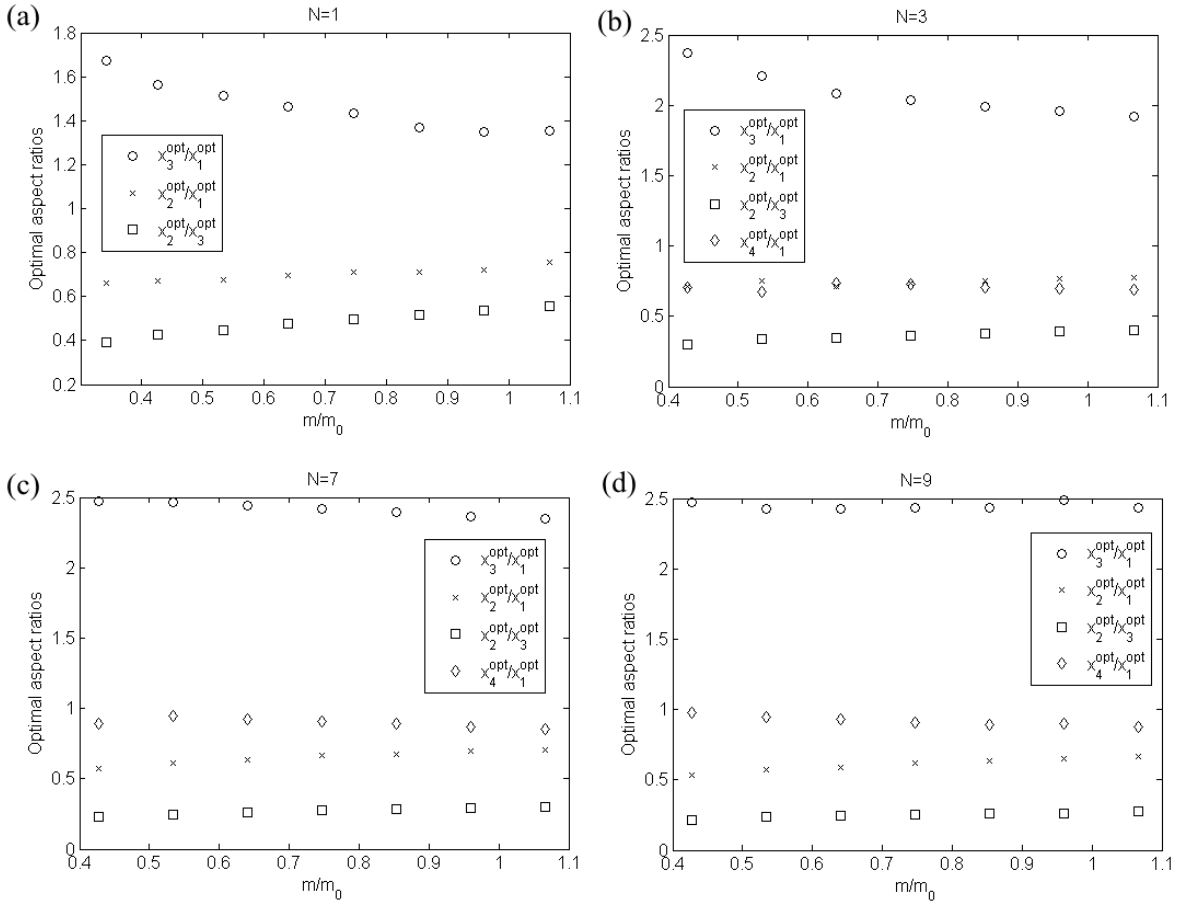

Figure 4.33: Optimal aspect ratios of the magnets for: (a) $N = 1$, (b) $N = 3$, (c) $N = 7$, and (d) $N = 9$ plotted against the maximum weight of the magnet system.

Table 4.10: Normalized optimization results.

N	x_1^{opt}/L	x_2^{opt}/L	x_3^{opt}/L	x_4^{opt}/L	F_L^{opt}/F_0	m^{opt}/m_0
1	0.536	0.354	0.898	-	3.3970e-3	0.3413
3	0.338	0.228	0.804	0.254	6.6308e-3	0.3413
5	0.346	0.240	0.806	0.304	1.4171e-2	0.64
7	0.326	0.216	0.788	0.296	1.7388e-2	0.7467
9	0.330	0.214	0.798	0.290	2.2676e-2	0.96

density $\mathbf{B}$, z component of the current density $\mathbf{J}$, and x component of the Lorentz force density $\mathbf{f_L}$ on $x - y$ symmetry plane for an optimized MS with 2 PMs and 10 PMs, respectively (see Table 4.10).

The highest magnetic flux density B_y is concentrated near the poles of the magnets (see Figure 4.34). There is consequently higher current density J_z near the channel walls (see Figure 4.35), if the velocity of the medium in the channel along the x axis is constant. Finally, as shown in Figure 4.36, the x component of the Lorentz force density f_{Lx} (which is mainly the product of J_z and B_y) reaches its maximal values near the channel walls.

Note that the Lorentz force density f_{Lx} is negative, whereas the velocity is positive along the x axis.

Figure 4.37 plots the contours of B_y for the magnet system containing 10 permanent magnets. Here, the magnetization inside the magnets changes its sign along the x axis (see also Figure 4.25(b)). The highest magnetic flux density is concentrated near the poles magnetized across the flow (the first, third, and fifth pairs of the magnets). One can see in Figure 4.38 that higher current density J_z is concentrated in regions with higher magnetic flux density B_y. It is to be noted that the current density J_z changes its sign along the x axis. Finally, as in the case of the magnet system with two permanent magnets, the highest Lorentz force density is concentrated in regions with the highest y component of the magnetic flux density B_y (see Figure 4.39). Note that the x component of the Lorentz force density f_{Lx} does not change its sign and is always negative if velocity is positive along the x axis.

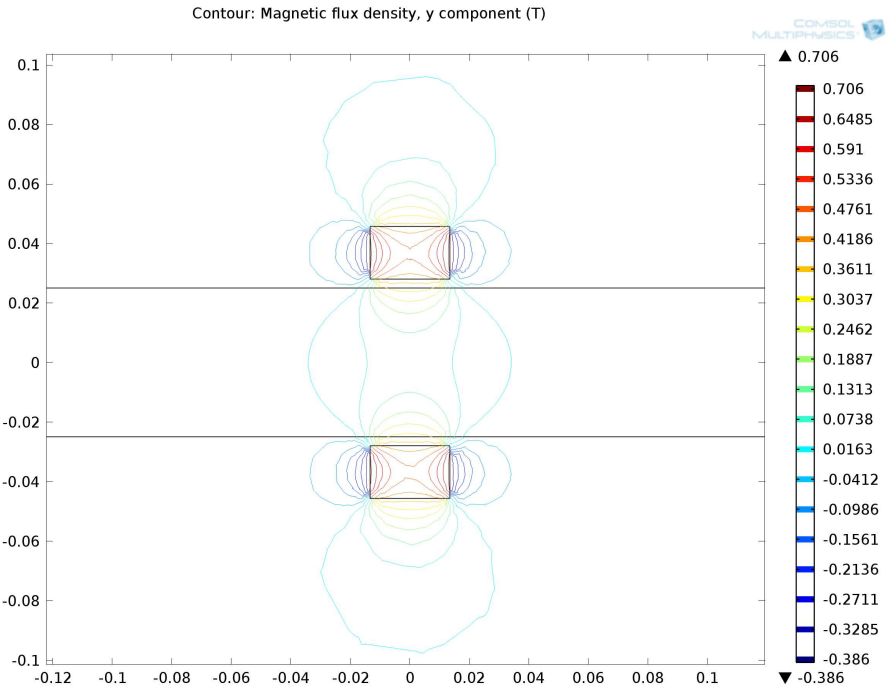

Figure 4.34: Magnetic flux density B_y contour plot on $x-y$ symmetry plane for an optimized MS with 2 PMs ($z = 0$).

4.6 Sensitivity analysis

To complete our analysis, we evaluated how robust are some of the optimal designs found in the previous section to uncontrolled variations of some of the parameters defining

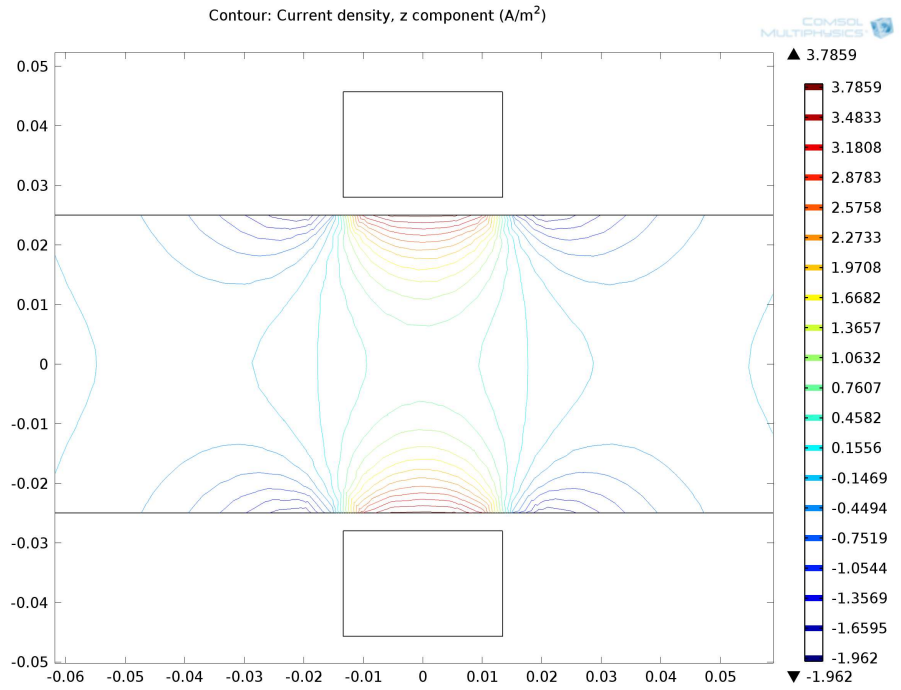

Figure 4.35: Current density J_z contour plot on $x-y$ symmetry plane for an optimized MS with 2 PMs ($z=0$).

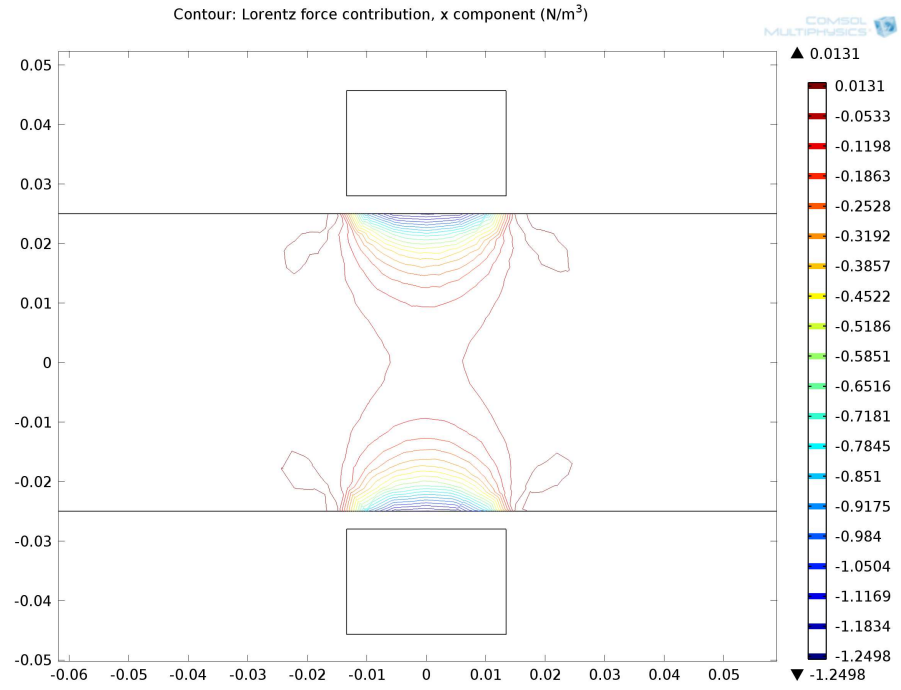

Figure 4.36: Lorentz force density f_{Lx} contour plot on $x-y$ symmetry plane for an optimized MS with 2 PMs ($z=0$).

the problem. The sensitivity for the magnet system with two magnets ($N=1$), ten magnets ($N=5$), and eighteen magnets ($N=9$) was analyzed. The relative sensitivity

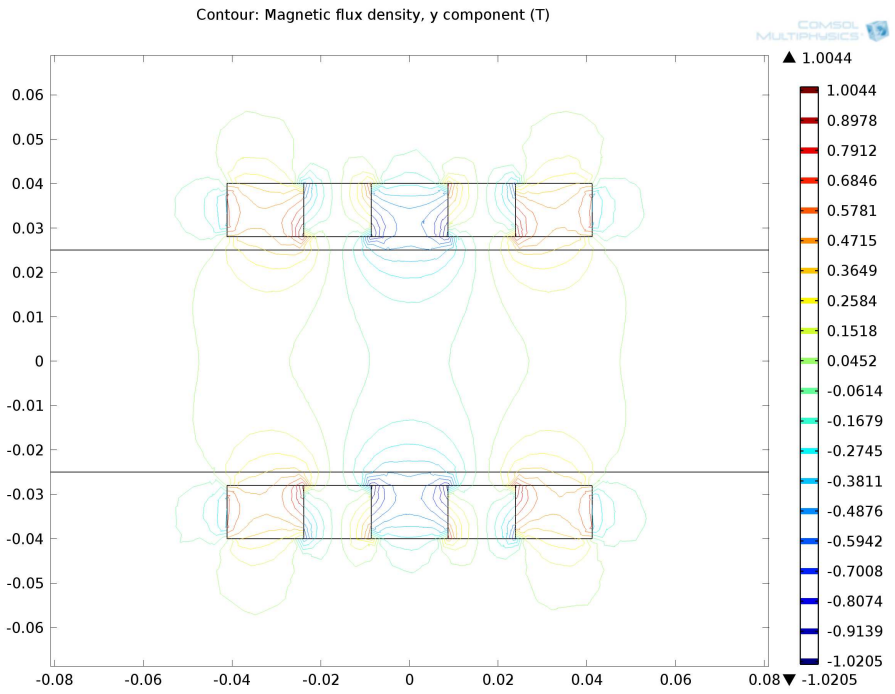

Figure 4.37: Magnetic flux density B_y contour plot on $x-y$ symmetry plane for an optimized MS with 10 PMs ($z=0$).

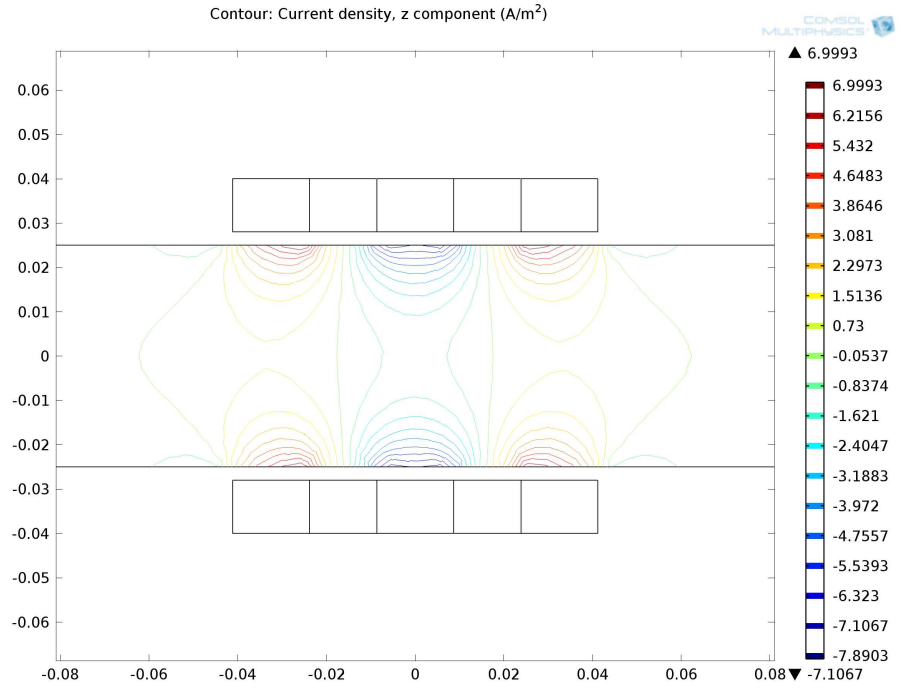

Figure 4.38: Current density J_z contour plot on $x-y$ symmetry plane for an optimized MS with 10 PMs ($z=0$).

of the maximum Lorentz force to a given variable is defined and estimated as:

$$S_X(F_L) = \frac{X^{opt}}{F_L^{opt}} \frac{\partial F_L}{\partial X}(X^{opt}) \simeq \frac{F_L^{opt}((1+\eta)X^{opt}) - F_L^{opt}(X^{opt})}{\eta F_L^{opt}} \tag{4.30}$$

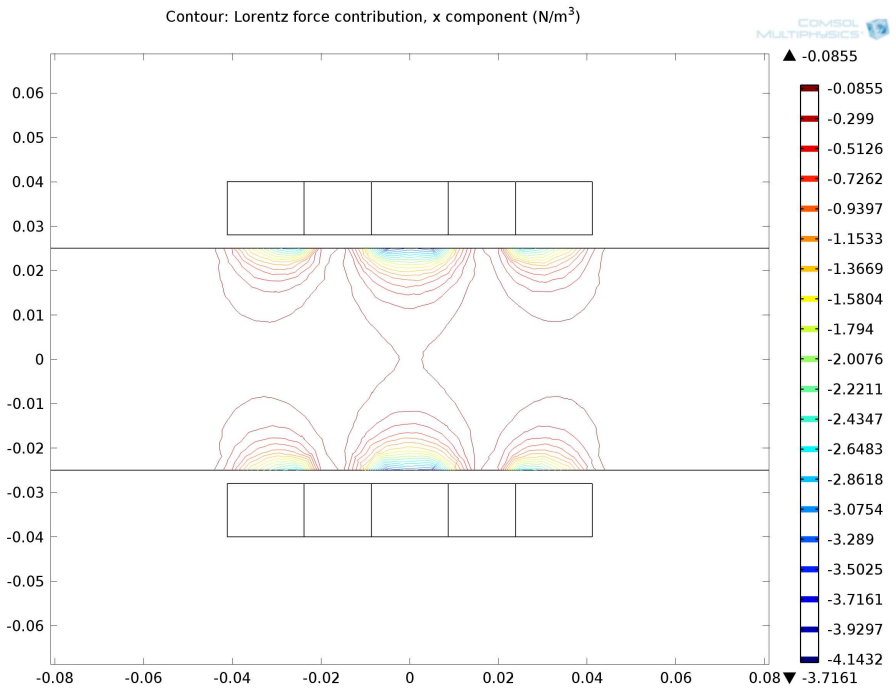

Figure 4.39: Lorentz force density f_{Lx} contour plot on $x-y$ symmetry plane for an optimized MS with 10 PMs ($z=0$).

We arbitrarily evaluated S_X for a relative increase of η in X, X being in turn, V_0, σ_0, M_0, y_0, and z_0, where y_0 and z_0 were the y- and z-position of the duct centerline (we have assumed $y_0 = z_0 = 0$ until now). The relative increase η was chosen to be 5 % for all disturbed parameters, except for y_0 for which $\eta = 1$ %, since $y_0 \leq 1$ mm, where 1 mm is the air gap between the duct walls and magnets. The sensitivity of design variables x_1, x_2, x_3 and x_4 was defined in a similar way.

Tables 4.11, 4.12, and 4.13 summarize the results of sensitivity analysis for $N = 1$, $N = 5$ and $N = 9$ respectively. It is noteworthy that the optimizer is not sensitive to V_0, σ_0 and M_0 for all N. Secondly, the sensitivity of F_L is nearly 1 to V_0 and σ_0 and nearly 2.05 to M_0 for all N. This means that when increasing V_0 or σ_0 by 5 %, the optimal drag force also increases by 5 %, while increasing M_0 by 5 % leads to increase of F_L by about 10 %. Thirdly, unlike V_0, σ_0, and M_0, the relative position of the duct to the magnet system (y_0, z_0) influences both the optimizer and the resulting Lorentz force. In particular, the positive sensitivity $S_{y_0}(F_L)$ increases with N and negative sensitivity $S_{z_0}(F_L)$ decreases. It is therefore crucial to ensure a perfectly symmetric position of the magnet system with respect to the duct.

Table 4.11: Sensitivity analysis results for $N = 1$ and m/m_0=1.067, for which the optimal parameters were found to be $F_L^{opt}/F_0 = 7.9347 \cdot 10^{-3}$, x_1^{opt}/L=0.814, x_2^{opt}/L=0.604, and x_3^{opt}/L=1.084.

Disturbance parameter X	$S_X(x_1)$	$S_X(x_2)$	$S_X(x_3)$	$S_X(F_L)$
V_0	$1.93 \cdot 10^{-4}$	$1.05 \cdot 10^{-4}$	$1.17 \cdot 10^{-4}$	1.000
σ_0	$1.93 \cdot 10^{-4}$	$1.06 \cdot 10^{-4}$	$1.17 \cdot 10^{-4}$	1.000
M_0	$2.88 \cdot 10^{-4}$	$-5.96 \cdot 10^{-6}$	$1.34 \cdot 10^{-4}$	2.050
y_0	0.403	−0.500	0.103	0.296
z_0	0.375	0.258	−0.619	−0.072

Table 4.12: Sensitivity analysis results for $N = 5$ and m/m_0=1.067, for which the optimal parameters were found to be $F_L^{opt}/F_0 = 2.2894 \cdot 10^{-2}$, $x_1^{opt}/L = 0.406$, $x_2^{opt}/L = 0.308$, $x_3^{opt}/L = 0.914$, and $x_4^{opt}/L = 0.338$.

X	$S_X(x_1)$	$S_X(x_2)$	$S_X(x_3)$	$S_X(x_4)$	$S_X(F_L)$
V_0	−0.007	0.008	$4.38 \cdot 10^{-4}$	−0.008	1.000
σ_0	−0.007	0.008	$4.38 \cdot 10^{-4}$	−0.008	1.000
M_0	−0.007	0.008	$4.38 \cdot 10^{-4}$	−0.008	2.050
y_0	−0.177	0.156	0.031	−0.201	0.506
z_0	−0.090	−0.038	0.089	0.020	−0.235

Table 4.13: Sensitivity analysis results for $N = 9$ and m/m_0=0.96, for which the optimal parameters were found to be $F_L^{opt}/F_0 = 2.2769 \cdot 10^{-2}$, x_1^{opt}/L=0.326, x_2^{opt}/L=0.212, x_3^{opt}/L=0.81, and x_4^{opt}/L=0.294.

X	$S_X(x_1)$	$S_X(x_2)$	$S_X(x_3)$	$S_X(x_4)$	$S_X(F_L)$
V_0	−0.001	0.013	−0.003	−0.022	1.000
σ_0	−0.001	0.013	−0.003	−0.022	1.000
M_0	$-3.70 \cdot 10^{-4}$	0.013	-0.003	−0.023	2.050
y_0	−0.362	0.208	0.136	−0.320	0.663
z_0	−0.017	0.057	−0.057	0.029	−0.248

Chapter 5

Conclusions

1. The use of Lorentz Force Velocimetry (LFV) for low conducting material has been investigated numerically.

2. A numerical model of LFV was developed using commercially available COMSOL Multiphysics software.

3. The main goal of the investigation was to optimize the magnet system for fixed velocity (5 m/s) and conductivity (4 S/m) of an electrolyte, fixed cross-section dimensions of the electrolyte (0.05 m $\times$ 0.05 m), fixed distance between the electrolyte and magnet system (3 mm), and no change in the material of the magnets (Nd-Fe-B). Optimizing in this instance means maximizing the Lorentz force and minimizing the weight of the magnet system.

4. There were predefined restrictions on the Lorentz force F_L and the magnet system weight, which were due to the measurement system available. The limits to be satisfied were: $F_L \geq 10$ μN and $m \leq 1$ kg.

5. The numerical model was verified for the magnetic field using analytical methods from the literature. Those methods are based on the distribution of the electric current (method 1) and on the distribution of the charge (method 2).

6. The numerical model was validated for the Lorentz force using the experimental data provided by our colleagues.

7. Almost all results of this work were obtained assuming a constant velocity profile for the electrolyte (solid body approximation). This assumption reduces computing time substantially. Time taken by the CPU is highly relevant in the optimization process, which for one fixed MS weight required several dozen F_L evaluations using the numerical

model.

8. The solid bar approximation was validated using experimental data and, also, numerically, using the k-ϵ turbulence model. These tests showed very little difference in the Lorentz force for a solid and a turbulent velocity profile (less than 5 %). Therefore the optimized magnet dimensions for a solid body are taken to be valid for turbulent flow.

9. The low Rm approximation ($Rm \ll 1$) showed that there was no need to couple the partial differential equations employed.

10. Symmetry conditions allowed us to reduce the computation domain by a factor of 4 for $N = 1$ and by a factor of 2 for $N > 1$. This reduced computational costs considerably.

11. The different magnet systems (Halbach arrays) were optimized using the optimization toolbox in MATLAB. In the optimization toolbox, *fmincon* function was used. This function will find the maximum of a constrained nonlinear multivariate function F_L. The active-set method and sequential quadratic programming (SQP) were used in the context of the *fmincon* function.

12. Least square fit was used to obtain the polynomial expression for the objective function. Validation of the polynomial expression was performed: optimization using 2^{nd} and 4^{th} order polynomials was accomplished for $N = 1$ and $N = 3$. As the difference between the results was negligible, the 2^{nd} order polynomial was accepted, since it requires fewer objective function evaluations in COMSOL Multiphysics.

13. Sensitivity analysis of the optimal solution was carried out for v, σ, M, and the position of the channel relative to magnet system along the y and z axis (y_0 and z_0) for N =1, 5, and 9. The optimal values for the design variables are insensitive to v, σ, and M and sensitive to y_0 and z_0. The sensitivity of Lorentz force in respect of v and σ is approximately 1 and in respect of M about 2.05 for all N. The absolute value of the sensitivity the Lorentz force to position of the duct increases with N.

14. A magnet system containing eighteen magnets ($N = 9$) and with optimized magnet dimensions proved to be the most suitable for given input data and constraints which were defined at the start of the work.

15. The maximum Lorentz force increases with the mass of the magnet system, regardless of the chosen magnet configuration. For a given mass, the Lorentz force in-

creases with N but saturates. For low mass systems, $N = 3$ already produces almost the maximum Lorentz force, whereas for $m/m_0 \in [0.4\ 1]$, $N = 7$ is the best compromise between optimal Lorentz force and simplicity, as the Lorentz force is practically the same as for $N = 9$ over this interval. One can expect that more complex magnet systems will be advantageous for $m/m_0 > 1$.

16. The efficiency of the magnet system with two magnets ($N = 1$) was increased by 14.5 % after optimization of the magnets' dimensions: $F_L/m = 2.7537 \cdot 10^{-5}$ N/kg before optimization and $F_L/m = 3.1531 \cdot 10^{-5}$ N/kg after optimization.

17. The efficiency of the magnet system with eighteen magnets ($N = 9$) was increased by 57 % after optimization of the magnets' dimensions: $F_L/m = 4.7666 \cdot 10^{-5}$ N/kg before optimization and $F_L/m = 7.4837 \cdot 10^{-5}$ N/kg after optimization.

18. Thanks to using Halbach arrays with optimized dimensions of the magnets the efficiency of the magnet system was increased by a factor of 2.72: $F_L/m = 2.7537 \cdot 10^{-5}$ N/kg for $N = 1$ before optimization and $F_L/m = 7.4837 \cdot 10^{-5}$ N/kg for $N = 9$ after optimization.

19. The numerical tests showed that the Lorentz force can be increased further by means of modification of the cross-section dimensions of the channel. To do so, the channel height h can be increased and the channel width w as well as the distance between the magnets D can be decreased.

20. Because of the low Hartmann number ($Ha < 1$), the effect of the Lorentz force on the flow of electrolyte was omitted in the numerical simulations, i.e. the kinematic approach was used with a constant velocity profile of the electrolyte.

Bibliography

[1] J. A. Shercliff, The theory of electromagnetic flow-measurement, Cambridge University Press, 1962.

[2] A. Thess, Y. Kolesnikov, Ch. Karcher, Method and arrangement for the contactless inspection of moving electrically conductive substances, US Patent 2008/0252287 A1.

[3] N. Ida, J. Bastos, Electromagnetics and calculation of fields, Springer-Verlag New York, Inc., 1992.

[4] A. Thess, E. Votyakov, B. Knaepen, and O. Zikanov, Theory of the Lorentz force flowmeter, *New Journal of Physics* 9 (2007) 299.

[5] A. A. Alferenok and A. B. Kuvaldin, Numerical simulation of the heat-and-mass transfer in the channel of an induction furnace for making cast iron, *Russian Metallurgy (Metally)*, Vol. 2009, No. 8, pp. 741-747.

[6] R. Klein, A. Potherat, and A. Alferenok, An experiment on a confined, electrically driven vortex pair, *Physical Review E*, Vol. 79, issue 1, id 016304.

[7] A. Thess, E. V. Votyakov, and Y. Kolesnikov, Lorentz Force Velocimetry, *Physical Review Letters*. Vol. 96, 164501, 2006.

[8] A. Thess, Y. Kolesnikov, Ch. Karcher, E. Votyakov, Lorentz Force Velocimetry - A contactless technique for flow measurement in high-temperature melts, Proceedings of 5th International Symposium on Electromagnetic Processing of Materials, pp. 731-734, 2006.

[9] R. Klein, C. Weidermann, X. Wang, M. Gramss, A. Alferenok, A. Thieme, Y. Kolesnikov, C. Karcher, A. Thess, Lorentzkraft-Anemometrie für die berührungslose Durchflussmessung von Metallschmelzen, *Technisches Messen* 79 (2012) 9.

[10] A. Wegfrass, C. Diethold, M. Werner, T. Froehlich, B. Halbedel, F. Hilbrunner, C. Resagk, and A. Thess, A universal noncontact flowmeter for liquids, *Applied physics letters* 100, 194103 (2012).

[11] A. Wegfrass, C. Diethold, M. Werner, A. Alferenok, C. Resagk, T. Fröhlich, B. Halbedel, U. Lüdtke, A. Thess, Lorentzkraft-Anemometrie für die berührungslose Durchflussmessung von Elektrolyten, *Technisches Messen* 79 (2012) 9.

[12] J. S. Choi, J. Yoo, Optimal design method for magnetization directions of a permanent magnet array, *Journal of Magnetism and Magnetic Materials*, 322, pp. 2145-2151, 2010.

[13] E. P. Furlani, Permanent magnet and electromechanical devices. Materials, analysis, and applications, *Academic Press*, 2001.

[14] F. Herlach and N. Miura, High Magnetic Fields: *Science and Technology*, vol. 1. World Scientific Publishing Co. Pte. Ltd, 2003.

[15] M. Werner, B. Halbedel, E. Raedlein, Numerical study of magnet systems for Lorentz force velocimetry in electrically low conducting fluids, Proceedings of 6th International Scientific Colloquium *Modelling for Material Processing*, pp. 233-238, 2010.

[16] J. Jin, The finite element method in electromagnetics, *John Wiley & Sons, Inc.*, 1993.

[17] M. Ziolkowski and H. Brauer, Fast Computation Technique of Forces Acting on Moving Permanent Magnet, *IEEE Transactions on Magnetics*. Vol. 46, No. 8, 2010.

[18] User's Guide for COMSOL Multiphysics.

[19] J. D. Jackson, Classical electrodynamics, John David Jackson, 3rd edition, 1999.

[20] P. H. Roberts, Introduction to Magnetohydrodynamics, Longmans, 1967.

[21] P. A. Davidson, An Introduction to Magnetohydrodynamics, Cambridge University Press, 2001.

[22] D. Lee and H. Choi, Magnetohydrodynamic turbulent flow in a channel at low magnetic Reynolds number *J. Fluid. Mech* **439**, 367-394, 2001.

[23] AC/DC module in COMSOL Multiphysics 3.5a *Users Guide*

[24] COMSOL Multiphysics 3.5a *Reference Guide*

[25] Y. Saad, A flexible inner-outer preconditioned GMRES algorithm, *SIAM J. Sci. Statist. Comput.*, **14**, 461-469, 1993.

[26] W. Hackbusch, Multi-grid methods and applications, Springer Verlag 1985.

[27] A. Greenbaum, Iterative methods for linear systems *Frontiers in Appl. Math.*, **17** (SIAM), 1997.

[28] Y. Saad and M. H. Schultz, GMRES: A generalized minimal residual algorithm for solving nonsymmetric linear systems *SIAM J. Sci. Statist. Comput.* **7**, 856-869, 1986.

[29] X. Gou, Y. Yang, X. Zheng, Analytic expression of magnetic field distribution of rectangular permanent magnets, *Applied Mathematics and Mechanics*, Vol. 25, No. 3, pp. 297-306, 2004.

[30] A. N. Mladenovic, S. R. Aleksic, Determination of magnetic field for different shaped permanent magnets, 7th International Symposium on Electromagnetic Compatibility and Electromagnetic Ecology, 2007, pp. 84-87.

[31] V. Minchenya, Ch. Karcher, Yu. Kolesnikov, A. Thess, Dry calibration of the Lorentz force flowmeter, *Magnetohydrodynamics*, Vol. 45, No. 4, pp. 569-578, 2009.

[32] A. Alferenok, U. Luedtke, Numerical simulation and magnet system optimization for the Lorentz Force Velocimetry (LFV) of low-conducting fluids, Proceedings of 6th International Scientific Colloquium *Modelling for Material Processing*, pp. 215-220, 2010.

[33] A. Alferenok, U. Lüdtke, Numerische Simulation und Optimierung von Magnetsystemen für die Lorentzkraft-Strömungsmessung mit elektrisch schwach leitfähigen Flüssigkeiten, Workshop Elektroprozesstechnik, 23.-24. September 2010.

[34] C. Stelian, A. Alferenok, U. Lüdtke, Yu. Kolesnikov, A. Thess, Optimization of a Lorentz force flowmeter by using numerical modeling, *Magnetohydrodynamics*, Vol. 47 (2011), No. 3, pp. 273-282.

[35] P. Venkataraman, Applied optimization with MATLAB programming, John Wiley & Sons, Inc., Hoboken, New Jersey, 2009.

[36] P. E. Gill, W. Murray, M. H. Wright, Practical optimization, Academic Press Inc., London, 1981.

[37] MATLAB R2012a documentation (The MathWorks Inc).

[38] M. J. D. Powell, A fast algorithm for nonlinearly constrained optimization calculations *Lecture Notes in Mathematics*, Vol. 630, Springer Verlag, 1978.

[39] M. Werner, B. Halbedel, Anwendung von Halbacharrays in der Lorentzkraftanemometrie, Workshop Elektroprozesstechnik, 2011.

[40] A. Alferenok, M. Werner, M. Gramss, U. Luedtke, and B. Halbedel, Numerical optimization of the magnet system for the Lorentz Force Velocimetry of electrolytes. *Int. Journal of Applied Electromagnetics and Mechanics*, 38 (2012), pp. 79-92.

[41] A. Alferenok, U. Lüdtke, Optimization of Halbacharrays for the Lorentz Force Velocimetry of low conducting materials using numerical simulation, Workshop Elektroprozesstechnik, 6.-7. September 2012.

[42] E. K. P. Chong, S. H. Zak, An Introduction to Optimization, 3rd ed., John Wiley & Sons, Inc., Hoboken, New Jersey, 2008.

[43] J. C. Mallinson, One sided fluxes - A magnetic curiosity? *IEEE Transactions on Magnetics* Vol. MAG. 9, No. 4, 1973.

[44] J.-S. Choi and J. Yoo, Design of a Halbach magnet array based on optimization techniques, *IEEE Transactions on Magnetics*. Vol. 44, No. 10, 2008.

[45] J.-S. Choi, J. Yoo, S. Nishiwaki, and K. Izui, Optimization of magnetization directions in a 3-D magnetic structure, *IEEE Transactions on Magnetics*. Vol. 46, No. 6, 2010.

[46] T. Okazaki, Multipolar wiggler, U.S. Patent 5,420,556, 1995.

[47] A. Alferenok, U. Lüdtke, Improvement of the magnet system sensitivity for the flow rate measurement based on Lorentz force velocimetry considering low conducting fluids by means of numerical modeling, Workshop Elektroprozesstechnik, 6.-7. Oktober 2011.

[48] Chemical engineering module of COMSOL Multiphysics, *Reference Guide*.

[49] L. Ignat, D. Pelletier and F. Ilinca, A universal formulation of two-equation models for adaptive computation of turbulent flows, *Computer meth. in appl. mech. and eng.*, **189**, pp. 1119-1139, 2000.

[50] A. Wegfrass, Experimentelle Untersuchungen zur Anwendbarkeit der Lorentzkraft-Anemometrie auf schwach leitfähige Fluide, Dissertation, 2012.

[51] A. Alferenok, A. Potherat and U. Lüdtke, Optimal magnet configurations for Lorentz Force Velocimetry in low conductivity fluids (to be published)

Appendices

Appendix A

Optimization results

1) $N = 1$:

m/m_0	x_1^{opt}/L	x_2^{opt}/L	x_3^{opt}/L	F_L^{opt}/F_0
0.3413	0.536	0.354	0.898	0.0033970
0.4267	0.588	0.394	0.92	0.0040794
0.5333	0.638	0.432	0.966	0.0048770
0.64	0.68	0.474	0.994	0.0055870
0.7467	0.716	0.508	1.026	0.0062361
0.8533	0.76	0.54	1.042	0.0068455
0.96	0.79	0.57	1.066	0.0074071
1.067	0.804	0.608	1.09	0.0079309

2) $N = 3$:

m/m_0	x_1^{opt}/L	x_2^{opt}/L	x_3^{opt}/L	x_4^{opt}/L	F_L^{opt}/F_0
0.4267	0.36	0.256	0.854	0.254	0.0082424
0.5333	0.392	0.294	0.864	0.264	0.010144
0.64	0.428	0.306	0.892	0.316	0.012070
0.7467	0.45	0.332	0.918	0.326	0.013800
0.8533	0.472	0.356	0.94	0.334	0.015426
0.96	0.492	0.376	0.962	0.342	0.016968
1.067	0.51	0.396	0.98	0.35	0.018438

3) $N = 5$:

m/m_0	x_1^{opt}/L	x_2^{opt}/L	x_3^{opt}/L	x_4^{opt}/L	F_L^{opt}/F_0
0.4267	0.246	0.214	0.784	0.268	0.0093268
0.5333	0.338	0.216	0.77	0.294	0.011776
0.64	0.346	0.24	0.806	0.304	0.014170
0.7467	0.362	0.262	0.836	0.31	0.016448
0.8533	0.378	0.28	0.864	0.314	0.018632
0.96	0.392	0.298	0.89	0.318	0.020737
1.067	0.406	0.314	0.914	0.324	0.022774

4) $N = 7$:

m/m_0	x_1^{opt}/L	x_2^{opt}/L	x_3^{opt}/L	x_4^{opt}/L	F_L^{opt}/F_0
0.4267	0.282	0.162	0.698	0.252	0.0096355
0.5333	0.296	0.18	0.73	0.28	0.012321
0.64	0.312	0.198	0.762	0.288	0.014895
0.7467	0.326	0.216	0.788	0.296	0.017387
0.8533	0.34	0.23	0.814	0.302	0.019810
0.96	0.354	0.246	0.838	0.308	0.022172
1.067	0.366	0.258	0.86	0.312	0.024479

5) $N = 9$:

m/m_0	x_1^{opt}/L	x_2^{opt}/L	x_3^{opt}/L	x_4^{opt}/L	F_L^{opt}/F_0
0.4267	0.262	0.14	0.648	0.256	0.0096581
0.5333	0.28	0.16	0.68	0.266	0.012341
0.64	0.294	0.174	0.714	0.274	0.014984
0.7467	0.306	0.19	0.744	0.278	0.017588
0.8533	0.318	0.202	0.774	0.284	0.020151
0.96	0.326	0.212	0.81	0.294	0.022768
1.067	0.338	0.226	0.822	0.296	0.025164